UPC - Universitat Politècnica de Catalunya

Doctoral Thesis

Solid-State Quantum Memory for Photonic Qubits

Author:
Mustafa Gündoğan

Supervisor:
Prof. Dr. Hugues de Riedmatten

A thesis submitted in fulfilment of the requirements for the degree of Doctor of Philosophy

in the

QPSA - Quantum Photonics with Solids and Atoms *group*,
ICFO - The Institute of Photonic Sciences

September 2015

"There is more than the germ of truth in things erroneous in the child's definition of memory as the thing one forgets with. To be able to forget means sanity. Incessantly to remember means obsession, lunacy."

Jack London, *The Star Rover*

Acknowledgements

First and foremost, I thank my adviser Hugues de Riedmatten for his guidance, trust and patience. His kind, wise and positive attitude always helped at times I thought I got stuck, or things looked difficult from the early days in the lab –when the lab was nothing but an empty room- to the days I was finalising this manuscript. I also thank him for bringing many fantastic people together in QPSA. I will always feel kind of privileged to be his first student at ICFO.

I was quite lucky to work with postdocs like Matteo, Patrick and Margherita from whom I learned a lot, really a lot, not only in the lab but also outside –in the *world of fanciness*, as Matteo would call it. I thank them all for everything and especially for their friendship.

Kutlu deserves a special thanks as he has absorbed my nonsense for the last three years. Thankfully, he was not some random person from Turkey but turned out to be really a good friend.

I thank Boris for his sense of humour and precision. *I mean* his fast and furious personality with such speed, very good (I know this sentence doesn't make sense). It was a bit pity that I didn't have the chance to share neither the office nor the lab with him, but still it was all fun.

I thank all the present and former members of the group (+ Gonzalo xd) for providing a warm and friendly atmosphere. And thanks Pau for the Catalan translation of the thesis abstract and the goals he scored in the campus football tournament. As a goalkeeper, I always felt quite lucky whenever he was in my side. Speaking of football, I thank all my fellow members of the ICFO football team. It was great to fight together even at times we were losing.

Although we have been physically far apart for many years, it was also our common enthusiasm, motivation and views I shared with Tolga that helped me stay in track.

I would like thank my former flatmate, the ex-physicist comrade Baybars for all the fun we had together both at home and in the *internets*. #aynıevdeyaşayanikidevletmemurununmaceraları will live on.

Müsemma and Arkadaş, I will always remember those two days you hosted me in Atlanta! Müsemma, thanks for pushing me to write about stuff other than science.

I appreciate the endless motivation my friends in *onharfliler* gave me both during the long nights I spent in the lab and also during the time I was writing this thesis. I am sorry to tell them that a teleportation à la Star Trek seems impossible (at least for now).

Human resources and the people in the academic affairs office deserve a special thanks as they made all the bureaucratic works (hence my life here as a non-EU person) a lot easier and smoother than otherwise possible. Manuela, Cristina, Anne, Mery and Laia, I thank you all.

Lastly, I thank my parents and my sister Hilal for always being there and always supporting me in this difficult path I chose years ago. I love you.

Abstract

Optical quantum memories (QMs) are one of the fundamental building blocks in quantum information science (QIS). They might find important use in quantum communication and computation applications.

Rare-earth ions (REIs) have been investigated for decades for their optical properties. They exhibit excellent coherence properties when cooled down to cryogenic temperatures. Not surprisingly, they emerged as a promising candidate for use in QIS as QMs.

In this thesis, we investigated the quantum storage of photonic qubits in a $Pr^{3+}:Y_2SiO_5$ (PrYSO) crystal for potential use in quantum communication and networking applications.

We started by constructing the experimental setup and the laser system from scratch as our research group had just been established at the beginning of this PhD study. First experiments included spectroscopy of the PrYSO system in order to identify the electronic transitions that are suitable for the QM experiments. We used the atomic frequency comb (AFC) memory protocol in all the experiments presented in this thesis. We also developed complex pulse sequences that are necessary for the optical preparation of an AFC.

As a first experiment, we demonstrated the storage of photonic polarization qubits encoded in weak coherent states in the excited states of Pr^{3+} ions for a predetermined storage time of 500 ns. This had not been achieved previously due to the polarization dependent absorption of the material. We achieved average storage fidelities of $\sim 95\,\%$ which surpass the best achievable value with a measure and prepare strategy, thus proving the quantum character of our interface.

Nevertheless, in order to be implemented in realistic quantum networking architectures, a QM should have the capability of on-demand retrieval of

the stored information. As a first step towards this goal, our next experiment concerned the transfer of the input pulses to and from the long-lived hyperfine ground levels of Pr^{3+} ions, albeit with bright pulses. Furthermore, by performing time-bin interference experiments, we demonstrated that the coherence is preserved during the storage, transfer and retrieval processes. Temporal multimode storage in the spin-states up to 5 modes was also shown.

Finally, in the last part of this thesis we demonstrated a solid-state spin-wave quantum memory, with qubits encoded in weak coherent states at the single photon level. Storing and retrieving single-photon level fields in the ground levels of the PrYSO system is challenging as the strong control pulses and the weak input pulse to be stored in the memory are separated by only 10.2 MHz. The control pulses create noise, mostly as free-induction decay, fluorescence and scattering off the optical surfaces. In order to circumvent this problem we employed narrow-band spectral, temporal and spatial filtering. By using spectral-hole burning based narrow band filter created in a second PrYSO crystal, we could achieve signal-to-noise ratio (SNR) > 10 for input pulses with mean photon number of around 1. The high SNR we achieved allowed us to store and recall time-bin qubits with conditional fidelities again higher than that is possible with a measure and prepare strategy. This experiments also represents the first demonstration of a quantum memory for time-bin qubits with on demand read-out of the stored quantum information.

The results presented in this thesis fill an important gap in the field of solid-state quantum memories and open the way for the long-lived storage of non-classical states of light. They further strengthen the position of REI based systems in QIS, specifically as nodes in scalable quantum network architectures.

Resum

Les memòries quàntiques òptiques (MQs) son un dels elements fonamentals en la ciència de la informació quàntica (CIQ). El seu ús podria ser important en aplicacions relacionades amb la comunicacio i la computació quàntiques.

Els ions de terres rares (ITRs) han sigut investigats durant dècades per les seves propietats òptiques. Exhibeixen excel·lents propietats de coherència quan es refreden a temperatures criogèniques. Per tant, no es sorprenent que hagin emergit com a candidats prometedors per ser usats en la CIQ com a MQs.

En aquesta tesis, hem investigat l'emmagatzematge quàntic de qubits fotònics en un cristall de Pr^{3+}:Y_2SiO_5 (PrYSO) per al seu possible ús en aplicacions relacionades amb les xarxes d'informació quàntiques. Vam començar construint el dispositiu experimental i els sistemes làser des de zero, ja que el nostre grup de recerca tot just acabava de néixer al començament d'aquest estudi doctoral. Els primers experiments van incloure espectroscòpia del sistema de PrYSO per tal d'identificar les transicions electròniques més apropiades per als següents experiments de MQs. En tots els experiments d'aquesta tesis vam utilitzar el protocol de memòria basat en una pinta de freqüències atòmiques (PFA). També vam desenvolupar complexes seqüències de polsos que són necessàries per a la preparació òptica d'una PFA.

En el primer experiment, vam demostrar l'emmagatzematge de qubits fotònics de polarització codificats en estats coherents febles. Aquest emmagatzematge es va dur a terme en els estats excitats dels ions Pr^{3+} durant un temps d'emmagatzematge predeterminat de 500 ns. Aquesta fita no s'havia assolit abans degut a que l'absorció òptica del material depèn de la polarització llum. Vam aconseguir fidelitats d'emmagatzematge d'un 95 % de mitjana, les quals sobrepassen el millor valor que es pot aconseguir amb

una estratègia de mesura i preparació, provant per tant el caràcter quàntic de la nostra interfície.

De totes maneres, per tal poder-se implementar de manera realista en xarxes quàntiques, una MQ hauria de tenir la capacitat de recuperar la informació en-demanda (en el moment que es desitgi). Com a primer pas cap a aquest objectiu, el nostre següent experiment va involucrar la transferència dels polsos d'entrada cap a i des de els nivells fonamentals hiperfins i longeus dels ions Pr^{3+}, mitjançant polsos brillants. A més, duent a terme experiments d'interferència, vam demostrar que la coherència es preserva durant els processos d'emmagatzematge, transferència i recuperació. Addicionalment, també vam demostrar l'emmagatzematge temporalment multimodal en els estats d'espín, de fins a 5 modes.

Finalment, en l'última part d'aquesta tesis vam demostrar una memòria quàntica d'estat sòlid basada en ones d'espín, amb qubits codificats en estats coherents febles al nivell d'intensitat de fotons individuals. Emmagatzemar i recuperar camps òptics al nivell de fotons individuals en estats fonamentals del sistema PrYSO és exigent. El motiu és que els potents polsos de control i el polsos dèbils d'entrada que s'emmagatzemen a la memòria estan separats per només 10.2 MHz. Els polsos de control creen soroll, la majoria consistent en decaïment de lliure inducció, fluorescència i dispersió en les superfícies òptiques. Per tal de resoldre aquest problema vam utilitzar filtratge estret de banda en freqüència i també filtratges temporal i espacial. Utilitzant un filtre estret de banda basat el la crema de forats espectrals en un segon cristall de PrYSO, vam poder aconseguir una relacio senyal soroll (RSS) > 10 per a polsos d'entrada amb un número mitjà de fotons al voltant de 1. L'alta RSS que vam aconseguir, ens va permetre emmagatzemar i recuperar qubits de inteval-de-temps amb fidelitats condicionals més altes una altra vegada que el que és possible amb l'estratègia de mesura i preparació.

Els resultats presentat en aquesta tesis omplen un buit important en el camp de les memòries quàntiques d'estat sòlid i obren la porta a l'emmagatzematge

de llarga durada d'estats de llum no-clàssics. A més, enforteixen la posició dels sistemes de IQ basats en ITR, específicament com a nodes en arquitectures de xarxes quàntiques.

List of publications

1. Mustafa Gündoğan, Patrick M. Ledingham, Attaallah Almasi, Matteo Cristiani and Hugues de Riedmatten, *Quantum Storage of a Photonic Polarization Qubit in a Solid*, Phys. Rev. Lett. **108**, 190504 (2012) (Chapter 5).

2. Mustafa Gündoğan, Margherita Mazzera, Patrick M. Ledingham, Matteo Cristiani and Hugues de Riedmatten, *Coherent storage of temporally multimode light using a spin-wave atomic frequency comb memory*, New J. Phys. **15**, 045012 (2013) (Chapter 6).

3. Daniel Rieländer, Kutlu Kutluer, Patrick M. Ledingham, Mustafa Gündoğan, Julia Fekete, Margherita Mazzera and Hugues de Riedmatten , *Quantum Storage of Heralded Single Photons in a Praseodymium-Doped Crystal*, Phys. Rev. Lett. **112**, 040504 (2014) (not part of the thesis).

4. Mustafa Gündoğan, Patrick M. Ledingham, Kutlu Kutluer, Margherita Mazzera and Hugues de Riedmatten, *Solid State Spin-Wave Quantum Memory for Time-Bin Qubits*, Phys. Rev. Lett. **114**, 230501 (2015) (Chapter 7).

Table of Contents

Chapter 1

Introduction

We have been living in the rather cliché-sounding *information age* in the last few decades. Transmission and storage of information revolutionized the world and the way we live. The classical information that shapes our lives is based on the *bit*, which can take up only two values. Mathematically, these values are commonly represented by 0 and 1, and any information can be encoded in strings of different bits. Physically, a bit can be represented in different forms. These include, but are not limited to, high/low voltage value, on/off state of a diode, presence/absence of a laser pulse and up/down alignment of the magnetization in a hard-drive. The combination of these technologies is what created the information age that was mentioned at the beginning.

On the other hand, our understanding of the physical universe was shaken with the birth of quantum mechanics and its weirdness in the last century. However, it was not until the last decades that those weird features of quantum mechanics could be technologically useful. Quantum information science (QIS) comes into the picture here.

1.1 Quantum information

QIS offers new technological perspectives to age-old technical problems while also providing tools and methods to test the fundamental aspects of quantum physics. These problems lie in quite broad areas such as communication, computation [1] and simulation [2]. It has already found its use in some applications, quantum key distribution (QKD) [3] being the major example. However, the current QKD experiments suffer from the losses in optical fibers which limit the operational range to at most few hundred kilometers. The no-cloning theorem imposes a fundamental limit as it states that no arbitrary quantum state can be cloned [4, 5]. This precludes the possibility of overcoming the problem of the optical loss by means of classical repeaters used in today's communication channels. In this context, the idea of quantum repeaters is being explored by many research groups, both theoretically and experimentally to overcome the limitations imposed by the optical losses and the no-cloning theorem.

In this section, I will introduce the basic concepts in QIS. The notions of quantum superposition and entanglement are the heart of quantum mechanics and as will be explained soon, they are the key resources in QIS.

1.1.1 Qubits

In quantum mechanics, the state of the particles or quantum systems can be expressed as the superposition of orthogonal states. One can then think of the quantum version of the smallest bit of information, the *qubit*, which is a quantum superposition of 0s and 1s. The word *qubit* stands for "quantum-bit" and it was first introduced by Schumacher in 1995 [6]. A qubit can be represented in Dirac notation as,

$$|\psi\rangle = \alpha|0\rangle + \beta|1\rangle, \tag{1.1}$$

where, α and β are the complex probability amplitudes with $|\alpha|^2+|\beta|^2 = 1$. Here, $|0\rangle$ and $|1\rangle$ are the two orthogonal basis states. Another form of representing a qubit is,

$$|\psi\rangle = \cos\left(\frac{\theta}{2}\right)|0\rangle + e^{i\phi}\sin\left(\frac{\theta}{2}\right)|1\rangle, \tag{1.2}$$

where, the qubit is now represented on a sphere, known as the *Bloch sphere* with unit length with θ and ϕ are azimuthal and longitudinal angles. Unlike the classical bit, the qubit can take up any superposition state between the two bases on the surface of the Bloch sphere. However, any measurement made on the qubit collapses the state into one of the bases, with a probability dictated by α and β.

Physically, a qubit can be implemented in numerous ways. Stationary qubits can be implemented, for instance, with the electronic or spin levels of trapped atoms or ions and opposite flux circulations in superconducting circuits. Flying qubits that carry the quantum information are usually encoded in photons in different degrees of freedom. These include polarization, frequency, path and orbital angular momentum. Photons can also carry the quantum information encoded in *time-bin*s. I will now discuss polarization and time-bin qubits in more detail since they will be used in this thesis.

1.1.1.1 Polarization qubits

The polarization state of a photon is a naturally-occurring two-level system and hence it has been widely used as a means to encode qubits. In its most basic form a polarization qubit is represented as,

$$|\psi\rangle = \alpha|H\rangle + \beta|V\rangle. \tag{1.3}$$

With different combinations of α and β, any polarization state can be created on the Bloch sphere, which in this context, known as the Poincaré sphere (Fig. 1.1). [7].

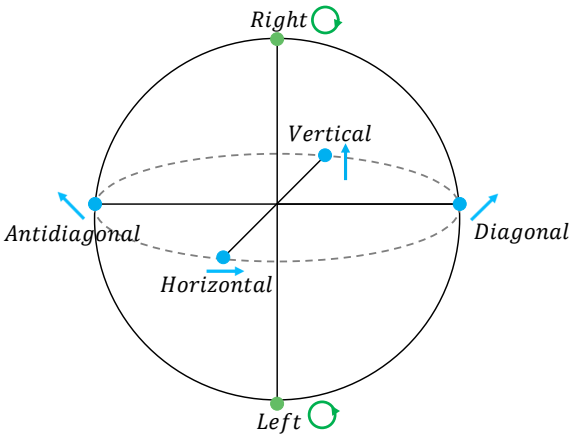

FIGURE 1.1: Pictorial representation of polarization qubits on the Bloch Sphere.

The polarization degree of freedom offers an easy preparation and analysis of qubits. However, it is not an easy task to maintain the polarization states during the transmission over long distances in optical fibres due the polarization fluctuation and depolarization due to polarization mode dispersion. Although there are some recent proposals to overcome this problem [8, 9], it still remains a significant technical challenge for the long distance transmission of polarization qubits.

1.1.1.2 Time-bin qubits

Time-bin encoding [10] has been used as it is more robust against decoherence during the transmission. Although it is relatively more difficult to prepare and analyse time-bin qubits than polarization qubits, they emerged as a promising alternative to polarization encoding and has already been used in some major experiments [11–13]. Time-bin qubits are prepared by sending a pulse of light (ideally a single photon) through a Mach-Zehnder interferometer (MZI), with a controllable phase α between the two arms. The output can be written as [14],

$$|\psi\rangle = c_e|e\rangle + c_l e^{i\alpha}|l\rangle. \tag{1.4}$$

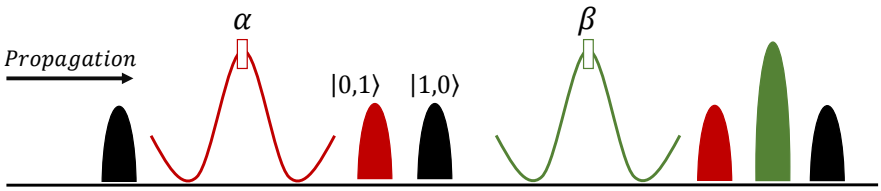

FIGURE 1.2: The schematic of the preparation and the measurement of time-bin qubits.

Here, the state $|e\rangle$ ($|l\rangle$) represents a photon passing through the short (long) arm, with a probability amplitude c_e (c_l) with $|c_e|^2 + |c_l|^2 = 1$. Figure 1.2 shows the preparation and the measurement of time-bin qubits. The first MZI is used to prepare the qubit in the form of Eq. 1.4, whereas the second MZI that is identical to the first one is used to analyse the prepared qubits in a superposition basis. When the prepared qubit is sent through the second MZI, each component again takes either the long or the short arm. As a result, the input pulse thus can take four different routes after two MZIs; short-short, long-long, long-short and short-long. However, the path length of the last two routes are equal and thus they can create interference. This results in three distinct temporal modes. The interference region is shown in green in Fig. 1.2. One can analyse the qubits by varying the phases α and β in a controllable manner, and measuring the visibility of the observed interference.

The concept of time-bin encoding was introduced by the group of Nicolas Gisin [10, 11] and it has been exploited in many demonstrations in quantum information and communication science, such as long distance teleportation [14] and distribution [15] of qubits. It can be also be used in creating high dimensional entanglement between two photonic systems. As an example, first an 11- [16] and later a 19-dimensional two-photon state has been created [17]. Finally, time-bin entangled photons from a quantum dot has also been observed recently [13].

1.1.2 Entanglement

The ideas that led to the quantum revolution in information science (and also the nature of reality) started with Einstein's early dissatisfaction with quantum mechanics. He, together with Boris Podolsky and Nathan Rosen, noticed that two particles that share a common history can still affect each other instantaneously, no matter how far they are separated. In their celebrated 1935 paper, also known as the EPR paper, they draw the conclusion that quantum mechanics is not complete [18]. It was after 1964, when John Bell provided an inequality known with his name that the ideas put forward in the EPR paper became experimentally testable [19]. However, it took a long time until the first experimental signs suggesting that Einstein was wrong about quantum mechanics [20–22].

The *spooky* connection between the particles that was pointed out in the EPR paper [18] was later called *entanglement* by Erwin Schrödinger in 1935 [23]. Mathematically speaking, a system is called entangled if the quantum state of the whole system cannot be factorized to the individual states of its constituents. For example, the following joint quantum state of two spin $-1/2$ particles is an example of an entangled state,

$$|\Psi^{\pm}_{1,2}\rangle = \frac{1}{\sqrt{2}}\left(|\uparrow_1,\downarrow_2\rangle \pm |\downarrow_1,\uparrow_2\rangle\right), \tag{1.5}$$

for the perfect negative correlation. Here, the state $|\uparrow_1,\downarrow_2\rangle$ corresponds to the situation where the particle 1 (2) has a spin projection of $+1/2$ $(-1/2)$ with respect to the quantization axis. For the case of a perfect positive correlation, one has the following entangled state,

$$|\Psi^{\pm}_{1,2}\rangle = \frac{1}{\sqrt{2}}\left(|\uparrow_1,\uparrow_2\rangle \pm |\downarrow_1,\downarrow_2\rangle\right). \tag{1.6}$$

Equations 1.5 and 1.6 imply that any single measurement performed on an individual spin also determines (i.e. collapses) the state of the other pair of the system, although no measurement is performed on it. This kind of correlation between two particles cannot be explained classically. The

measurement that projects the joint state of two quantum particles (two qubits in the context of QIS) to the form of Equations 1.5 and 1.6 is called a *Bell state measurement*. These states are thereafter called *Bell states*.

The concept of entanglement sparked an interest in superluminal communication during 1970s and 1980s. There were several attempts to exploit entanglement in an effort towards this goal [24, 25] which were all bound to fail. However, these attempts sparked an interest in research on the fundamentals of quantum mechanics and resulted in seminal works of Dieks [4] and Wootters and Zurek [5]. They showed that an arbitrary quantum state cannot be cloned, precluding the dreams of faster-than-light communication but stimulating further ideas, the most remarkable one being the quantum teleportation [26, 27].

There have been recent ideas that attempt to explain quantum entanglement in terms of a *wormhole* (also known as Einstein-Rosen bridges [28][1]) connecting different points in space-time [29]. This conjecture is known as ER = EPR and has attracted much attention lately [30, 31]. However, it is far outside the context of this thesis and mentioned here for the interested reader.

1.2 Quantum communication

The field of quantum communication deals with the distribution of quantum information mainly carried by light, over long distances. This opens up possibilities for applications such as secure communication [3, 32]. It also has implications in fundamentals of quantum physics, perfectly illustrated with experiments aiming at demonstrating quantum nonlocality between distant particles [33].

[1] It is interesting that this paper had been submitted to Physical Review less than two months after the submission of the EPR paper. It is again interesting that a possible connection between the two works came to light almost 78 years later.

The first proposal that utilizes the fact that light is made up of indivisible quanta is the quantum key distribution (QKD) [34]. In simple terms, it allows two distant parties to share a secret key in a secure way by transmission of single photons. The first QKD proposal has been made by Bennett and Brassard and is known as the BB84 protocol. Later, Artur Ekert proposed another protocol for secure key distribution that makes use of entanglement [35], which is known as Ekert91 protocol. QKD systems, based on the BB84 protocol have already been available commercially for almost a decade now.

However, long-distance QKD and transmission of quantum information is limited by the loss and decoherence that scales exponentially with the distance. If the photons are to be distributed through optical fibres, then the loss mechanism would be the absorption and scattering in the fibre (0.2 dB/kM for telecom C-band). This means that more than 1/3 of the carried energy is already lost just after 10 km. The transmitted energy drops down to 1 % after a reasonable 100 km [36]. One solution to this problem is to use the satellites in Earth's orbit as relay stations to transmit the quantum information over long distances [37, 38]. The other solution proposed to overcome this problem is called the *quantum repeater*, which will be described in the next section.

1.3 Quantum repeaters

The quantum repeater is a concept first proposed in Ref. [39] to overcome the limitations mentioned above for long distance entanglement distribution [36].

The underlying principle of the quantum repeater is the *entanglement swapping*. If one starts with two entangled systems, $a\&a'$ and $b\&b'$, then it is possible to create an entangled state between a and b, by performing a Bell-state measurement on particles a' and b'. The original idea that was put forward in Ref. [39] is to divide the distance L over which the

entanglement swapping operation would be performed into many shorter segments with length L_0. Then, individual entanglement swapping operations can be performed between neighbouring nodes and the concatenation of this operation would result in the entanglement between the two ends of the whole link, over the distance L.

A remarkable proposal to realize a practical quantum repeater came in 2001, known as the DLCZ scheme named after the authors (Duan, Lukin, Cirac and Zoller) [40]. The proposal is based on the creation, storage and transfer of a photon to a single collective spin-excitations in atomic ensembles. Entanglement between remote ensembles is achieved by a quantum interference in the detection of photons emitted by the atomic ensembles, that are mixed at a beam splitter and detected with a single photon counter. This protocol triggered an intense experimental effort and the main ingredients have now been realized experimentally [36]. Atomic ensembles provide the means to store the quantum information long enough so that the result of the entanglement creation operation could be transferred between different nodes. This protocol has the great advantage that it uses only atomic ensembles and linear optics. Also, the ensembles serve as entanglement source and quantum memory in one physical system. However, the drawback is that most of the systems used for DLCZ experiments (Cs and Rb atoms) emit light around 800 nm, where the loss in optical fibers is very high. Also, the outcome of the entanglement creation operation in each elementary link can only be learned later through a classical channel [26], so this limits the time between two entanglement generation attempts to around L_0/c, where c is the speed of light.

Another protocol, which makes use of photon pair sources and multimode memories for light [41] has been proposed in order to circumvent these problems. The scheme is a modified version of DLCZ protocol. In its simplest form, the individual segment consists of two quantum memories, $M_{(A,B)}$, and two entangled photon pair sources, $S_{(A,B)}$ as shown in Fig. 1.3(a). If each source emits photon pairs, with a probability $p/2$, with

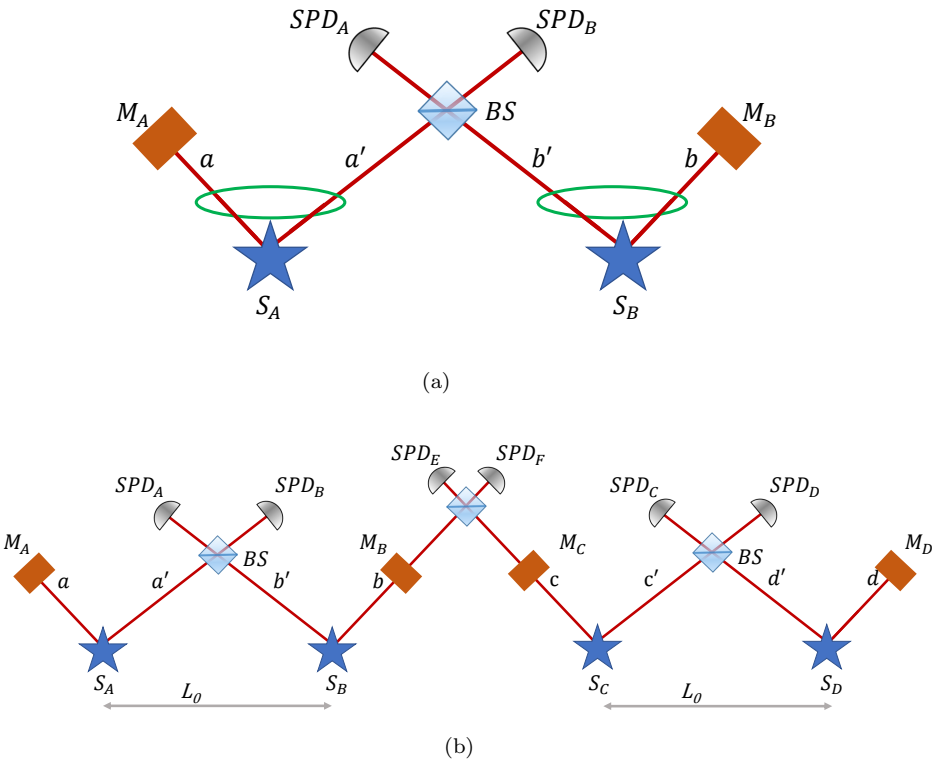

FIGURE 1.3: Basic schematic of a quantum repeater segment based on the proposal [41]. (a) Entanglement between the two distant memories (M_A and M_B) can be created by a Bell state measurement (BSM) on the photons in the modes a' and b'. (b) The entanglement can be extended by performing another BSM with the photons retrieved from the memories M_B and M_C, given that the photons in the modes a (d) are stored in the memories M_A (M_D) until the result of the second BSM is known.

$p \ll 1$, then the overall state can be written as follows [41]

$$|\Psi\rangle = \left[1 + \sqrt{\frac{p}{2}}\left(a^\dagger a'^\dagger + e^{i\phi_{AB}} b^\dagger b'^\dagger\right) + O(p)\right]|0\rangle. \tag{1.7}$$

In this equation a and a' (b and b') are the optical modes of the entangled pairs, ϕ_A (ϕ_B) is the phase of the pump ($\phi_{AB} = \phi_B - \phi_A$) laser for the corresponding source and $O(p)$ is the term that includes the higher photon number contributions. The photons in the mode a (b) is stored in optical

memory M_A (M_B) and photons in modes a' and b' are sent through optical fibers over a distance and then combined at a beam splitter, BS. The two photons of the pair can have different wavelengths, such that a and b are resonant with the quantum memory and a' and b' can be at telecommunication wavelengths to minimize the loss in the fiber transmission. The joint state is projected to the following state upon the detection of a single photon in either of the single photon detectors (SPDs),

$$|\Phi\rangle_{AB} = \frac{1}{\sqrt{2}} \left(a^\dagger e^{i\theta_A} + b^\dagger e^{i\theta_B} \right) |0\rangle. \tag{1.8}$$

In this equation, θ_A (θ_B) denotes the total phase acquired by the photon a (b) until it reaches the detector and the phase from the laser to the photon pair source. If we recall that the photon a (b) is stored in the memory M_A (M_B), then the Eq. 1.8 can be finally expressed in the following entangled state of the two memories,

$$|\Phi\rangle_{AB} = \frac{1}{\sqrt{2}} \left(|1\rangle_A |0\rangle_B + e^{i\theta_{AB}} |0\rangle_A |1\rangle_B \right). \tag{1.9}$$

This equation means that when there is a single excitation stored in M_A the state of M_B is empty, and vice versa. Here $\theta_{AB} = \theta_B - \theta_A$.

One can concatenate the scheme we described so far, by implementing Bell state measurements on the photons stored in memories M_B and M_C (Fig. 1.3(b)). The overall effect of this measurement is to map the state of the system into an entangled state of the memories (M_A and M_D) located at the two ends of the whole link.

The description given so far does not require the memories to have multimode capabilities. Nevertheless, if the memories can store multiple temporal modes, then the number of entanglement generation trials can be increased dramatically. In this way, one does not need to wait the time L_0/c as we have discussed above. Eventually this scheme's main advantage is faster scaling of the entanglement distribution time over a given

range. For instance, it would take $\sim 100\,\mathrm{s}$ with DLZC protocol to create entanglement between 500 km, whereas the same task only takes $\sim 1\,\mathrm{s}$ with the protocol presented in, assuming a memory capable of storing 100 modes [41]. However, to realize this proposal one still needs to implement multi-mode optical quantum memories.

1.4 Quantum memories

Quantum memory (QM) is an integral part in prospective applications in QIS, such as deterministic single photon sources [42, 43], single photon detection [44, 45] and linear optics quantum computation [46]. In the context of quantum communication though [36], QM is a device that can store the quantum information sufficiently long enough, so that it allows the entanglement distribution over neighbouring nodes with high fidelity [47–49]. We limit our discussion of QMs in this context.

The physical realization of QMs relies on converting light to excitations in long-lived atomic states. This would map the information carried by photons to the internal states of atoms or ions. Several systems have been explored for this purpose, mainly single atoms or ions trapped in cavities, cold and warm atomic gases and solid-state system, such as rare-earth ion doped (REID) crystals. The very first experiment demonstrating the mapping of photonic quantum information to the atomic states was performed in the group of Eugene Polzik in 2004 [50]. In this and the following experiments [51, 52] from the same group, the quantum information is carried by the quadrature components of the light. (Called *continuous variable* QIS [53]. Also a quantum repeater protocol for continuous variable optical states has just been recently made [54].)

We will be concentrated on the *absorptive* type of quantum memories, where the quantum information encoded in a pulse of light is absorbed and transferred preferably to and from long-lived electronic states of the

atomic system. This is the type of the memory that should be implemented to realize a quantum repeater architecture as described in Sec. 1.3. There is also the *emissive* type of quantum memories, where the quantum entanglement between the photon and the memory is created with the application of classical pulses [48, 55–58].

There are several figures of merit that are used to characterize the performance of a quantum memory. These will be outlined in the following sections. More detailed information on quantum memories is given in Sec. 3.2.

1.4.1 Efficiency

One important parameter to assess the performance of an optical memory is its efficiency, denoted with η. It is basically defined as the ratio of the retrieved pulse energy to the input pulse energy. It should be as high as possible, but it has been shown that a value of around 90 % is required in order for a quantum memory to be useful in quantum repeater applications [36].

The efficiency of an optical memory can be enhanced by better engineering the light-matter interaction in the system, such as putting the memory in an optical cavity or using ensembles instead of single absorbers or combining the two approaches together. Nevertheless, highly efficient storage of light in a memory is not sufficient by itself since the quality of the storage of the quantum information is also of vital importance. This brings us to the notion of *fidelity*.

1.4.2 Fidelity

In the context of quantum repeaters using absorptive memories, qubits and photon counting, the fidelity is described as the overlap between the states of the retrieved pulse and that of the input pulse, conditioned on

the fact that the memory gives an output. This is called the conditional fidelity and it can be expressed as,

$$F^c = \mathrm{Tr}(\rho_{\mathrm{in}}\rho_{\mathrm{out}}). \tag{1.10}$$

On the other hand, fidelity can also be calculated with respect to a target state $|\psi\rangle$ as follows,

$$F^c_{|\psi\rangle} = \langle\psi|\rho_{\mathrm{out}}|\psi\rangle. \tag{1.11}$$

Eqn. 1.11 is the definition that we will use in Chapters 5 and 7. Any process is said to be in the quantum domain if the measured fidelity of the process surpasses the maximum value that can achieved by means of classical strategies. For the case of the storage of quantum information, the classical strategy against which we compare our results is the *measure-and-prepare strategy* where a measurement is done on the input qubits and the output qubits are prepared based on the results of the measurement done. The maximum fidelity that can be obtained for such a strategy is given by [59],

$$F = \frac{N+1}{N+2}. \tag{1.12}$$

This equation is valid for the case of an N-particle Fock state. However, it should be modified if the quantum memory is tested with weak coherent states (see Appendix A for details).

1.4.3 Storage time

One of the most important figures of merit for an optical quantum memory is its storage time. Given that a memory could store the quantum information with high efficiency and high fidelity, it should still have the capability of storing the information for the time it takes to establish entanglement over the two ends of the whole link. Storage time of around a second is needed in order to successfully distribute entanglement over a link of 1000 km, for example [36].

1.4.4 Other criteria

As we have presented above, the multimode capability is a crucial property for quantum memory to implement practical quantum repeater architectures.

Another important criterion is the ability to distribute the photons over long distances through optical fibres with low loss. However, this requirement puts a limitation on the wavelength of the transmitted photons, since the low loss spectral window of optical fibres is situated around $\sim 1.5\,\mu$m. This puts constraints on the atomic systems but the problem can be tackled by implementing quantum frequency converters with nonlinear crystals [60, 61].

The quantum repeater proposal [41] presented in Sec. 1.3 already offers a solution to overcome this limitation. An entangled photon pair source that emits one photon of the pair in the telecom wavelength, where the other photon has an optical wavelength suitable with the quantum memory offers long-distance scalability of such networks [62].

1.5 Contents of this thesis

In this thesis I present the experimental work that was carried out during the period September 2010 - September 2014. It should be noted here that our research group had just been established at the time and the work also contained building the experimental setup from scratch. Our work mainly concentrated on the storage of quantum information encoded in different forms (polarization and time-bin qubits) in a $Pr^{3+}:Y_2SiO_5$ crystal using the atomic frequency comb (AFC) protocol.

Chapter 2 provides the background for REID systems in general, and for $Pr^{3+}:Y_2SiO_5$ system in particular.

In Chapter 3, I introduce the basic light-matter interaction physics to understand the results and the techniques used in this thesis. Also included is the different quantum memory protocols implemented in solid-state medium, together with a detailed description of the atomic frequency comb protocol, the memory technique that we used in all the experiments presented in this thesis.

Chapter 4 details the experimental setup that was used in all the experiments. Discussions include the sum-frequency-generation of 606 nm light, locking of the laser frequency with the Pound-Drever-Hall technique, details of the cryostat and the detection and data acquisition hardware.

The first experimental results are presented in Chapter 5, where we report the first demonstration of quantum storage of photonic polarization qubits in a solid-state system. Also included in that chapter is the measurement of polarization qubits and a brief description of quantum state tomography technique.

In Chapter 6, I present our work on the coherent storage of temporally multimode light in the spin-states of a REID solid. This experiment is also the initial step towards our end goal, the on-demand storage and retrieval of single-photon level light pulses in the same system.

Chapter 7 presents the results of spin-state storage of single-photon level light in the crystal. It also presents the first on-demand quantum memory for time-bin qubits realized with any physical system. The main technical challenge, that is the narrow-band spectral filtering of the noise to reach the quantum level is also described in detail.

Chapter 2

Rare-earth doped crystals

This chapter will deal with the electronic and optical properties of the material system that we used throughout the course of this PhD study. The atomic system that we choose to study is a rare-earth ion doped (REID) solid, specifically a Y_2SiO_5 crystal doped with Pr^{3+} ions. In this section I benefited from several reviews [63–65] and PhD theses [66, 67] on the subject.

Rare-earth elements, also called Lanthanide series are recognized with partially full $4f$ electronic shells inside the filled $5s$ and $5p$ electronic orbitals. They have atomic numbers ranging from 57 for Lanthanum to 70 for Ytterbium. $4f$ orbitals have smaller radii than the $5s$ and $5p$ orbitals. The outer electronic levels are filled first so the $4f$ orbitals of the rare-earth element remain unfilled. The radial distribution of different electronic wavefunctions are shown in Figure 2.1 for Pr^{3+}. The filled outer electronic orbitals provide a *screening effect* for the $4f$ orbitals. These orbitals basically act like a Faraday cage that protects the $4f$ electrons from the external perturbations caused by the crystal lattice. When cooled to cryogenic temperatures to suppress the effect of phonons, this screening results in very sharp $4f^n - 4f^n$ transitions that make REIDs attractive for quantum information applications that requires long coherence times. Here, n is the

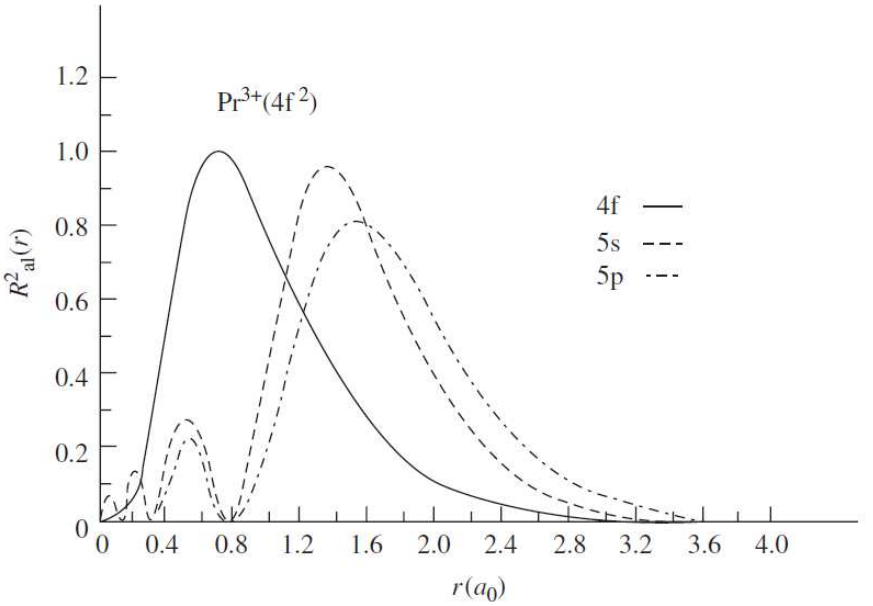

FIGURE 2.1: Radial distribution of different electronic orbitals, showing the smaller size of the $4f$ orbitals for Pr^{3+} ion. Figure is taken from [68].

number of electrons in the $4f$ shell. Transitions as narrow as 50 Hz in the infrared for Er^{3+} ions [69] and 100 Hz in the visible domain for Eu^{3+} ions [70] in a solid-state environment were reported. Thanks to this screening effect the ions embedded in solids can be treated as free ions in perturbative potentials, which simplifies handling the electronic and spectroscopic properties. The most stable and common oxidation state of rare-earth elements is 3+, although 2+ and 4+ states are also observed in some of them. We will consider only the trivalent ionization case for the rest of this manuscript. As the main electronic state in all rare earth elements is the same it is the ionic radius that distinguishes one from another.

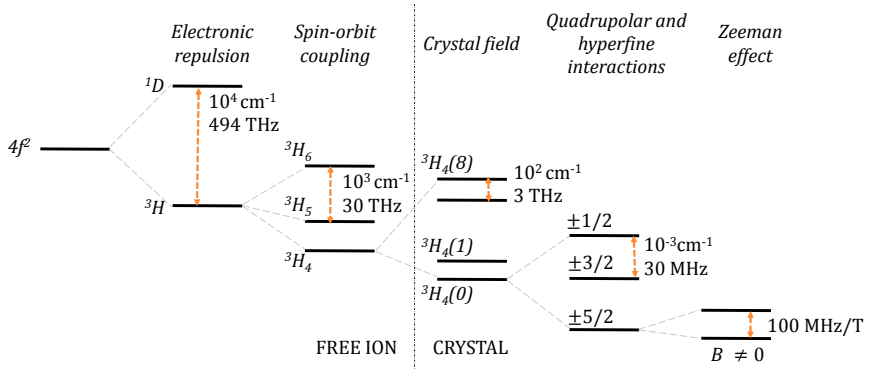

FIGURE 2.2: Simple schematic of the electronic energy levels of rare-earth ions with different interactions.

2.1 Energy levels

$4f$ electrons in rare-earth ions can be treated as electrons in free ions that are under the effect of the crystal field. The remaining interactions, such as hyperfine, can be approximated as small perturbations. The strong spin-orbit coupling in rare-earths splits the $4f$ levels into J-manifolds which give rise to optical transitions. Spin-orbit coupling gives rise to *spectral terms*, denoted with $^{2S+1}L_J$, where S is the net electronic spin, L is the total orbital quantum number and J is the total angular momentum quantum number. The letter L is determined with the following convention, $L = 0, 1, 2, 3, 4, 5, ... \equiv$ S, P, D, F, G, H... Following this rule, one can find the ground state manifold of Pr^{3+} ion to be $^3H_4$. For rare earth ions with odd or even number of electrons, these levels then further split into (2J+1)/2 or 2J+1 levels due to the Stark shift created by the crystal lattice, depending on the site symmetry. These separations are typically on the order of $0.1 - 1$ THz and they are much smaller than the separation between different J manifolds. This keeps J still a good quantum number. The electrons in the higher levels of Stark manifolds mostly decay to the lowest lying levels through phonon emissions. They can then decay to the lowest lying levels of other Stark manifolds. In almost all

of the experiments related to quantum information with rare-earth ions, only the transitions between these lowest lying levels are used because of their long coherence and population lifetimes. These transitions are called *zero-phonon transitions*, as they do not involve any phonon throughout the process. Nonetheless, the zero-phonon transitions are not limited to these but also includes other transitions that do not include a phonon transition. Simple representation of the effects of different interactions on the free-ion electronic energy level is drawn in Figure 2.2.

As for the magnetic properties of rare-earth ions, one needs to consider the elements with odd and even number of f electrons differently. The unpaired electron of the ions with odd number of electrons results in ground states that are magnetic doublets having a magnetic moment about the Bohr magneton. These ions are also called Kramers ions [71]. The electronic degeneracy of a J-state is lifted in non-Kramers ions (ions with even number of electrons) in low-symmetry sites. So the resultant electronic levels are singlets and the electronic angular momentum is *quenched* to first order by the crystal field for lattice sites with less than axial symmetry [63].

2.2 Hyperfine levels

Until now, we gave a qualitative discussion of the energy level structures. Quantitatively, all the effects on the $4f$ orbitals can be included in the Hamiltonian [63],

$$\mathcal{H} = [\mathcal{H}_{FI} + \mathcal{H}_{CF}] + [\mathcal{H}_{HF} + \mathcal{H}_{Q} + \mathcal{H}_{Z} + \mathcal{H}_{z}] \tag{2.1}$$

Here, the first term accounts for the free ion case together with the spin-orbit coupling, the second term represents the crystal field interaction that we already described previously. The total Hamiltonian is grouped into two parts as the first part is mainly responsible for the large splittings,

whereas the terms in the second group can be treated as perturbations to the system and are responsible for the hyperfine structures.

In Equation 2.1, $\mathcal{H}_{HF}$ is the hyperfine coupling between the electrons and the nuclear spin, $\mathcal{H}_Q$ is the nuclear electric quadrupole interaction, $\mathcal{H}_Z$ is the electronic Zeeman and $\mathcal{H}_z$ is the nuclear Zeeman interactions.

Since the angular momentum is quenched by the crystal field as we described above for low-symmetry sites, there is no first order hyperfine interaction. This is also the regime that we are interested in as Pr^{3+} ions also belong to this class. In the presence of this quenching there is still the second order hyperfine interaction that arises from the perturbation theory and the system now can be described with the following effective Hamiltonian [63],

$$\mathcal{H}_{eff} = -g_J^2\mu_B^2 \boldsymbol{H}\cdot\Lambda\cdot\boldsymbol{H} - (2A_{\mathbf{J}}g_J\mu_B\boldsymbol{H}\cdot\Lambda\cdot\boldsymbol{I} - \mathcal{H}_Z) - (A_{\mathbf{J}}^2\boldsymbol{I}\cdot\Lambda\cdot\boldsymbol{I} + \mathcal{H}_Q) \tag{2.2}$$

where, $\mathbf{H}$ is the applied magnetic field, $\mathbf{I}$ is the vector form of nuclear angular momentum operators, g_J is the Lande g-factor and μ_B is the Bohr magneton and $A_{\mathbf{J}}$ is the magnetic hyperfine constant. Here Λ is the tensor describing the second order interactions in the system. The first term in the Eqn. 2.2 is the quadratic electronic Zeeman shift, the second term is the enhanced nuclear Zeeman Hamiltonian (enhancement is due to the coupling to the second order hyperfine interaction) and last term is the effective quadrupolar Hamiltonian which is the combination of the second order hyperfine and pure quadrupole interactions. This term is also known as the *pseudo-quadrupolar interaction* term.

There are several mechanisms determining the long population lifetimes of the hyperfine ground levels [72]. Among these are: *i*) phonon processes, which include direct phonon couplings, non-resonant Raman scattering of phonons and two-phonon Orbach process [73]. These mechanisms become dominant at higher temperatures as they involve phonons. *ii*) REI−host nuclear spin flips and *iii*) REI−REI spin flips. The last two contributions

are comparable for weakly doped samples and thus can be approximated with one combined lifetime. Thus the ground state hyperfine population lifetime exhibits two distinct decays. These will be explained in detail in the next section.

2.3 Homogeneous and inhomogeneous linewidths

2.3.1 Homogeneous linewidth

The previous section described the time-independent processes that give rise to electronic level structures. However, dynamic events at the level of individual REIs would determine the lifetime of those electronic levels. Here the term *homogeneous* means that each REI is affected by the same processes in the same way.

The homogeneous linewidth, Γ_{hom} of a transition is ultimately limited by the pure population decay time, T_1, and it is further broadened by several dephasing mechanisms,

$$\Gamma_{hom} = \frac{1}{2\pi T_1} + \frac{1}{\pi T_2^*} = \frac{1}{\pi T_2}, \tag{2.3}$$

where T_1 represents the non-radiative decay channels and T_2^* is the dephasing processes that we will explain soon. The overall homogeneous linewidth can be expressed in terms of $1/T_2$, a term which includes both dephasing and population decay times. The systems that exhibit zero dephasing are called T_1-limited. I will now explain different physical processes that result in the homogeneous linewidth of individual ions, following the treatment given in [67].

2.3.1.1 Ion-phonon interactions

Phonons in the crystalline host matrices usually have energies comparable to the splittings between individual crystal field levels within a J-manifold.

As a result, a direct coupling between the phonons and the higher lying crystal field levels is possible. This results in the decay of the electrons in these levels to low-lying crystal field levels. This is a T_1 process, as it directly effects the electronic lifetime. Since the energy gap between different J-manifolds is too large, only multi-phonon processes could induce phononic transitions between different J-manifolds possible.

Apart from the above-mentioned direct phonon and multi-phonon couplings, elastic Raman scatterings can also have an effect on the Γ_{hom}. These are pure dephasing (T_2^*) events as the population does not change after the process. However, these contributions to Γ_{hom} at temperatures < 6 K can be neglected [74].

2.3.1.2 Spin-spin interactions

Electronic spins of REIs can also interact with the spins of the other REIs as well as the nuclear spins in the host matrix. Fluctuating spins in the environment would thus result in a fluctuating magnetic field at the REI, which in the end contribute to Γ_{hom}. To reduce the effect of ion-nuclear spin interaction, host materials with low nuclear magnetic moments, such as Y_2SiO_5, are chosen. Another method to mitigate this effect is to apply an external magnetic field with a particular direction and strength, such that the first order Zeeman shift becomes zero [75, 76]. This method is called Zero First Order Zeeman Shift (ZEFOZ) and has been successfully applied to increase the ground state hyperfine coherence time of Pr^{3+}:Y_2SiO_5 to around 1 s, from $\sim 500\,\mu$s. Finally, the individual electronic spins of REIs can also interact with other REI electronic spins, however this is negligible for non-Kramers ions as their electronic magnetic moment is quenched.

This is the reason why the silicates, for example, are good materials to host rare-earth ions as they have very small nuclear magnetic moments. Non-Kramers ions (including Pr^{3+}) have non-magnetic electronic energy

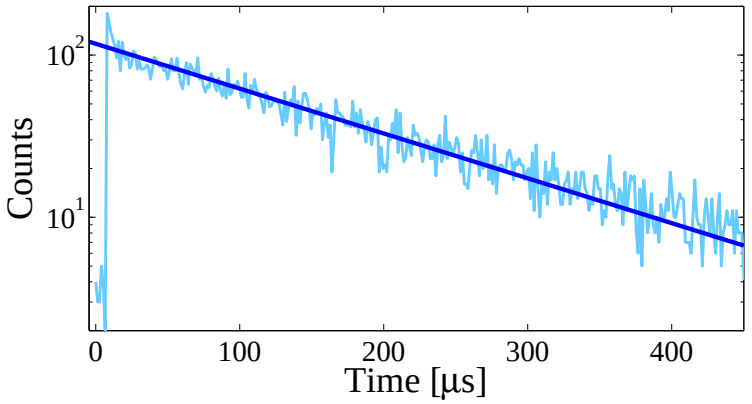

FIGURE 2.3: Measured population lifetime of $^1D_2 - ^3H_4$ transition in Pr^{3+}. The straight line is the exponential fits to the data. The measured T_1 is $\sim$160 μs.

levels which allows them to have long optical coherence times. However, for Kramers ions, application of an external magnetic field can mitigate the effect of the fluctuating magnetic field in the crystal environment and thus one can achieve long optical coherence times.

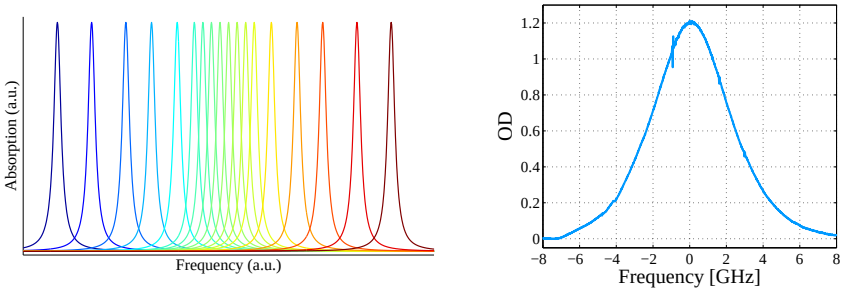

(a) (b)

FIGURE 2.4: (a)Schematic description of inhomogeneous broadening. Each individual line represents a single ion. (b) The experimental trace of the inhomogeneous broadening. The probe light is horizontally polarized with respect to the D_2 axis of the crystal.

2.3.2 Inhomogeneous linewidth

The crystal field inside the lattice is not spatially isotropic and as a result, individual ions located at different sites might experience slightly different field. This slight variation results in slightly different transitions in different ions. In the end, if the ensemble of the ions is probed collectively, the overall absorption line would have a width of the whole ions. This is called the inhomogeneous linewidth (Γ_{inh}) and it is much larger than the individual linewidths (see Figure 2.4(a)). The ratio $\Gamma_{\text{inh}}/\Gamma_{\text{hom}}$ can be up to 10^8 for rare-earth ions doped into solids. For Pr^{3+}, inhomogeneous linewidth is usually around $1 - 10$ GHz, mostly dependent on the doping level. In our case, as shown in Fig. 2.4(b), the measured Γ_{inh} is around 5 GHz for a 3 mm long crystal with 0.05% doping level. It should be noted that Γ_{inh} does not depend on the crystal length.

One of the important points is that Γ_{inh} is often much larger than the hyperfine splittings, which are on the order of tens of MHz. The main consequence of this fact is that within an inhomogeneously broadened ensemble all of the possible transitions can be excited by a single frequency field (Figure 2.5). For this reason, at first sight, the inhomogeneous broadening may look like an effect that must be eliminated. But on the other hand, when combined with the long hyperfine population lifetimes, it can be used as a resource for quantum memory protocols. The main technique enabling these tasks is called *spectral hole burning* that will be detailed in Sec. 2.5.

2.4 Pr^{3+}:Y_2SiO_5

Pr^{3+} is a non-Kramers ion with 2 electrons in its $4f$ shell. The host material yttrium orthosilicate Y_2SiO_5 is a monoclinic biaxial crystal belonging to the C_{2h}^6 symmetry group with eight molecules per unit cell [77]. Pr^{3+}

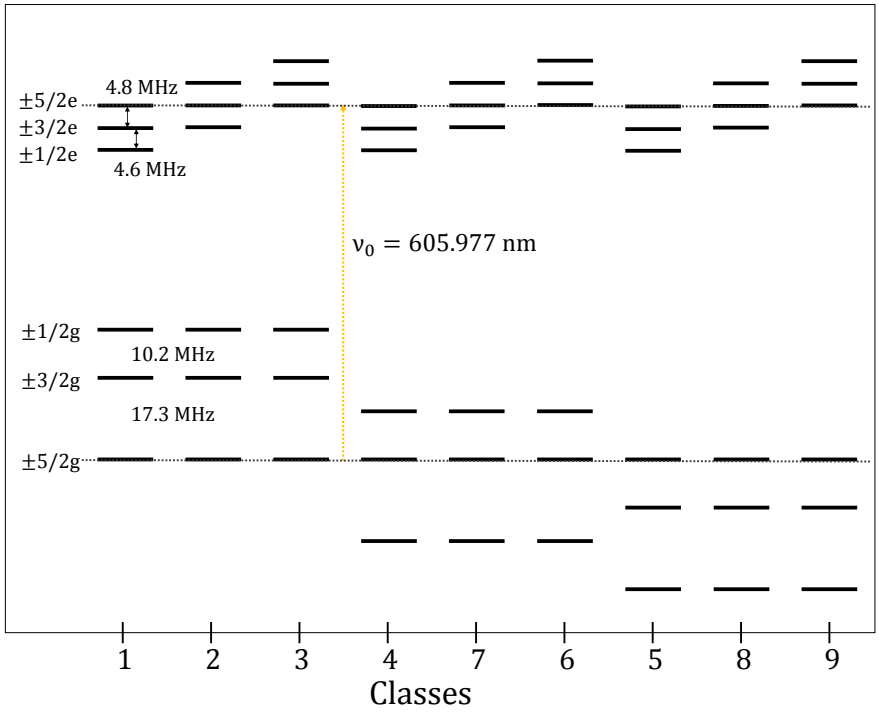

FIGURE 2.5: Hyperfine level structure of Pr^{3+} ions doped into Y_2SiO_5 crystal and excitation of different classes of ions due to the inhomogeneous broadening. Black dashed lines indicate the levels that are excited simultaneously.

ions substitute Y^{3+} ions in two different crystallographic sites without rotational point symmetry [77]. The probability for Pr^{3+} ions to occupy these sites are not equal, indeed one site (called *site 1*) is much more likely to be occupied than the other (*site 2*). This results in higher absorption for site 1. Similar to other quantum information experiments with Pr^{3+}:Y_2SiO_5, we also chose to work with the ions located in site 1 due to this high absorption. As we discussed earlier, the long-lived optical transition occurs between the lowest lying levels of the lower and upper crystal field manifolds. $^1D_2(0) \rightarrow {}^3H_4(0)$ transition in Pr^{3+} is an example to this kind of zero-phonon transitions. When doped into Y_2SiO_5 crystal this transition lies at 605.977 nm for site 1 and 607.934 nm for site 2, which are orange in colour. The axes of optic indicatrix of Y_2SiO_5 crystal are denoted as b, D_1

g/e	±1/2	±3/2	±5/2
±1/2	0.55	0.38	0.07
±3/2	0.40	0.60	0.01
±5/2	0.05	0.02	0.93

TABLE 2.1: Relative transition strengths between hyperfine $^1D_2(0)$ ground and $^3H_4(0)$ excited states (data taken from Ref. [78]).

and D_2 and are all mutually perpendicular [67]. The maximum absorption occurs when the polarization of the light is close to being parallel to the D_2 axis. The host crystal, Y_2SiO_5 has a refractive index of 1.809.

For site 1, the *homogeneous* linewidth (Γ_{hom}) is around few kHz. In our lab we measured optical T_1 of around 160 μs by fluorescence decay measurements (See Figure 2.3) which is lower than the previously reported value of 164 μs [77]. The T_2 time of the transition has been reported to be 111 μs under zero magnetic field [77] at a temperature of 1.4 K. By performing photon-echo experiments (for details see Sec. 3.1.3), we measured an average T_2 of around 63 μs in a 5-mm crystal, shown in Fig. 2.6. The experiment is repeated 10 times to have a better averaging. Fit to the best values gives a T_2 value of $\sim 87\,\mu$s. The measured values are compatible with the previously reported value of 111 μs which can be explained by taking into account the fact that our experiments were performed at a slightly higher temperature (~ 3 K). The variation of the measured values for each time delay can be explained by the fact that the experiment was not synchronized with the cryostat's cycle as explained in Sec. 4.2 and thus it was affected by the vibrations in the cryostat.

Pr^{3+} has a nuclear spin of $I = 5/2$ which gives rise to hyperfine levels ±1/2, ±3/2 and ±5/2 under zero external magnetic fields (Fig. 2.5). Each of these levels would further split under an applied magnetic field. The splitting of the hyperfine levels are usually very small, on the order of 10 MHz. These hyperfine levels usually have long coherence (T_2) and population lifetimes (T_1) (Eq. 2.3). For Pr^{3+}, the ground state hyperfine T_1 is on the order of a minute [79] and the T_2 is around 500 μs [80].

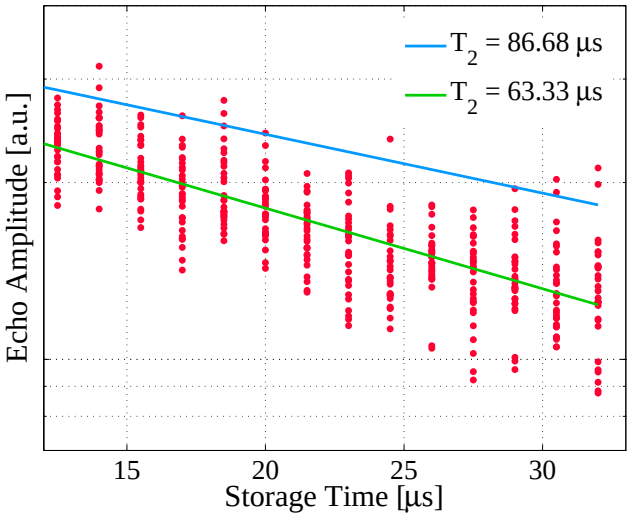

FIGURE 2.6: Measurement of T_2 by photon echo experiments. The experiment is repeated 10 times (red dots) for each time delay. Blue line is the fit to the highest value of each set, whereas the green line is the fit to the average of each measurement set.

Table 2.1 shows the relative transition strengths between different ground and excited hyperfine states. The strongest transition occurs between the $\pm 5/2_g - \pm 5/2_e$ states. However, the transition probabilities from $\pm 5/2_e$ to the other two ground states are almost negligible, which prevents to form a $\Lambda-$level system, having the $\pm 5/2_e$ state as the common excited state. Among all the possibilities, a $\Lambda-$level system can be formed with the ground states $\pm 3/2_g$ and $\pm 1/2_g$ connected to the common excited state $\pm 3/2_e$. This configuration is used in the experiments that are presented in Chapters 6 and 7.

2.5 Spectral hole burning

As we discussed above, in an inhomogeneously broadened medium different transitions can be excited by a single frequency field. In the case of Pr^{3+} all 9 possible transitions can be excited as shown in Figure 2.5. There are

numerous ions within the ensemble whose transition frequency is shifted such that only $\pm 5/2_g - \pm 5/2_e$ transition is resonant with the applied field. This group of ions is called a *class* (Class I in Figure 2.5). In this way there are 9 different classes of ions inside an ensemble as all the transitions can be excited due to the inhomogeneous broadening.

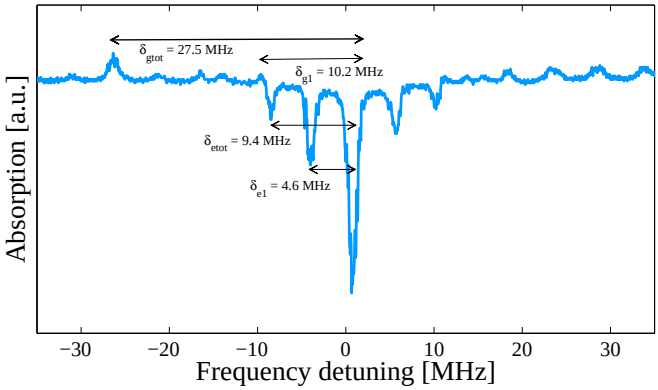

FIGURE 2.7: Experimental hole burning in Pr^{3+} :Y_2SiO_5 showing the hyperfine level seperations.

If a sufficiently long external laser pulse is applied such as the one represented with yellow dashed lines in Figure 2.5, then the ground state populations can be redistributed to other hyperfine levels. After such a pulse the $\pm 5/2_g$ state of the ions in classes I, II and III, the $\pm 3/2_g$ state of the ions in classes IV, V and VI and lastly the $\pm 1/2_g$ state of the ions in the last three classes would be empty and there would be a so-called *spectral hole* at this frequency. These structures are long-lived as the ground-state hyperfine population lifetimes are usually long as mentioned earlier.

However, at the frequency detunings corresponding to the ground state hyperfine level separations, there would be an excess of population that creates additional absorption that are so-called *anti-hole*s in the inhomogeneous line. The opposite effect would be observed at frequencies of excited state hyperfine level separations. Now, there would be again reduced absorption that results in *side-hole*s. So, in summary, exciting an ensemble

of inhomogeneously broadened rare-earth ions would create complex structures composed of holes and anti-holes. One example is given in Fig. 2.7, which also shows the hyperfine level separations from which the ground and excited state hyperfine structures can be reconstructed.

In principle one can create larger spectral holes by sweeping the frequency of the pump laser which are called *spectral pit*s in the community as well as in this thesis. The limit to which these larger pits can be burned is the difference between the ground and excited hyperfine levels. For Pr^{3+}, since the total ground state separation is larger than the one for the excited state, the width of such spectral pits is limited to 18.1 MHz. Larger structures are not possible as the anti-holes would start filling the spectral pit. Spectral hole burning can be used to isolate a single class of ions as described in Appendix D.

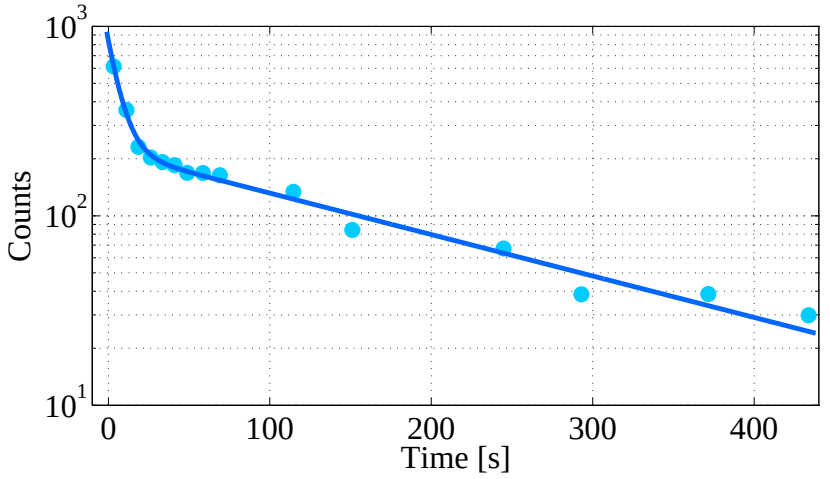

FIGURE 2.8: Double-exponential decay of the amplitude of a spectral hole. $\tau_1 \approx 7.5$ s and $\tau_2 \approx 198.5$ s.

Figure 2.8 shows the ground state hyperfine population decay of Pr^{3+} ions, clearly showing two distinct decay constants. This measurement is done at a sample temperature of $\sim 2.8\,\mathrm{K}$. According to Ref. [67] the shorter decay (τ_1) is due to the Orbach processes whereas the longer decay (τ_2) is due to the ion-ion interactions.

As we will see in the next sections, spectral hole burning techniques forms the basis of the Atomic Frequency Comb memory protocol [81] that we use in our experiments.

Chapter 3

Light-matter interaction and quantum memories

In this chapter, I will give a theoretical overview of light-matter interactions necessary to understand the experiments presented in this thesis. I will then describe several quantum memory protocols in detail with a special emphasis on the atomic frequency comb (AFC) technique. Finally, I will present a state of the art of solid state quantum memories based on rare-earth ion doped (REID) solids.

3.1 Coherent light-matter interactions

The very basic concept in quantum optics is a two-level system interacting with a radiation field (Fig. 3.1). Not only it provides a general framework to understand light-matter interactions, but also forms a basis for applications in quantum information science as almost any two-level system can be viewed as a qubit. Once the fundamental concepts are understood, the treatment of the two-level systems interacting with light can be extended to more complicated scenarios where other levels are also involved.

3.1.1 The semi-classical approach

The semi-classical approach, where the radiation is treated as a classical field and the atom is considered as a quantized two-level system is sufficient to demonstrate the underlying physics behind the most experiments shown in this thesis. In this section I will follow the approach taken in [82]. Fig.

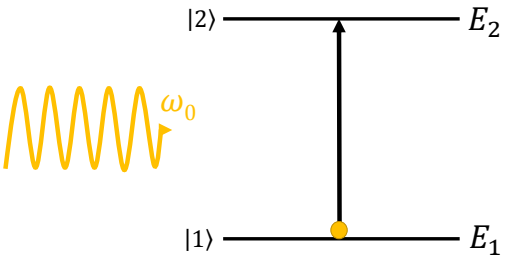

FIGURE 3.1: Simple representation of the interaction with a radiation of frequency ω with a two-level system with $E_2 - E_1 = \hbar\omega_0$, where $|\omega_0 - \omega| \approx 0$.

3.1 shows a basic example where a two-level system with eigenstates $|1\rangle$ and $|2\rangle$ with corresponding energies E_1 and E_2 is interacting with a radiation field with an angular frequency ω_0. The wavefunction of the two-level system is given by,

$$|\psi\rangle = c_1|1\rangle + c_2|2\rangle, \tag{3.1}$$

with time-dependent complex probability amplitudes, c_1 and c_2 ($|c_1|^2 + |c_2|^2 = 1$). The interaction Hamiltonian is given by,

$$\hat{H} = \hat{H}_0(\boldsymbol{r}) + \hat{V}(t) \tag{3.2}$$

where

$$\hat{V}(t) = V_{ij}(t) = -\frac{\mathcal{E}_0}{2}(e^{i\omega_0 t} + e^{-i\omega_0 t})\mu_{ij} \tag{3.3}$$

describes the time-dependent radiation field and $\hat{H}_0$ is the atomic Hamiltonian with $\hat{H}_0\psi_i = E_i\psi_i$, with $i = 1, 2$ and $E_2 - E_1 = \hbar\omega$. μ_{ij} is the dipole matrix element and $\mu_{11} = \mu_{22} = 0$ and $\mu_{12} = \mu_{21}$. If we solve the

Schrödinger equation with Eqns. 3.1 and 3.2 under the *rotating wave approximation* assuming the exact resonance condition $\omega = \omega_0$, c_1 and c_2 are found to be (with the initial conditions $c_1(0) = 1$ and $c_2(0) = 0$),

$$\begin{aligned} c_1(t) &= \cos(\Omega_R t/2), \\ c_2(t) &= i\sin(\Omega_R t/2), \end{aligned} \tag{3.4}$$

with the Rabi frequency, $\Omega_R = |\mu_{12}\mathcal{E}_0|/\hbar$. Eq. 3.4 describes an oscillatory behaviour of the system with a period of $2\pi/\Omega_R$. This oscillation is called the Rabi oscillation or the Rabi flopping. As can be seen from Eq. 3.4 the product $\Omega_R t$, which is called the *pulse area*, determines the distribution of the population between the ground and the excited states. Starting from the ground state, i.e. $c_1(0) = 1$, a pulse with an area $\pi/2$ brings the system into an equal superposition between the two states, whereas a pulse with an area π (also called a $\pi-$pulse) excites all the population to the excited state.

3.1.2 The Bloch sphere representation

If the quantum state at hand has to be described by an ensemble, then it can be represented by the atomic density operator [83],

$$\hat{\rho} = \rho_{11}|1\rangle\langle 1| + \rho_{12}|1\rangle\langle 2| + \rho_{21}|2\rangle\langle 1| + \rho_{22}|2\rangle\langle 2|, \tag{3.5}$$

where,

$$\rho_{ij} = \langle c_i c_j^* \rangle, \quad i, j = 1, 2. \tag{3.6}$$

The state can be geometrically described by a vector $\mathbf{r}$ with components u, v and w. These are related to the density matrix ρ as follows,

$$\begin{aligned} u &= 2\mathrm{Re}(\rho_{12}) \\ v &= 2\mathrm{Im}(\rho_{12}) \\ w &= \rho_{22} - \rho_{11}. \end{aligned} \tag{3.7}$$

In Eq. 3.7 w represents the population difference between the states $|0\rangle$ and $|1\rangle$. It takes a value of -1 if all the system is in the ground state and as explained in Sec. 3.1.1, a resonant $\pi-$pulse would bring the system to the excited state, with $w = +1$. The other two components represent the coherence between the two states. The **r** vector has a unit length and the surface that it can trace forms what is known as the Bloch sphere.

If we also include the decay terms T_2 and T_1 (see Eq. 2.3) under the rotating wave approximation, then the equations of motions for the **r** vector becomes [84],

$$\begin{aligned} \dot{u} &= -\delta v - \frac{u}{T_2} \\ \dot{v} &= \delta u - \frac{v}{T_2} + \Omega_R w \\ \dot{w} &= \frac{w - w_{eq}}{T_1} - \Omega_R v. \end{aligned} \tag{3.8}$$

In the above equations, δ is the detuning of the external field from the atomic transition. These equations are known as the optical Bloch equations and they describe the response of an atomic system to an external electric field. However, one should also consider the effect of the atoms back on the light field, in order understand the underlying physics behind quantum memory protocols. This brings us to the Maxwell-Bloch equations.

Application of a resonant external field would make the ensemble of the atoms oscillate, thus creates an oscillating polarization density $P(z,t)$ across the sample, expressed as

$$P(z,t) = N\mu_{12}\mathrm{Re}\left[\int_{-\infty}^{\infty} \left(u(z,t;\delta) - iv(z,t;\delta)\right) e^{-i(\omega t - kz)} g(\delta)\mathrm{d}\delta\right]. \tag{3.9}$$

Eq. 3.9 already depends on the atomic variables u and v. Here, N is the number of atoms in the ensemble and $g(\delta)$ is the spectral distribution of the atoms (represents the inhomogeneous broadening, see Sec. 2.3.2). If it is inserted in the Maxwell equation, and under the slowly varying envelope approximation (i.e. when the electric field amplitude $\mathcal{E}_0$ varies slowly), we

have [85]

$$\left(\frac{\partial}{\partial z} - \frac{n}{c}\frac{\partial}{\partial t}\right)\Omega_R(z,t) = \frac{i\alpha_0}{2\pi}\int_{-\infty}^{\infty}\left[u(z,t;\delta) - iv(z,t;\delta)\right]g(\delta)\mathrm{d}\delta, \quad (3.10)$$

where α_0 is the optical depth of the ensemble. This equation tells that the electric field and thus the Rabi frequency, Ω_R, is modified by the atomic polarization already induced by that electric field. It is this modified electric field that now acts on the atoms, completing the mathematical description. Equations 3.8 and 3.10 are known as Maxwell-Bloch equations.

One can also define the atomic polarization, $\sigma(z,t;\delta)$, corresponding to atoms with a detuning δ as,

$$\sigma(z,t;\delta) = u(z,t;\delta) - iv(z,t;\delta). \quad (3.11)$$

With this, the Maxwell-Bloch equations can also be written as follows [81, 86]

$$\begin{aligned}\frac{\delta}{\delta t}\sigma(z,t;\delta) &= -i\delta\sigma(z,t;\delta) + i\mu_{12}^2\Omega_R(z,t)/\hbar \\ \left(\frac{\partial}{\partial t} + c\frac{\partial}{\partial z}\right)\Omega_R(z,t) &= \frac{i\omega_0\hbar}{2\epsilon_0 V}\int_{-\infty}^{\infty} g(\delta)\sigma(z,t;\delta)\mathrm{d}\delta.\end{aligned} \quad (3.12)$$

Here, ϵ_0 is the vacuum permittivity and V is the quantization volume. This notation will be quite convenient in the analytical treatment of the AFC method (Sec. 3.3).

3.1.3 Two-pulse photon echo

The inhomogeneous absorption line, $g(\Delta)$, can be probed with several methods among which a common is the two-pulse echo (2PE) technique [87]. It starts with an ensemble of atoms initially in the ground state ($w = -1$, $u = v = 0$ in Eq. 3.7). The application of a short $\pi/2$ pulse brings the system to the $u - v$ plane (I in Fig. 3.2), which creates a collective dipole oscillating all in-phase. This collective dipole oscillation

results in the emission of a coherent radiation, called the *free induction decay* (FID). This will be a source of noise in the experiments presented in Chapter 7. Duration of the FID is usually short, similar to that of the excitation pulse.

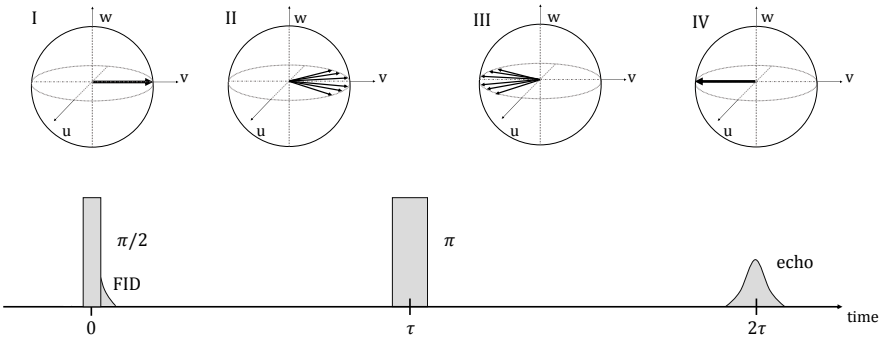

FIGURE 3.2: Upper panel shows the Bloch sphere representation of the two-pulse echo technique, whereas the time sequence of the pulses is shown below. (I) shows the atomic state upon the application of a $\pi/2$ pulse. A π pulse is applied between (II) and (III) after a time τ that rotates the vectors around the X axis. This results in the rephasing of the atomic coherence and produces a coherent emission (IV).

After the application of the $\pi/2$ pulse, the frequency detuning $g(\Delta)$ would cause individual atoms to oscillate at slightly different frequencies and thus they start dephasing with respect to each other (II). The application of a π pulse a time τ after the $\pi/2$ pulse rotates each Bloch vector 180 ° around the u axis (III). The atoms would continue to oscillate at different frequencies, however a time τ after the π pulse they would be all in-phase again. The collective dipole oscillation results again in a coherent radiation, which is called the *photon echo*. In this sense the photon echo can be interpreted as the revival of the FID that would already be lost if no rephasing pulse was applied. A detailed analytical treatment can be found in Refs. [84, 88].

2PE is quite a powerful tool to measure the coherence time, T_2 of an inhomogeneously broadened optical transition. Performing a 2PE experiment repeatedly by changing the delay, τ, between the pulses and monitoring

the echo intensity, one can infer the coherence time T_2. The echo intensity depends on τ as follows [89],

$$I(t) \sim e^{-4\tau/T_2}. \tag{3.13}$$

We used this method to determine the T_2 of the optical transition we used in our experiment as explained in Sec. 2.4 and shown in Fig. 2.6.

2PE and its modified version that uses two $\pi/2$ pulses for the rephasing instead of a single π pulse (this method is called *three-pulse echo*) attracted much attention for optical data storage applications [90, 91] especially after narrow-linewidth, tunable dye lasers became widely available. Storage of 25 bits of optical information in a Pr^{3+} :YAG crystal [92], 248 bits in a Eu^{3+} :$YAlO_3$ crystal [93] and 1020 bits in Er^{3+} :Y_2SiO_5 crystal [94] have been demonstrated.

These developments opened prospects for quantum information storage with REID systems. Nevertheless, it has been shown that neither of these techniques could allow performing the task of quantum information storage [95, 96], due to the fact that the inherent noise associated to these techniques would not allow one to reach a sufficient signal-to-noise ratio. Highly modified versions of these protocols have been proposed for quantum information storage purposes [97, 98] and the first of these has been also demonstrated experimentally [99]. However the protocol presented in Ref. [98] is yet to be demonstrated in the quantum regime.

3.2 Quantum memory protocols

An optical quantum memory is a device that can faithfully store and recall the stored quantum information carried by light on-demand [47, 49]. It is essential in many applications in quantum information science as being an interface between flying and stationary qubits. The flying qubits are encoded in different degrees of freedoms in photons propagating either in

free space or through optical fibres. Different physical systems can be used for the implementation of the stationary qubits. Stationary qubits can be realized by using the internal states of single absorbers, such as, single trapped ions or single atoms in optical cavities or by mapping the state of the incoming photon to the collective atomic excitations in an ensemble of atoms. These systems include, but are not limited to warm atomic vapors, cold atomic ensembles, Bose-Einstein condensates and REID systems, such as our system. In this section I will overview some of the well-established optical quantum memory protocols realized in solid-state ensembles. Then, I will present a detailed view on the Atomic Frequency Comb (AFC) technique that forms the backbone of the work presented in this thesis.

3.2.1 Electromagnetically induced transparency

Electromagnetically induced transparency (EIT) was first observed in 1991 [100]. It is a coherent quantum optical effect that arises from the destructive interference between the excitation pathways, $|b\rangle - |a\rangle$ and $|b\rangle - |a\rangle - |c\rangle - |a\rangle$ (Fig. 3.3(a)). This interference results in the modified optical response of the medium, as seen in Fig. 3.3(b). The susceptibility, $\chi = \chi' + i\chi''$, of the medium is modified such that, when the two beams are resonant with the corresponding transitions, the medium becomes extremely dispersive, whereas, at the same time the probe field experiences a transparency over a narrow bandwidth, determined by the Rabi frequency of the strong control beam. This behaviour is shown in Fig. 3.3(b). The blue curve shows the real part of the susceptibility of the medium, χ' under the EIT conditions. It shows a narrow transmission window within the absorption line. However, the importance of EIT in the light of coherent light storage becomes apparent if we look closer to the orange curve. It shows the imaginary part, χ'' of the susceptibility, which is related to the dispersion of the medium. The sharp slope around 0 detuning results in a reduced group velocity of light. This feature, when combined

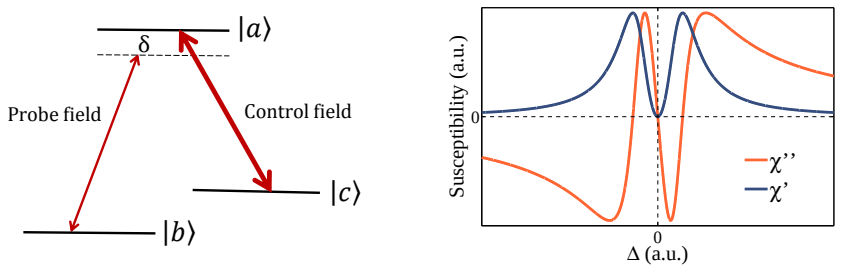

FIGURE 3.3: (a) Level diagram for EIT. A strong resonant field couples the states $|c\rangle$ and $|a\rangle$. (b) Real (χ') and imaginary (χ'') parts of the material susceptibility under the EIT condition.

with the transmission window over the same spectral region enables one to achieve ultralow group velocities and full transparency in an otherwise opaque medium. The first slow-light experiment based on this technique was reported in 1999 [101] where the group velocity of a light pulse was reduced to a mere 17 m/s. Later on, it was proposed [102] and shown that switching off the control beam after a pulse of light at the probe frequency enters the medium can completely stop the pulse inside the medium. The stopped pulse can be retrieved back later by switching the control beam on again, as demonstrated in Ref. [103, 104]. One of the first stopped light experiments based on the EIT method was performed with the Pr^{3+}:Y_2SiO_5 crystal [105]. This very early experiment in the field already demonstrates the promise of the REID based systems.

The technique was extended to the storage of single-photon level pulses in cold trapped atoms [106, 107] and warm atomic vapours [108]. Later advances include the storage of classical light in a Pr^{3+}:Y_2SiO_5 crystal on the order one second [109] and more recently the record-breaking one minute [110]. It was also demonstrated with single [111] and ensemble [112] of atoms trapped in optical cavities. Storage and retrieval of classical pulses with an efficiency of 78 % has been demonstrated with a cold ensemble of Rb atoms [113] and with 50 % with single-photon level pulses [114].

However, EIT comes with its own limitations too. The first is the limited bandwidth of the EIT tranmission window -typically few hundred kHz or few MHz, depending on the physical system and the Rabi frequency of the control field. Another limitation that the EIT possesses for especially single photon level light storage is the resonant character of the technique which would add excess noise [115]. Additionally, the fact that the control beams have to be on during the readout process adds extra noise. Lastly, the number of modes, N that can be stored in the memory scales as $\sqrt{d}$, where d is the optical depth of the medium [116]. Achieving high efficiency storage of several temporal modes is extremely challenging as it requires extremely high OD. This limitation practically makes EIT-based memories single mode memories in time.

3.2.2 Controlled reversible inhomogeneous broadening

Controlled reversible inhomogeneous broadening, known shortly as CRIB is another type of optical memory protocol where the inhomogeneous broadening in the optical transition is exploited. It was initially proposed for Doppler-broadened atomic gases [117], but it later found its use in rare-earth doped systems as well [118, 119]. These first experiments in solid state media were performed with classical pulses, but again, the results were later on extended to the single-photon level [120, 121]. The schematic of the CRIB protocol is shown in Fig. 3.4. The procedure starts with an inhomogeneously broadened atomic ensemble. Firstly, a narrow absorbing peak containing many atoms is created within a transparency pit inside the inhomogeneous line. This is realized by spectral hole burning methods described in Sec. 2.5 (Fig. 3.4(a)). Afterwards a transverse external electric field is applied to induce frequency shifts in the optical transitions of the atoms due to the linear dc-Stark effect (Fig. 3.4(b)). The input light whose bandwidth matches that of the broadened absorption feature is then sent into the ensemble. After the absorption the atomic coherence starts to dephase due to this controlled broadening of the initial absorption peak.

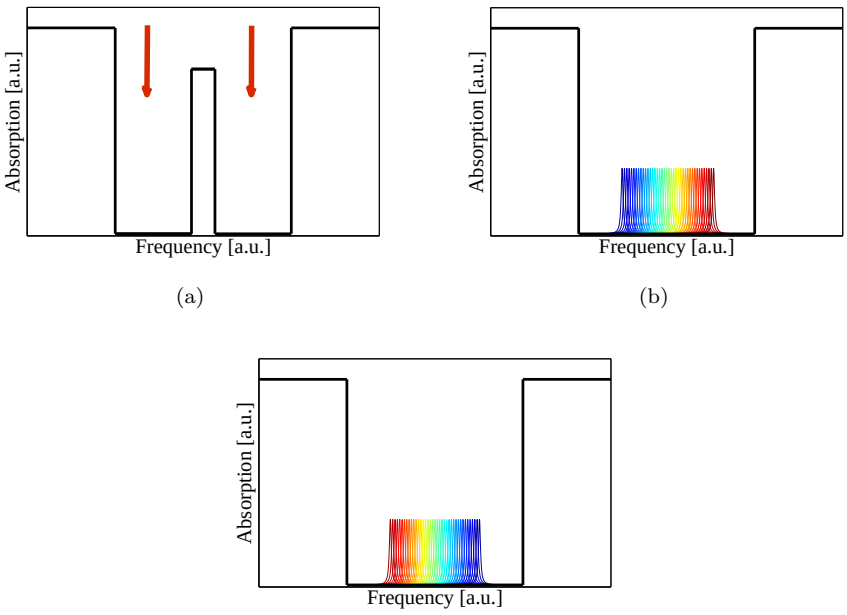

FIGURE 3.4: The basics of CRIB. (a) A narrow absorption feature is prepared within a larger transparency window by spectral hole burning methods (Sec. 2.5).(b) An electric field is applied to broaden the narrow absorption peak. (c) The polarity of the electric field is reversed after the input pulse is absorbed. Re-emission is triggered by this reversal of the electric field polarity.

The polarity of the external field is reversed to rephase the coherence and hence to recall the absorbed pulse in a photon echo fashion. The efficiency of the process is given by [120]

$$\eta_{CRIB}(t) = d^2 e^{-d} e^{-t^2\hat{\gamma}^2}. \tag{3.14}$$

In the above equation, d is the optical depth of the broadened absorption feature and $\hat{\gamma} = 2\pi\gamma$ representing the spectral width of the initial absorbing peak. However, the efficiency given by Eq. 3.14 is limited to 54% due to the re-absorption in the forward direction. However, as I will discuss for the case of the AFC method, a pair of strong control pulses can in principle be applied to transfer the optical coherence to the low-lying spin-states.

If implemented with counter-propagating control pulses, it can enable a storage and recall process with unit efficiency [86]. It would also offer longer storage times, if spin-states with long coherence time are chosen.

Another method to overcome the problem of the limited efficiency is to apply the electric field longitudinally, so that its amplitude depends on the propagation direction, hence inducing different frequency shifts in atoms at different locations in the ensemble which, as a result, prevents the re-absorption of the emitted echo. This variant of the CRIB method is called the *Gradient Echo Memory* (GEM) and was first proposed in Ref. [119] in 2006 and demonstrated in 2008 [122]. The process is perfectly efficient in the limit of large optical depth. A record 69 % storage efficiency was reported with GEM-based memory in 2010 [121]. This result marks the highest efficiency with REID systems to date. The experiment made use of a 14 mm long Pr^{3+}:Y_2SiO_5 crystal in which a 140 kHz wide narrow peak having an absortion of 140 dB (OD $\sim$ 32) was prepared. Apart from the high efficiency, the results are also important in the sense that the weak coherent states are stored and recalled with a performance surpassing the no-cloning limit [4, 5]. Different version of GEM, called $\Lambda-$GEM, has also been proposed and demonstrated [123] as a Raman process in atomic gases, with a controlled and reversible broadening of the spin transition [124]. A storage and recall efficiency of up to 87 % has been demonstrated with classical pulses in a warm Rb vapor system with this protocol [125]. Other significant experiments include coherent pulse sequencing [124] and the a highly efficient (84 %) unconditional quantum memory for weak coherent pulses [126].

One can store multiple temporal modes with the CRIB method, with a scaling $N \sim d$ [127]. However, the drawback of this technique is that the OD of the initial peak is reduced after it is broadened by the applied external electric field. So, one still needs very high optical depths due the this reason.

Nevertheless, it has a particular advantage stemming from the fact that the spectral width of the peak can be dynamically changed with the external field. The field can be switched off to narrow the peak, so that the transfer to the long-lived spin-states with control pulses would be much easier. So far, the only CRIB experiment featuring the transfer of the coherence to and from the spin-states has been performed with an efficiency of $\sim 3{\cdot}10^{-4}$ [128].

3.3 Atomic Frequency Comb Technique

The atomic frequency comb (AFC) method is a promising memory protocol based on the rephasing of atomic coherences. Rephasing is based on the periodic absorption features engraved in the inhomogenously broadened absorption profile of the medium. This method has been proposed by Afzelius *et. al* [81] in Geneva in 2008. The first experimental demonstration also came from the same group that at the time included the director of this thesis [129]. All the light storage experiments presented in this thesis are performed with this technique.

The technique assumes an inhomogeneously broadened ensemble of atoms as a storage medium, and unlike the CRIB method, it does not require the use of a Stark shift. It requires at least three ground levels $|g\rangle$, $|s\rangle$ and $|aux\rangle$ that have a common excited state $|e\rangle$. These ground levels can be Zeeman or hyperfine levels, depending on the particular atom of interest. Furthermore, it requires the optical homogeneous linewidth γ_h to be much smaller than the inhomogeneous broadening Γ_{inh} ($\gamma_h \ll \Gamma_{inh}$). These conditions can easily be satisfied with rare-earth ion doped (REID) solids as we discussed in Chapter 2.

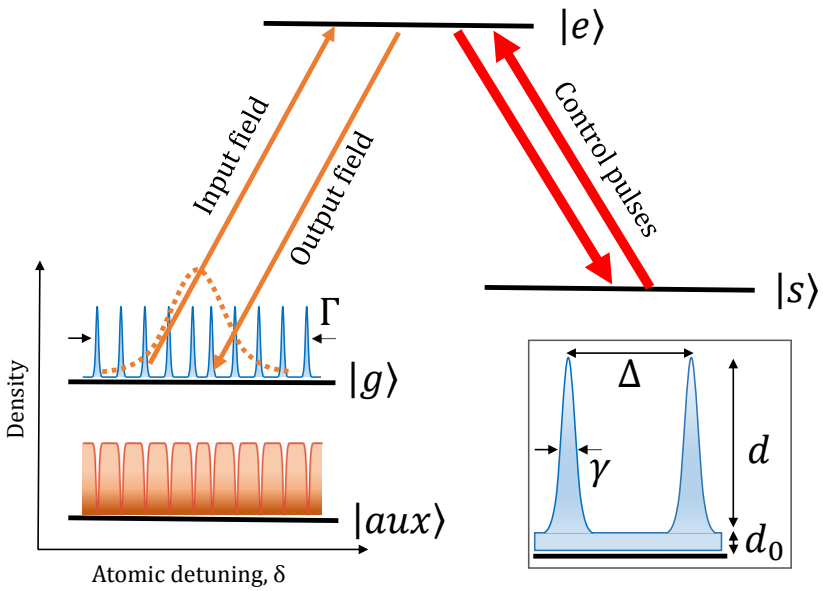

(a)

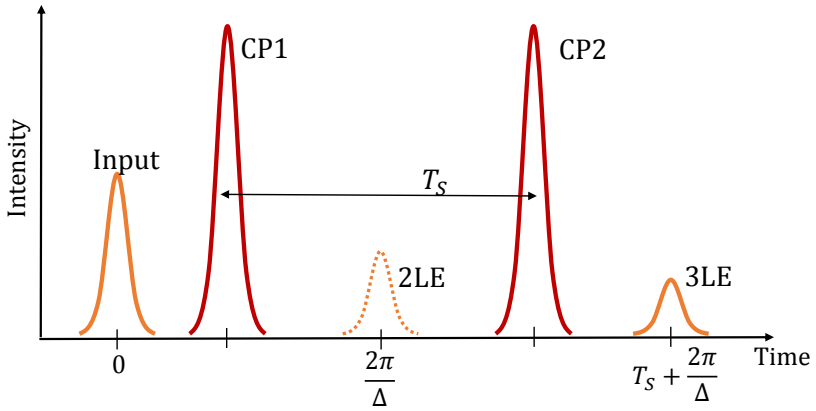

(b)

FIGURE 3.5: (a) Schematic description of the AFC technique. Details are in the text. Inset: Zoomed view of the comb. (b) Timing sequence of the storage and retrieval. CP1 and CP2 are the control pulses. 2LE is the AFC rephasing in the absence of CP1. 3LE is the retrieved signal with the full AFC protocol.

3.3.1 Storage in the excited state

The protocol starts with the creation of periodic absorption peaks on the $|g\rangle - |e\rangle$ transition by means of optical pumping. Here, the suitability of REID systems for spectral hole burning comes into play. The peaks of the AFC can be tailored with the hole burning methods described in Section 2.5. Another ground level, denoted as $|aux\rangle$ in Fig. 3.5(a) can be used as a shelving level for the transfer of the unwanted ions that are spectrally located between the individual AFC peaks (additional detail can be found in Appendix D).

After the preparation of the AFC, a single-photon level light pulse having a spectral width of γ_p is sent to the medium. The pulse is resonant with the $|g\rangle - |e\rangle$ transition. We assume the following condition holds true

$$\Delta \ll \gamma_p \ll \Gamma, \tag{3.15}$$

where, Γ is the overall spectral width of the AFC and Δ being the separation between peaks in an AFC. The overall quantum state after the mapping can be expressed as a Dicke state,

$$|\psi\rangle = \sum_{i=1}^{N} c_i e^{i\delta_i t} e^{-ikz_i} |g_1 \cdots e_i \cdots g_N\rangle. \tag{3.16}$$

Here z_i is the position of the ith atom, k is the wavenumber of the light field, δ_i is the frequency detuning of the ith atom and c_i is the amplitude depending on the frequency and position of the specific atom. Eqn. 3.16 describes a single excitation delocalized over N atoms, called *collective atomic excitation*. After the mapping each atom oscillates with a slightly different frequency with respect to each other due to the frequency detuning introduced by the inhomogeneous broadening, thus the collective state dephases quickly. However, in the presence of the AFC with sharp peaks, i.e. when Eqn. 3.15 is satisfied, the frequency detuning can be replaced by equally spaced peaks as $\delta_i = m_i\Delta$, where m_i are integers. This now

results in the rephasing of the collective state after a time $\tau = 2\pi/\Delta$. A photon-echo like coherent re-emission in the forward direction is observed as all the atoms would oscillate in-phase. Similarly to CRIB, the efficiency of this process is limited to 54 % due to the reabsorption of the emitted light by the absorbing medium.

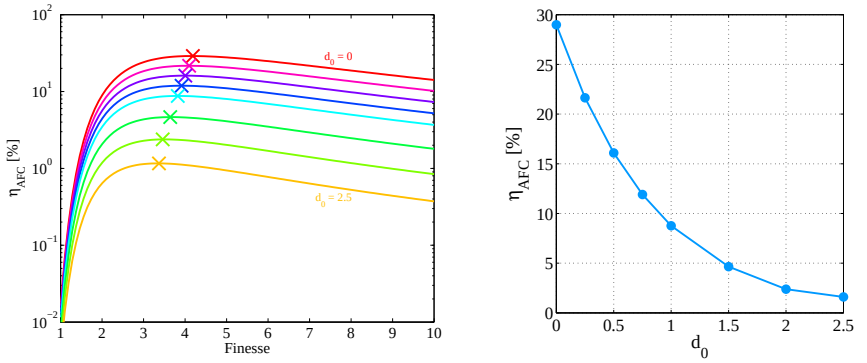

FIGURE 3.6: (a) Two-level AFC storage efficiency with respect to the comb finesse. Different curves represent different AFCs with increasing background absorption, d_0. The maximum achievable peak OD $(d + d_0)$ is taken to be 5. Crosses mark the maximum efficiencies for each curve, which are plotted separately in (b).

The analytical treatment of the method is based on the Maxwell-Bloch equations introduced in Sec. 3.1.2. Here, it is assumed that strong control pulses are applied at time $t = 0$ and there is no decoherence in the ground states for the simplicity of the calculations. Any decoherence can then be conveniently introduced as a loss [129]. The main idea is to treat the atomic distribution $g(\delta)$ as a series of Gaussian peaks as following,

$$g(\delta) \propto e^{-\delta^2/\left(2\Gamma^2\right)} \sum_{j=-\infty}^{\infty} e^{-(\delta - j\Delta)^2/\left(2\tilde{\gamma}^2\right)}, \tag{3.17}$$

and then to solve Eqns. 3.12 to find a mathematical expression for the re-emitted field. The output in the forward mode is given by [81],

$$E_{\text{out}} = -E_{\text{in}} e^{-(\pi^2/4\ln 2\, F^2)} \tilde{d}\, e^{-\tilde{d}/2}, \tag{3.18}$$

where $F = \Delta/\gamma$ is the finesse of the comb with γ being the peak width, $\tilde{d} \approx d/F$ is the effective optical depth experienced by the absorbed pulse with d being the maximum optical depth. The efficiency is then given by the ratio of the energy of the output field to the one of the input,

$$\eta = \frac{|E_{\text{out}}|^2}{|E_{\text{in}}|^2}. \tag{3.19}$$

Eq. 3.18 can then be used to approximate [81, 129] the efficiency and the result is,

$$\eta_{\text{AFC}} \approx \tilde{d}^2\, e^{-7/F^2}\, e^{-\tilde{d}}\, e^{-d_0}, \tag{3.20}$$

where d_0 is the absorbing background as shown in the inset of Fig. 3.5. Figure 3.6(a) shows the two-level storage efficiency, η_{AFC}, plotted versus the comb finesse with different background absorption values, d_0. As we will see in the relevant sections, the imperfect preparation of the AFC might result in an absorbing background, which in the end degrade the storage efficiency. In this plot the maximum optical depth of an AFC is taken to be 5, which is usually the case for our experiments. As can be seen from the Fig. 3.6(b), η_{AFC} can be as high $\sim 29\,\%$ for $d_0 = 0$, however, a realistic $d_0 = 0.5$ would yield $\eta_{\text{AFC}} \sim 16\,\%$. This clearly demonstrates the importance of the optical pumping for the AFC preparation.

Just after the first AFC proposal, it was shown that the optimum peak shape in an AFC is square [130]. Intuitively, it can be thought that the larger number of atoms in a square peak than those are in a Gaussian peak accounts for the higher achievable efficiency. Quantitatively, the efficiency, η_{AFC}, is given as [130, 131],

$$\eta_{\text{AFC}} = \tilde{d}^2\, e^{-\tilde{d}}\, \text{sinc}^2(\pi/F). \tag{3.21}$$

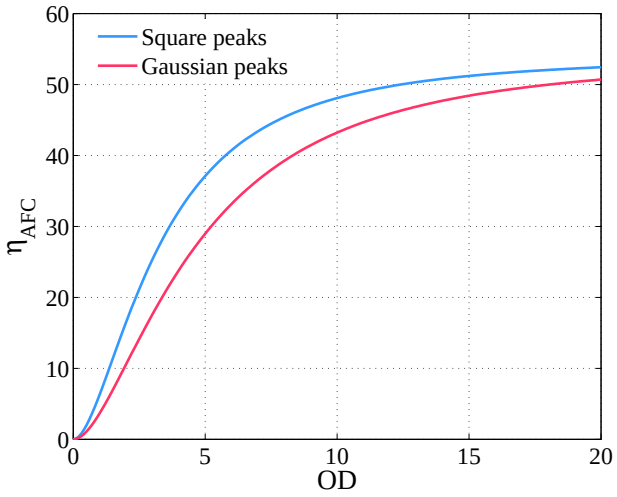

FIGURE 3.7: Comparison of the maximum obtainable AFC efficiencies with Gaussian (red curve) and square-shaped (blue) combs

On the other hand, the optimum finesse, F, that gives the maximum η_{AFC} for a given d is expressed as,

$$F_{\mathrm{opt}} = \frac{\pi}{\arctan(2\,\pi/d)}. \tag{3.22}$$

The maximum obtainable AFC efficiencies for Gaussian and square peaks are plotted in Fig. 3.7. As an example, with an optimized finesse, an AFC with Gaussian peaks would produce echoes with $\approx 29\,\%$ efficiency for $d = 5$, whereas with the same d one can reach $\eta_{\mathrm{AFC}} \approx 37\,\%$.

3.3.2 Full AFC scheme with spin-state storage

So far we only considered the storage in the excited state without the transfer of the stored excitation to another ground state $|s\rangle$. The protocol only offers a preprogrammed storage times set by the AFC spacing, Δ. AFC storage in the excited can be useful if it is combined with huge spectral multiplexing capability and deterministic single photon sources [132]. Also, similar results could be obtained by sending the light through a long

enough optical fibre, though in this case the efficiency is limited by the losses. However, the AFC storage in the excited state might offer a better performance than an optical fibre delay line since an efficiency of 54 % can be attainable.

On the other hand, the full AFC scheme offers on-demand retrieval of light which is necessary for many quantum information and communication applications [133]. This can be realized by the use of strong control pulses to coherently transfer the excitation to and from long-lived spin states.

The stored excitation needs to be transferred before the re-emission time τ. Once the coherence is transferred to a spin-wave, for example by a single frequency π-pulse, the optical dipole evolution is effectively frozen. To read-out this spin-wave, a second transfer pulse is applied after a time T_S, resulting in a three level echo (3LE) with a total storage time of $\tau + T_S$. The time sequence of such an experiment is shown in Fig. 3.5(b). If each transfer pulse has an efficiency of η_{T}, then the total efficiency is given by [134]

$$\eta_{\mathrm{3LE}} = \eta_{\mathrm{AFC}} \times \eta_{\mathrm{T}}^2 \times \eta_{\mathrm{C}}, \tag{3.23}$$

where η_{AFC} is the two-level AFC echo efficiency and η_{C} is the decoherence during the storage in the spin states. The transfer efficiency can be further optimized by the use of chirped pulses, as theoretically discussed in [135].

An additional benefit of the full AFC scheme is that the control pulses can be applied in the counter propagating direction to the input pulse, as in the CRIB proposal. This allows the backward retrieval of the echo which could enable a storage and retrieval efficiency of 100 % [81]. In this case, and for Gaussian AFC peaks (Eq. 3.17), the efficiency is given as,

$$\eta_B \approx (1 - e^{-d/F})^2 e^{-7/F^2}. \tag{3.24}$$

This enhanced efficiency can be reached thanks to the elimination of the reabsorption of the emitted echo by the medium that happens during the retrieval in the forward direction. One advantage of AFC over CRIB is

that the number of stored modes, N scales with the number of teeth in the AFC, independent of the optical depth, d. This can simply be understood after noting that $N \propto \tau_{\mathrm{AFC}}/\tau_p$, where $\tau_p = 2\pi/\gamma_p$ is the duration of an individual input pulse and the storage time in the excited state, τ_{AFC}. In a realistic experiment one has $\gamma_p \approx \Gamma$. Since $\tau_{\mathrm{AFC}} = 2\pi/\Delta$, now we have $N \propto \Gamma/\Delta = n_{peaks}$.

The main limitation of the AFC is its bandwidth. The width of the AFC that can be created within an inhomogeneously broadened medium is limited by the hyperfine level splittings (given that these splittings are much smaller than the inhomogeneous broadening), for high-finesse combs. This is on the order of few MHz for Pr^{3+} and few tens of MHz for Eu^{3+}.

3.3.3 State-of-the-art with AFC memories

Numerous significant experiments have already been performed with the AFC method.

The first experimental demonstration of the protocol came in 2008 [129]. Weak coherent states at the single photon level were stored in the memory with predetermined storage times of up to $\sim 1\,\mu$s. The coherence of the stored pulses were shown to be preserved by implementing a *double-AFC* scheme, where two different AFCs with different Δ were prepared simultaneously in the crystal. This results in two distinct echoes at the output for any given input pulse. In this way the memory can act as a Mach-Zender interferometer and can be used to quantitatively evaluate the preservation of the coherence during the storage. Raw visibility of around 86 % has been observed. Detector dark count subtraction resulted in a visibility of $\sim 95\,\%$

Temporal multimode storage capability of the AFC was also investigated in different experiments and thus in different physical systems. The first experiment was performed again by the Geneva group in 2010 with Nd^{3+}:Y_2SiO_5 [136]. Nd^{3+} does not possess the extra ground level that is required for the

spin-state storage ($|aux\rangle$ in Fig. 3.5(a)). However, the splitting between the ground states are much larger than that of the Pr^{3+}. This allows one to create spectrally larger AFCs which in the end increases the number of modes that can be stored. In the above-mentioned experiment, a 100 MHz-wide AFC was created and a train of 64 pulses, with each having mean photon numbers, $\bar{n} \leq 1$, were stored and recalled after a predetermined time of 1.32 μs. The other experiment where a high number of temporal multimodes were stored was performed in 2011 [137] with the Tm^{3+}:YAG system. In this case, an AFC with a spectral width of 0.93 GHz was prepared to store 1060 temporal modes. In this case, the predetermined storage time was 1.6 μs. The reported efficiency was around 1 %. The comb preparation method employed in this experiment intrinsically limited the comb finesse, which contributed the relatively low storage and retrieval efficiency. This experiment was performed with bright light unlike the case of Nd^{3+} :Y_2SiO_5 [136].

Other experiments focused on the quantum aspects of the protocol by characterizing the performance of the storage devices in view of applications in quantum information and communication science. The first experiments include the storage of photonic entanglement in a crystal [138, 139]. The groups of Nicolas Gisin in Geneva and Wolfgang Tittel in Calgary were able to store a single photon from an entangled photon pair source with a Nd^{3+}:Y_2SiO_5 crystal and a Ti:Tm:$LiNbO_3$ waveguide, respectively. It was shown that the entanglement between the photons in the pairs were preserved after one of the photons was stored in the crystal. These experiments paved the way to other significant experiments, such as the heralded entanglement between two crystals [140] and storage of time-bin qubits in the excited states of a large bandwidth, waveguide memory [141]. Later on, the Calgary group went on to extend the capabilities of large bandwidth AFC memories to an on-chip integrated processor, where various tasks, such as sequencing, time-to-frequency multiplexing and demultiplexing, splitting, temporal and spectral filtering and compressing and stretching can be performed [142]. Other significant experiments from the Calgary

group included the demonstration of two-photon interference between weak coherent pulses recalled from separate memories [143]. Finally the group has recently demonstrated an Er^{3+} doped fiber memory operating at the telecom wavelength 1532 nm, albeit with short storage times of around few ns [144]. In our lab, we demonstrated the storage of heralded single photons from an ultra-narrow band spontaneous parametric down conversion source [62] with predetermined storage times of up to 4.5 μs [145] in a Pr^{3+}:Y_2SiO_5 crystal.

The full AFC protocol, where the input light is transferred to the spin-states was demonstrated in 2010 [134] with the Pr^{3+}:Y_2SiO_5 system. Although this experiment was performed with bright pulses, it stimulated further efforts in extending the full method to single-photon level pulses. Here the efficiency, $\eta_{3\mathrm{LE}}$, was limited to $< 1\,\%$ due to the low d and imperfect spatial overlap between the input and the control pulse modes. Also, the storage of two temporal modes in the spin-states was demonstrated as well. The only other REI that allows storage in spin-states is Eu^{3+}. It has several advantages over Pr^{3+}, the first of which is the longer coherence times. Ground state coherence time of 6 hours has been recently reported [146]. The second advantage is that the hyperfine separations are much larger than that of Pr^{3+}. However, these advantages come with the expense of lower oscillator strengths. The first full implementation of the AFC method with Eu^{3+} came in 2012 [147]. This experiment was performed with bright pulses and later extended to weak coherent pulses with $\bar{n} \approx 2$ [148].

Another line of research with AFC memories involves placing the memory crystal inside an impedance-matched cavity, as proposed in Ref. [149]. There have been several experiments, all performed with classical light. The first two of these came from Lund with Pr^{3+}:Y_2SiO_5 [150, 151] and they were followed by an experiment from Geneva with a Eu^{3+}:Y_2SiO_5 crystal [131]. The reported two-level efficiencies, η_{AFC}, were 22 %, 56 % and 53 %, respectively. Additionally, the Geneva experiment also featured

the transfer of the excitations to the long-lived spin-states with efficiency, $\eta_{3\mathrm{LE}} = 12\,\%$.

Our contributions also focused on the quantum aspects of the AFC protocol. As will be discussed in Chapter 5, we demonstrated the storage and recall of polarization qubits encoded with weak coherent states [152]. Two independent experiments reporting similar results were also published along our work [153, 154]. We later performed the first spin-wave AFC experiment to show that the coherence is preserved during the storage and retrieval process [155]. This experiment formed the basis of the final result of this thesis, namely the first storage and on-demand recall of time-bin qubits from a spin-wave optical memory [156].

Chapter 4

Experimental setup

In this chapter I will give details about the experimental setup and basic techniques we used throughout the course of this PhD study. Keeping in mind that our main goal is to perform coherent light-matter interaction experiments, the necessity of having a narrow-linewidth light source becomes clear. The other reason on the necessity of having a narrow-linewidth laser is to make use of the narrow linewidth of the optical transition in Pr^{3+} ions, which is around 2 kHz. In this respect, I will first describe the two laser systems and the stabilisation setup that we set up in our lab. Then I will outline the technical properties of the cryostat, detectors, pulse preparation and the control electronics.

4.1 Light Sources

I should first note that when embedded in a Y_2SiO_5 matrix, Pr^{3+} ions have a transition frequency at 606 nm which was mostly achievable with dye lasers. However since it is first, not cost-effective and second, hard to operate and stabilise due to high frequency noise associated with the dye jets (e.g. fluctuations in the density of the liquid dye), we decided build

our own 606 nm light source with sum frequency generation (SFG) out of 987, nm and 1569, nm extended cavity diode lasers (ECDLs).

4.1.1 Sum frequency generation and quasi-phase matching condition

In this section I will outline the theoretical basis for the SFG and describe quasi-phase matching (QPM) condition to achieve efficient wavelength conversion.

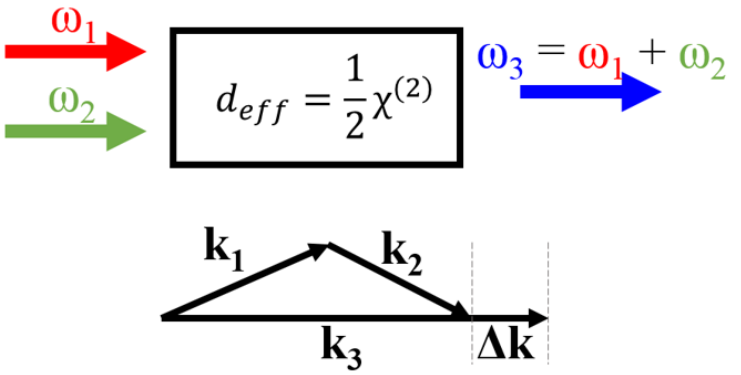

FIGURE 4.1: Sum frequency generation.

SFG is a second-order nonlinear process which means that it arises from $\boldsymbol{\chi^{(2)}}$ nonlinearity in the medium. Only the crystals that do not show inversion symmetry can allow such processes. SFG, second-harmonic generation (SHG), difference frequency generation and spontaneous parametric down conversion are examples of second-order nonlinear processes.

Fig. 4.1 depicts the basic principles of SFG. Two different strong light fields with frequencies ω_1 and ω_2 enter in a nonlinear material where the $\boldsymbol{\chi^{(2)}}$ nonlinearity produces the third field with frequency ω_2. d_{eff} represents the effective nonlinearity of the material. $\mathbf{k_1}$, $\mathbf{k_2}$ and $\mathbf{k_3}$ are the associated wavevectors of the two input fields and the output field. $\boldsymbol{\Delta k} = \mathbf{k_1} +$

$\mathbf{k_2} - \mathbf{k_3}$ is the phase mismatch. The intensity I_3 of the output beam is calculated to be [157]

$$I_3 = \frac{8d_{\text{eff}}^2\omega_3^2 I_2 I_1}{n_1 n_2 n_3 \epsilon_0 c^2} L^2 \text{sinc}^2(\frac{\Delta k L}{2}) \tag{4.1}$$

where, I_1 and I_2 are the intensities of the input beams, L is the length of the crystal, n_i $(i \in 1, 2, 3)$ are the refractive indices for the three fields, ϵ_0 is the free space electric permeability and c is the speed of light. As can be seen, the output intensity depends strongly on the phase mismatch term, $\mathbf{\Delta k}$. Apparently the output intensity is maximized when the phase mismatch is zero. This physically means the constructive interference of the three waves. However, as L gets bigger than $1/\mathbf{\Delta k}$ the output field is no longer in phase with the input fields and thus the power now can flow from frequency ω_3 to ω_1 and ω_2 waves. Thus, one can define the so-called coherence length $L_{coh} = 2/\mathbf{\Delta k}$ over which this phase matching disappears.

It is quite difficult to have zero phase-mismatch indeed. The reason is the normal dispersion, that is the increasing refractive index with increasing frequency. If we assume $\omega_1 \leqslant \omega_2 < \omega_3$, then the phase matching condition $(\mathbf{\Delta k} = 0)$ can also be written as

$$\frac{n_1\omega_1}{c} + \frac{n_2\omega_2}{c} = \frac{n_3\omega_3}{c}. \tag{4.2}$$

From this equation one sees that the following equation should be satisfied

$$n_3 - n_2 = (n_1 - n_2)\frac{\omega_1}{\omega_2}. \tag{4.3}$$

For normal dispersion, however, this is impossible to hold true as n_3 should be greater than n_2 together with n_2 being greater than n_1. This results in positive left-hand-side and negative right-hand-side of the equation. So it is impossible to have zero phase-mismatch with materials having normal dispersion, if the involved fields have the same polarization. There are

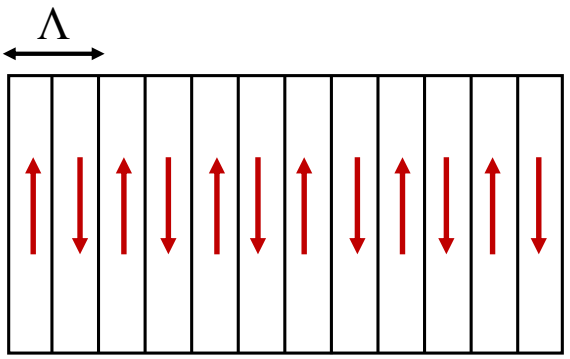

FIGURE 4.2: Schematic of periodical poling of a nonlinear crystal. Λ is the poling period.

several techniques to compensate for the phase-mismatch to have the maximum conversion efficiency throughout the whole length of the material. One of the most common techniques is called quasi-phase matching which relies on engineering of the nonlinear coefficient of the material. This is done by changing the sign of the susceptibility of the material during the engineering process with a period of Λ, which is usually around few tens of μms. This means that the material is now composed of permanent ferroelectric domains with opposite signs. The QPM condition can now be expressed as

$$\Delta k = k_1 + k_2 - k_3 + \frac{2\pi}{\Lambda}. \tag{4.4}$$

If we recall $L_{coh} = 2/\Delta k$, Λ can now be written as $2L_{coh}$. In this way the back-flow of the energy from the ω_3 beam to the other beams can be eliminated to some extent. The energy buildup in a nonlinear medium with no phase-matching, perfect phase-matching and quasi phase-matching is illustrated in Fig. 4.3. One should note that under perfect phase-matching condition and without loss, the produced power P scales with L^2.

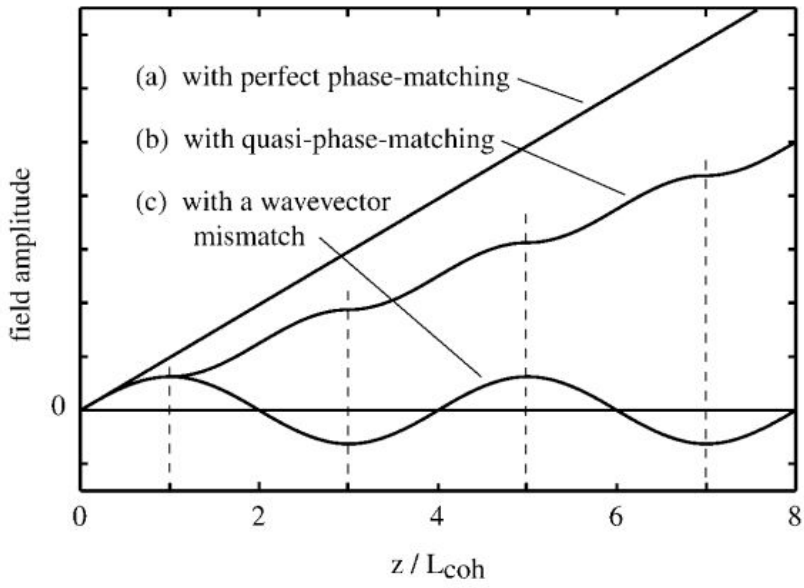

FIGURE 4.3: Amplitude of the generated field vs. position inside the nonlinear medium towards the propagation direction. In (a) the perfect phase-matching condition is assumed, (b) is under the quasi-phase matching condition and finally in (c) there is no phase matching which does not yield any increase in the produced field (figure taken from [157]).

4.1.2 Generation of 606 nm light via SFG

After the above basic theoretical introduction, I will now explain our SFG setup to produce 606 nm light.

The nonlinear crystal we use is a periodically-poled potassium titanyl phosphate (PPKTP) crystal, manufactured by AdvR and has a length of ∼2.5 cm. It has numerous waveguides buried just beneath the upper surface with each having a cross section area of around $4{\times}4$ μm^2. The chip is mounted on a one-dimensional translation stage for scanning different waveguides. A Peltier element is stacked in between the crystal mount and the translation stage to ensure high thermal stability and thus maintaining the temperature-dependent QPM condition (Fig. 4.5). The pump lasers for the SFG are from Toptica DL Pro design series. These are ECDL type lasers that have intrinsically narrow linewidths (around a hundred kHz)

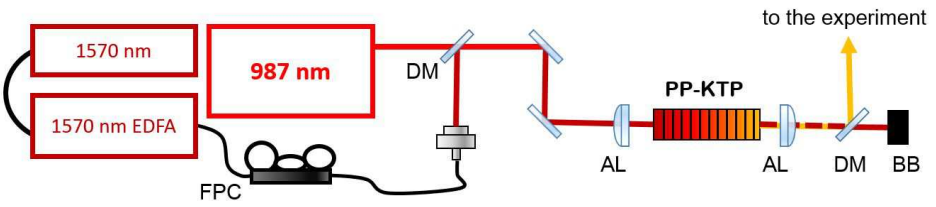

FIGURE 4.4: Experimental setup for sum-frequency generation of 606 nm light. EDFA: Erbium-doped fiber amplifier, DM: dichroic mirror, AL: aspheric lens, BB: beam block, FPC: fiber polarization controller, PPKTP: Periodically-poled potassium titanyl phosphate.

enabled by the design. In tunable ECDL-type lasers the laser diode chip is anti-reflection coated in one end and a diffraction grating is located at the output of this end of the diode chip. Optical feedback is provided by the first order diffracted beam from the grating. Wavelength tuning is achieved by rotating the diffraction grating, which is usually mounted on a piezoelectric controlled stage.

The 1570 nm laser has a maximum output power of around 50 mW. The output is adjusted to be around 1.5 mW and coupled to a single-mode fiber and then sent to a Keopsys Erbium-doped fiber amplifier (EDFA). The beam is then passed through a fiber polarization controller, then out-coupled and collimated with a Thorlabs aspheric lens (C220TME-C). The output amplitude is set to 30 dBm and the power measured before the PPKTP crystal is around 750 mW.

The 987 nm laser already contains an amplifier inside and the output is adjusted to around 400 mW. A pair of anamorphic prisms (not shown in the figure) are used to correct the elliptical shape of the beam at the output to ensure spatial overlap with the 1570 nm beam. Both beams are combined on a dichroic mirror and then focused to one of the waveguides in the PPKTP chip with another Thorlabs aspheric lens (C220TME-C). The produced 606 nm beam is collected and collimated with a Thorlabs C220TME-B aspheric lens. Each lens is mounted on a high-precision three-dimensional translation stages for better optical coupling. This ensemble

of the crystal and lenses is followed by a dichroic mirror (Semrock) which reflects 606 nm and transmits the remaining pump beams (which are then blocked) hence separating the 606 nm beam for the experiment.

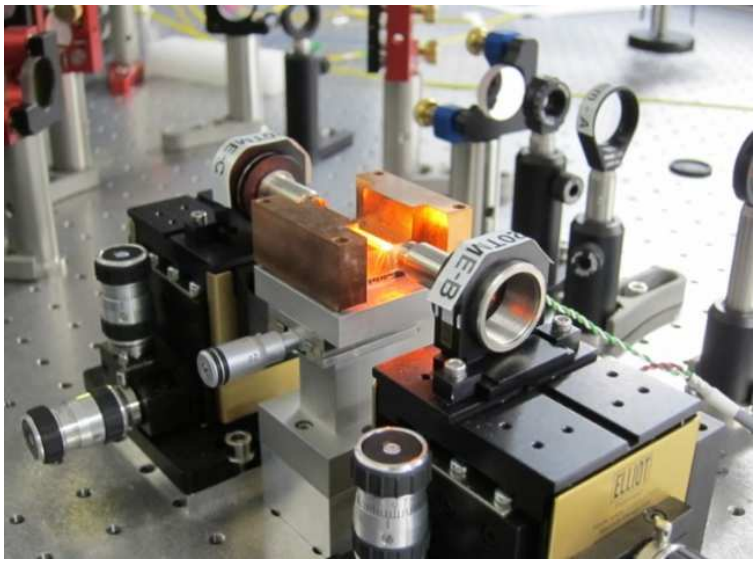

FIGURE 4.5: PPKTP crystal, together with the coupling optics.

The output power is adjusted by first beamwalking the two mirrors before the PPKTP, ensuring good optical coupling to the waveguide modes. However, as the coupling improves temperature of the crystal changes due to this enhanced coupling. After reaching a maximum value with beamwalking, temperature should also be tuned in order to readjust the QPM condition. The total output power is thus maximized in an iterative manner. Depending on the waveguide and the coupling efficiencies of the pump lasers, 606 nm beams with powers as high as 190 mW were produced. We typically had coupling efficiencies of around 30 % and a maximum conversion efficiency of $\sim$ 400%/W. Details for individual experiments will be given in related chapters.

The linewidth of the produced light is simply the sum of the input field linewidths as they have both Lorentzian shapes. Thus the expected linewidth

is around <200 kHz which was also confirmed by spectral hole burning experiments. As the linewidth is quite narrow compared to the hyperfine separations (>4.6 MHz) in Pr^{3+}:Y_2SiO_5 it allows us to perform spectroscopy and basic light storage experiments even without the need of an active frequency stabilisation. The quantum storage of polarization qubits that will be described in Chapter 5 was performed under such conditions.

4.1.3 Laser stabilisation

Although the unstabilised laser is capable of performing some basic experiments, to reach longer storage times it is necessary to have a laser with much narrower linewidth. The main reason is that as shown in Sec. 3.3 the storage time in the excited state is given by the inverse of the atomic frequency comb spacing, Δ. One can create AFCs with smaller Δ with narrower linewidth lasers. In this respect, we employed the Pound-Drever-Hall (PDH) laser technique to stabilise the frequency of our laser. It is based on locking the frequency of the laser to a mode of a medium-finesse Fabry-Perot optical cavity [158]. Another reason of stabilising the laser wavelength is to avoid long-term drifts. However, this does not constitute a major problem since the inhomogenous broadening of the transition is around 5 GHz and reasonably long experiments with unstabilised laser can still be performed in this range. It is nevertheless important that the laser does not drift between the memory preparation and the pulses storage. The details of the PDH technique is given in Appendix C. In this section, I will describe the particular setup we implemented in our lab.

The cavity is placed inside a homemade vacuum chamber with a base pressure of 1.6×10^{-7} mbar maintained by an ion pump, to reduce the effects of atmospheric fluctuation and vibrations. Some of the parameters of the cavity are as follows; $L = 15$ cm, $r = 99.86\%$ (specified by the manufacturer) and the measured FWHM is ∼1.21 MHz (∼1.36 MHz) in vacuum (air). The cavity has a free spectral range (FSR $\equiv c/2L$) of 1 GHz and a finesse (FSR/FWHM) ∼826 (∼735) in vacuum (air) (Fig. 4.6). The

experiments presented in Chapter 6 were performed while the cavity was in air, whereas the results presented in Chapter 7 were obtained with the cavity placed in the vacuum chamber.

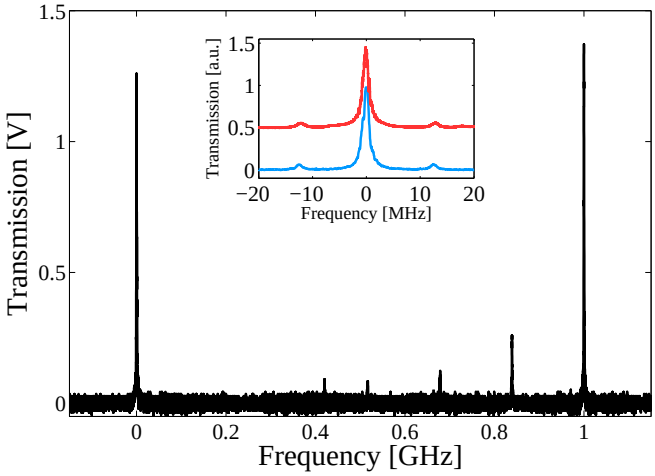

FIGURE 4.6: Frequency scan of the cavity showing the FSR= 1 GHz. Inset shows transmission signals when the cavity is outside (blue) and inside (red) the vacuum chamber. All three traces are single-shot frames. The FWHM of transmission peaks is 1.36 MHz (1.21 MHz) when the cavity is in air (vacuum). The sidepeaks at 12.5 MHz are clearly visible.

The general schematic of the locking setup is shown in Fig. 4.8. A portion of the main beam is picked up and sent through an EOM which is driven by a 12.5 MHz signal. The RF source is located inside a Toptica Digilock module, which also produces the feedback signal for the piezo controller of the diode laser. The mixer, low pass filter and the phase shifter are housed inside the lock-in module built by ICFO Electronic Workshop with the serial number TE2012.124. After passing through the EOM the beam is mode-matched to TEM_{00} mode of the cavity. The reflected signal is detected with a fast photodetector (Thorlabs PDA 450B) with 150 MHz detection bandwidth and demodulated with the 12.5 MHz signal. The resulting error signal is split into two and sent to two different feedback modules. The first part is sent to the Toptica Digilock110 module which is connected to a PC via a USB connection. One can monitor the error signal

and tune the PID parameters through a custom software. A screenshot of the user interface of the software is shown in Fig. 4.7.

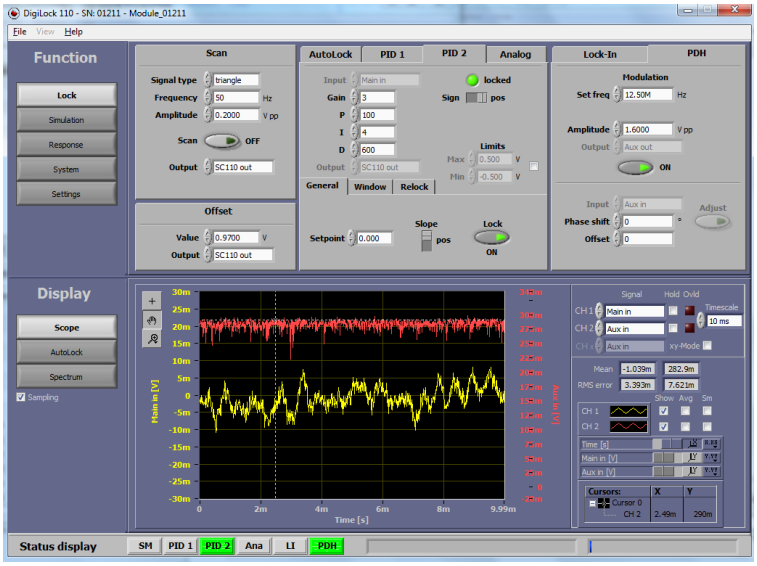

FIGURE 4.7: Screen capture of the laser frequency stabilisation software. Red trace in the panel shows the transmitted signal through the locking cavity and yellow trace shows the error signal.

The feedback is then given to the piezo of the 987 nm laser which secures long term wavelength stability. In order to correct for fast fluctuations and to reduce the linewidth of the laser however, a second, much faster electronics is needed. Toptica's FALC (Fast Analog Linewidth Control) module is designed precisely for this purpose. It has an operating bandwidth of 45 MHz that allows this kind of fast feedback. The second part of the error signal is sent to the FALC module and the feedback signal created by FALC is directly sent to the current control of the 987 nm master diode. The gain and PID parameters can be adjusted on the module itself instead of via a computer.

One way of evaluating the performance of the lock is to check the Fourier transforms of the error and/or the reflected signals with different lock parameters. A reduction in noise around the modulation frequency is a

clear indication that the feedback is working. Fig. 4.9 shows the spectrum of the detected signal at the locking detector. The signal is centered at 0 MHz for reference. We see that when we switch on the FALC module there is a reduction in the noise 675 kHz around DC.

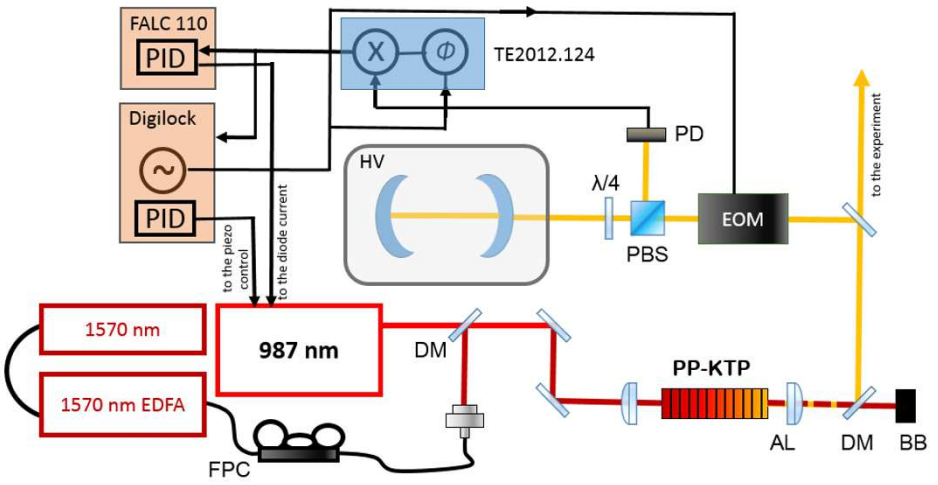

FIGURE 4.8: Schematic of the locking setup implemented in our lab. $\times$: mixer, ϕ: phase shifter, $\sim$: 12.5 MHz signal, EOM: electro-optic modulator, PD: photodiode, HV: high vacuum.

The achieved locking bandwidth is higher than the linewidth of the unstabilised laser. This would bring a reduction in the linewidth as the feedback is faster than the frequency fluctuations. The linewidth reduction is confirmed by observing spectral holes in the inhomogeneous absorption line with < 60 kHz spectral widths. A further increase in the locking bandwidth can be possible by shortening the electronic feedback loops and the optical path.

It should be noted that the feedback is only sent to the 987 nm laser whereas the error signal is derived from 606 nm light generated with SFG. Here, linewidth reduction demonstrates that the feedback signal also corrects for the fluctuations in the 1570 nm laser as well.

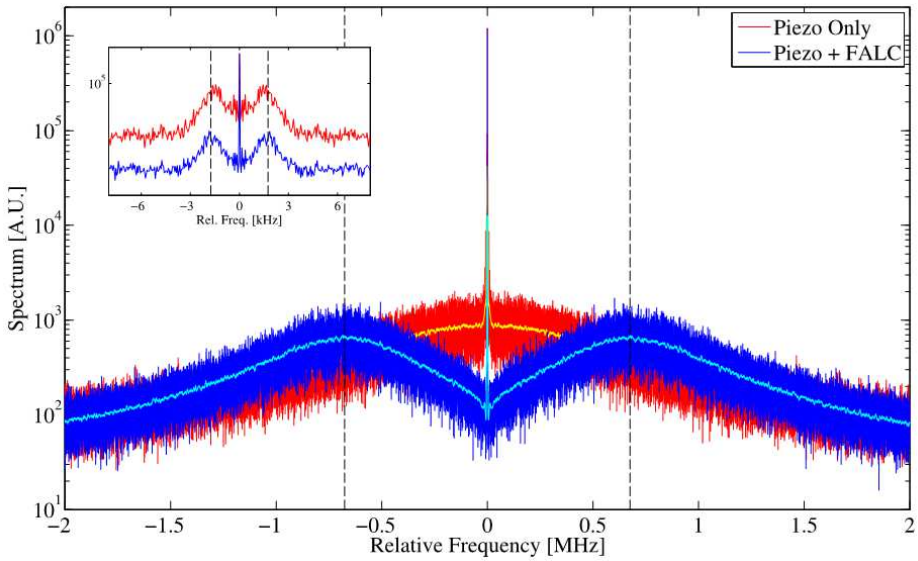

FIGURE 4.9: Spectrum of the reflected signal detected at the locking detector. The red trace shows the signal when only the piezo feedback is on. Blue shows the reduction of the noise when FALC module is turned on. Inset shows a zoom ±7 KHz around the center frequency. The dashed lines indicate the locking bandwidth of 676 kHz.

4.1.4 Toptica TA-SHG Pro laser system

We acquired a custom-built solid-state laser system from Toptica towards the end of this PhD study. As we mentioned before, dye lasers were the only type of commercially available laser for 606 nm. However, recent advances in semiconductor physics for tapered amplifiers allowed the realization of a diode laser at this wavelength.

The laser is based on the second harmonic generation (SHG) of 1212 nm beam at a nonlinear crystal located inside a bow-tie cavity to increase the conversion efficiency. The cavity length is locked to the frequency of the master laser to maintain high built-up powers within the cavity. The stabilisation is again done by the PDH method.

The 1212 nm beam is actually produced by a grating stabilised diode laser which then passes through optical isolators and fed into a tapered amplifier.

The maximum output of the master laser is 104 mW, whereas we set it to ∼90 mW. The power of the amplified 1212 nm beam is measured to be

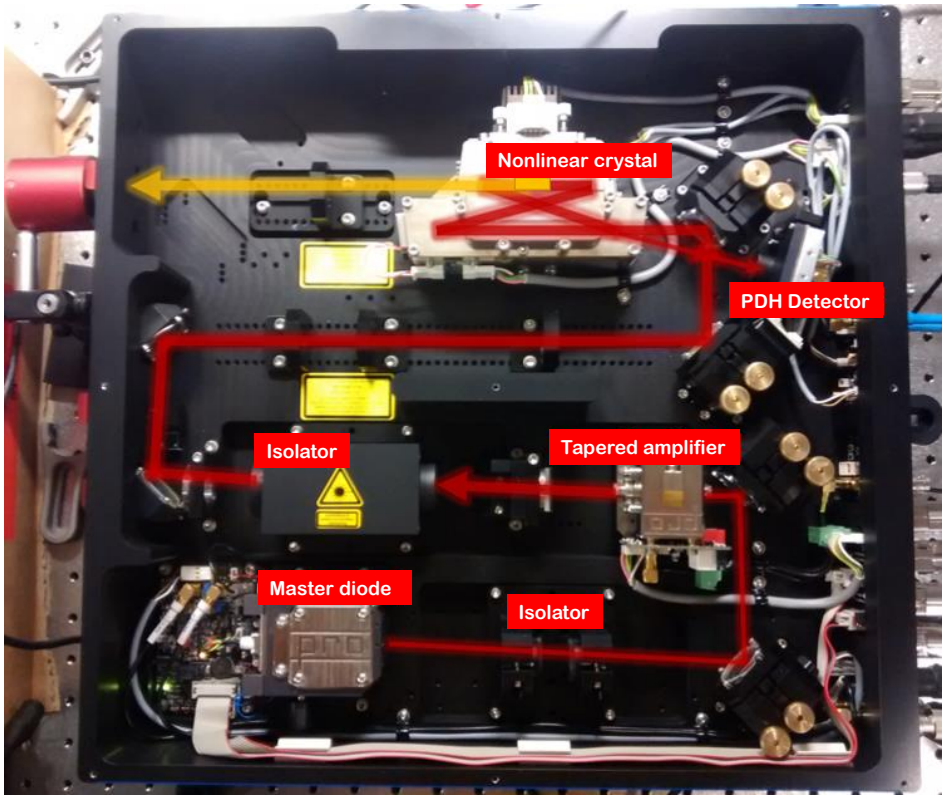

FIGURE 4.10: Top view of the Toptica TA-SHG Pro laser system.

$\sim 1.5\,\mathrm{W}$. In the end with this input power, ~ 920 $mathrmmW$ of 606 nm beam is produced through the resonance-enhanced SHG process.

The temperature of the nonlinear crystal is controlled with a precise controller and it is set to 28.1°C for proper QPM condition. The overall design allows mode hop-free frequency scans of around 20 GHz which was not possible with the previous laser setup due to the fact that it involved SFG of two separate lasers.

The stabilisation of the main beam is done by using the setup we described in the preceding section. The error signal is split into two, of which one

of them is sent to the piezo controller and the other to the current control of the 1212 nm master diode. The main advantage of this laser system is hence twofold; *i*) increased optical power. Previously the maximum 606 nm power we could ever obtain was around 190 mW, whereas now we can readily have almost a Watt of 606 nm beam, and *ii*) the linewidth of the produced 606 nm light is narrower. This is confirmed by increased two-level AFC storage efficiencies. To test this, we prepared the memory with the same optical power as with the SFG setup. We saw increases of up to 30% in the efficiency which can be attributed to the better shaping of the AFCs. Lastly, as the additional data show in Appendix B, it has superior noise performance in experiments presented in Chapter 7.

The results presented in Chapter 7 were made possible by using this system. Especially the narrower linewidth enabled us to reach ultra-low noise levels as I will describe in the relevant sections. The difference between the two systems in terms of noise performance will be discussed in Appendix B.

4.2 Cryostat

Rare-earth ions have nice coherence properties but only when they are cooled to cryogenic temperatures (<4 K). Thus a powerful and reliable cryostat is required.

We used OptistatAC-V14 liquid-free cryostat, with a cooling power of 0.5 W at 4.2 K from Oxford Instruments in all the experiments presented in this thesis. It is a closed-cycle cryostat which means that the same helium is used to cool down the sample without the need for refilling for very long times (We have not performed any helium refill during the course of this PhD study, for example). This is achieved by containing the helium in a closed circuit where it is first compressed in a water-cooled compressor (with a pressure $235-250$ psi) and then sent to a chamber by a rotary pump where it expands (with a pressure $110-120$ psi) and thus cools down.

This cryostat type is also called a pulse-tube refrigerator. A golden-coated cold finger extends from the chamber down to a second chamber where the sample holder is attached. The memory crystal is glued to the sample holder with a silver paste (Mepindus, Ag1000) to ensure the thermal contact. The expanded helium is pumped back to the compressor for the next cycle of cooling.

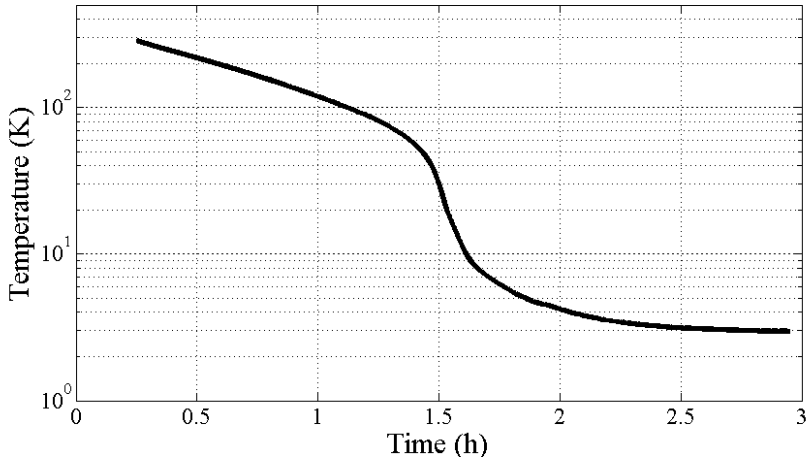

FIGURE 4.11: Measured cooling curve of the cryostat.

This cycle is repeated with a period of $\sim 0.7\,\mathrm{s}$ and the system can reach the base temperature of about $2.8\,\mathrm{K}$ in ~ 2 hours (Figure 4.11).

The main advantage of this design is that it is highly reliable (in our case it can continuously operate for few months) and does not need liquid helium. This comes with a further advantage that it reduces the operational costs. However, the main disadvantage is the vibration created by the pulses of the compressor.

In order to reduce the effects of vibrations we used two different approaches: The first is to attach the sample holder to the cold finger with a vacuum grease instead of a silver glue with which we glue the crystals to the sample holders. Being much more viscous than the silver glue, vacuum

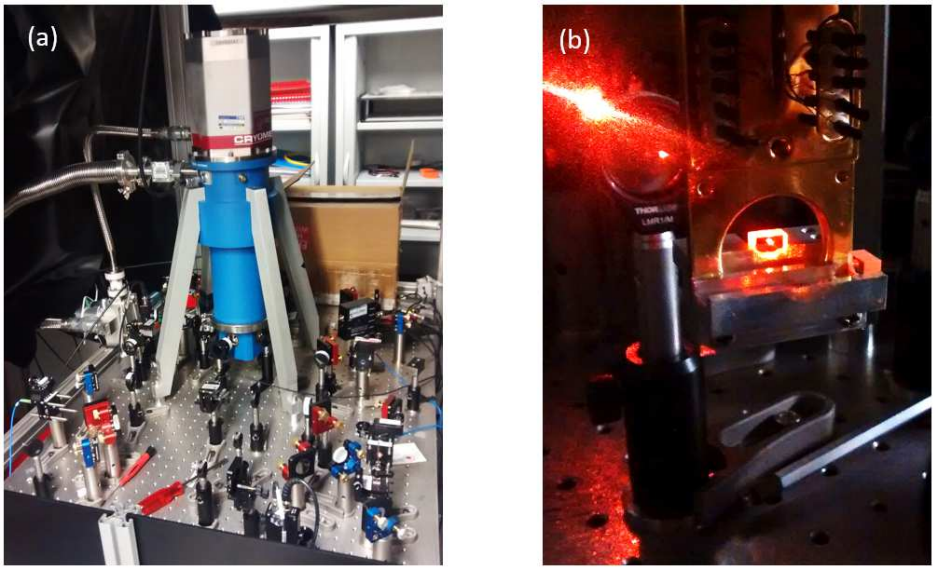

FIGURE 4.12: (a) Cryostat and the optics around it for the single-photon level spin-wave storage experiment. (b) Two crystals mounted on the sample holder attached to the cold finger in the single-photon spin-wave experiment configuration.

grease dampens the vibrations and provides a better acoustic isolation for the sample holders. We also note that clamping the crystal to the sample holder increases the effect of the vibrations on the experiments.

The second method is a bit more involved. It relies on the synchronization of the experimental cycle with the cryostat's operation cycle. This is made possible mainly due to the fact that our single experimental cycle typically lasts in much shorter times than the cryostat's cycle of 707 ms, as shown in Fig. 4.14.

A piezoelectric element is mounted on the rotary pump to convert acoustic signals to electrical ones. This series of pulses is first sent to an electronic circuit based on a preamplifier and an RC filter to filter out this high frequency noise inside the 1.4 Hz envelope. The resulting signal is then sent to an electronic module (TE2013.234) where each individual pulse is converted to a TTL signal. The fourier transform of the raw signal from

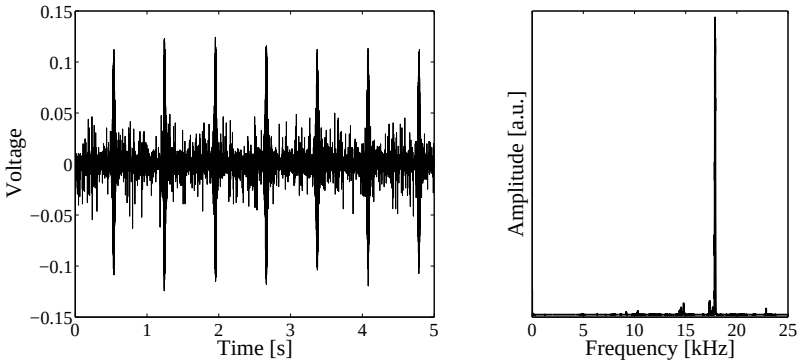

FIGURE 4.13: (a) Raw signal from the piezoelectric element, showing the cryostat's operation cycle with $\sim 0.7\,\mathrm{s}$. (b) Fourier transform of the pulses, showing the high frequency noise around 17 kHz.

the piezo shows that the sound has a frequency of 17 kHz (Fig. **??**), which is close to the upper limit of human ear around 20 kHz. The circuit is based on a preamplifier and an RC filter to filter out this high frequency noise inside the 1.4 Hz envelope.

After implementing this two-stage vibration elimination method the average memory efficiency we have became $\sim 80\,\%$ of the maximum achievable when the cryostat is off, i.e. in the absence of vibrations at all.

4.3 Detectors and the electronics

Experiments in quantum optics require a variety of detectors for different power levels and also for different wavelengths. In our lab we use several kinds of photodetectors and avalanche photodiodes (APDs).

4.3.1 Classical detectors

For the experiments involving classical light a high-gain Thorlabs PDA150B balanced detector is used. The signal is detected by one port where the

other one is physically covered. We use a transimpedance gain of 10^5 to detect the retrieved light from the memory with a bandwidth of 5 MHz. This setting allows us to detect weak classical signals ($\sim \mu$W) without distorting the shape of the pulses. However, to read the AFCs higher gain is used. We use 10^6 (10^7) with 300 kHz (100 kHz) detection bandwidth. These bandwidths would result in timing resolutions of around 3 μs and 10 μs, respectively. In this way, we can further decrease the power to read out the memory and other spectral structures we create by hole burning. This comes with the expense of the decreased bandwidth for sure, but it can be overcome by changing the sweep rate of the reading pulse. The typical read rate in the experiments is 4 kHz/μs. From the above timing resolutions for given gain settings the spectral resolution of the read would be around 12 kHz and 40 kHz, respectively. This detection resolution and the fact that the resolution of the read process is a convolution of the laser linewidth and the spectral structures put a higher bound on the observed laser linewidth.

We also made use of PDB36A-EC type of variable gain photodiodes at different stages in the experiment. We mostly use this model for reference calibration purposes. Small amounts of beams were picked up both from the memory preparation and the input beams in order to monitor the power fluctuations and to do a proper photon number calibrations.

4.3.2 Single photon counting

APDs are the central devices in most quantum optics laboratories where the experiments are performed with "discrete variables" and hence photon counting is necessary. We used several Si-APDs in our experiment with different dark count rates and detection efficiencies.

Chronologically, the first APD we used is from Laser Components COUNT series. It features a dark count rate of around 50 Hz and a measured efficiency of ∼40% at 606 nm wavelength including the fiber coupling to

FIGURE 4.14: Oscilloscope trace of a typical experimental sequence (200 ms/div). Yellow: Cryostat pulses, generated directly by the piezoeletric element. Each pulse is composed of 17 kHz oscillations. Purple: Memory preparation and control pulses. Blue: series of input pulses to be stored in the memory and green: Trigger signal created by the AWG for individual storage trial. Inset (5 μs/div): zoomed view to show individual input pulse, trigger and the pair of control pulses.

the detector chip. This model is used in the polarization qubit storage experiment and the demonstration of temporally multimode storage in spin-levels.

The other APD used in the experiments is τ-SPAD-20 from PicoQuant. This model has a much lower dark count rate of around 10 Hz and a higher detection efficiency, measured around 60% at 606 nm, again including the fiber coupling to the detector chip. This APD is used in the spin-wave qubit storage experiment.

4.3.3 Control and detection electronics

Our experiments require to have full control over the phase, frequency and amplitude of the light beams that are necessary to perform light storage experiments. Also, very complex pulse sequences for optical pumping are required in order to prepare AFCs. Thus, we need several acousto-optic modulators (AOMs) to carry out these tasks.

The AOMs used for creating the necessary pulse sequences are driven with a Signadyne analog electronic card (SD-PXE-AOU-H002). This module has 4 channels each of which has 500 M/s sampling rate and 200 MHz output. Each channel has arbitrary waveform generators (AWGs) which enables shaping pulses at will. This feature would become quite important in spin-wave qubit storage experiment as the finely shaped Gaussian control pulses induce much less noise than the square pulses. The output signals are sent to RF amplifiers (AA-Optoelectronic, AMPA-B-34) with a maximum output of 2.5 W before being fed to corresponding AOMs (AA-Optoelectronic, 200 MHz central frequency). The AOMs are installed in a double-pass configuration to eliminate beam deflection during frequency sweeps [159].

One needs a highly precise time-to-digital converter (TDC) to register the timings of individual counts from the APD. This is done by Signadyne TDC module SD-PXE-TDC-H002. It has again 4 independent channels and it features a built-in RAM to avoid memory overflows. Each channel has a timing precision of 320 ps. We typically use one channel to start a histogram with a TTL signal and given that the trigger is detected, the counter starts and registers the timing of the APD click with respect to this trigger click. A typical experimental cycle as seen on the oscilloscope is shown in Fig. 4.14.

Chapter 5

Polarization qubit storage

5.1 Introduction

Photonic quantum information can be encoded in different degrees of freedom. Time-bins and polarization states constitute robust and commonly used forms of encoding information. Polarization encoding has the advantage that the qubits can be prepared and analysed in an easy way using simple polarization optics. It is also a naturally occurring two-level system to implement photonic qubits experimentally.

There have been several experiments involving the storage of polarization states of single photon level light in different physical systems. These systems include single trapped atoms [160] and cold atoms in cavities [161]. There have also been other attempts with warm atomic ensembles, without the success of reaching the single excitation regime due to the excessive noise [162–164].

The storage of polarization qubits in a rare-earth ion doped crystal is challenging due to the fact that the host crystals are birefringent and usually have polarization-dependent absorption (Fig. 5.1). This chapter will describe our experiments where we stored and recalled photonic polarization

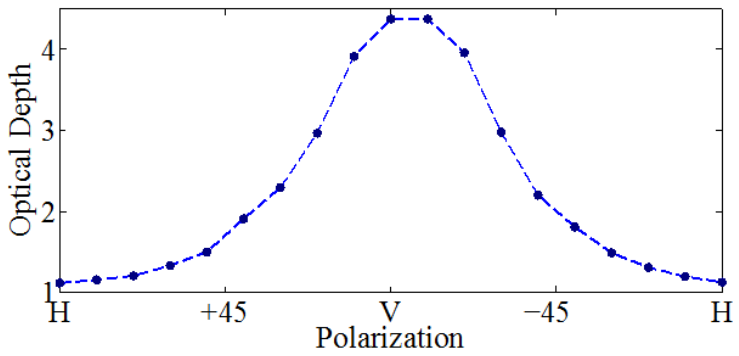

FIGURE 5.1: Measured optical depth (OD) with respect to the polarization of the absorbed light in $Pr^{3+}:Y_2SiO_5$. The maximum measured OD is around 4 and it was limited by the detection. More sensitive later measurements put this value to a minimum of 7.

qubits encoded in weak coherent states in a $Pr^{3+}:Y_2SiO_5$ crystal, using a dual-rail [46] qubit approach. The experiment made use of the Atomic Frequency Comb (AFC) scheme in the excited state, with storage times limited by the linewidth of the unstabilized 606 nm laser to around 500 ns. This is the first demonstration of photonic polarization qubit storage in a solid and it was published in the journal Physical Review Letters ([152]). This chapter also summarizes the measurement of polarization qubits and quantum state tomography.

5.2 Measurement of polarization qubits

Polarization qubits can be written in the following form

$$|\psi\rangle = \alpha|H\rangle + \beta|V\rangle. \tag{5.1}$$

with $|\alpha^2| + |\beta^2| = 1$, as we recall from Sec. 1.1.1.1. However, since the detected state is not necessarily a pure state, one needs to use the density matrix representation to properly obtain the encoded information in the qubits.

The density matrix of a system is given by,

$$\rho = \sum_{i=1} p_i |\psi_i\rangle\langle\psi_i| \tag{5.2}$$

with $\sum_{i=1} p_i = 1$, where p_i is the classical probability to find the system in state $|\psi_i\rangle$. Eq. 5.1 can be written in the column vector form as follows,

$$|0\rangle \equiv |H\rangle \equiv \begin{pmatrix} 1 \\ 0 \end{pmatrix} \text{ and } |1\rangle \equiv |H\rangle \equiv \begin{pmatrix} 0 \\ 1 \end{pmatrix}.$$

This notation makes it easier to express the qubits in density matrix form. They can now be written as follows [165]

$$\rho_H = \begin{pmatrix} 1 & 0 \\ 0 & 0 \end{pmatrix} \text{ and } \rho_V = \begin{pmatrix} 0 & 0 \\ 0 & 1 \end{pmatrix}. \tag{5.4}$$

Any arbitrary qubit can be expressed in the density matrix form with three variables as follows,

$$\rho = \begin{pmatrix} A & Be^{i\delta} \\ Be^{-i\delta} & 1-A \end{pmatrix}. \tag{5.5}$$

In 5.5, normalization requires $0 \leq A \leq 1$ and positive semi-definiteness imposes $|B| \leq \sqrt{A(1-A)}$. An alternative way of expressing density matrices makes use of the Pauli spin matrices as [165],

$$\rho = \frac{1}{2}(\mathbf{I} + \vec{\mathrm{r}} \cdot \sigma), \tag{5.6}$$

where $\sigma_1 \equiv \begin{pmatrix} 0 & 1 \\ 1 & 0 \end{pmatrix}$, $\sigma_2 \equiv \begin{pmatrix} 0 & -i \\ i & 0 \end{pmatrix}$ and $\sigma_3 \equiv \begin{pmatrix} 1 & 0 \\ 0 & -1 \end{pmatrix}$. $\mathbf{I}$ is the identity matrix. The components of the $\vec{\mathrm{r}}$ vector can be extracted from the photon counting measurements in different bases. The polarization of the light is given by the different components of the $\vec{\mathrm{r}}$ vector that correspond

to different bases, such as Horizontal - Vertical (H/V), Diagonal - Antidiagonal (D/A) and Right-Left Circular (R/L). The density matrix of the system can be reconstructed once the vector $\vec{r}$ is fully known. The polarization state of a qubit can be measured by performing projective measurements. Fig. 5.2 shows such an experimental arrangement. A set of quarter (QWP) and half waveplates (HWP) together with a polarizing beam splitter (PBS) are used to measure the input state in any polarization basis. The technique to perform this task is called Quantum state tomography and described in the following section.

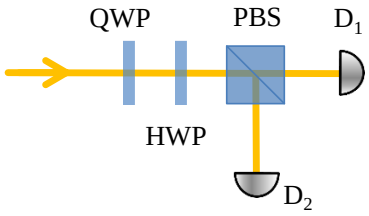

FIGURE 5.2: A sketch of a simple polarization analyser implemented with a set of waveplates and a polarizing beam splitter.

5.3 Quantum state tomography

Quantum state tomography provides a way to accurately construct the density matrix of a quantum mechanical system with a series of measurements performed in different bases. However, measurements on a single copy of the system is insufficient as the measurement results are probabilistic. Hence it is necessary to perform measurements to project the states of identical copies of the system to different states to obtain the full quantum mechanical information. Large number of measurements should be performed to have a better statistics on the probed system. We adopt the approach developed by the group of Paul Kwiat in Ref. [166] and later elaborated in [165].

In our photon counting experiments the relevant components of the $\vec{r}$ vector are found as $r_H = 2N_H/(N_H+N_V)-1$, $r_D = 2N_D/(N_D+N_A)-1$ and $r_R = 2N_R/(N_R+N_L)-1$, where N_i is the number of photons counted in the ith basis. The density matrix of the system then can be constructed according to Eq. 5.6. However, most of the time, mainly due to experimental imperfections and fluctuations the above method fails to yield a physical density matrix, i.e. the eigenvalues of the matrix might result in negative values. Quantum state tomography based on maximum likelihood estimation provides a way to overcome this issue.

5.3.1 Maximum likelihood estimation

A physical density matrix must satisfy the following properties *i*) normalization, *ii)* positive semi-definiteness and *iii)* hermiticity. As mentioned above any direct attempt to reconstruct the density matrix might fail to satisfy some of these, if not all, properties.

The maximum likelihood estimation technique is used to produce a matrix that is most likely to represent the measured density matrix. It starts with a matrix that already satisfies the three conditions for physicality. Any matrix that can be written as $\mathbf{T}^\dagger\mathbf{T}$ is hermitian and positive semi-definite [166]. As for the last condition, namely the normalization, the matrix is normalized with its trace that finally yields, $\rho_p = \mathbf{T}^\dagger\mathbf{T}/\mathrm{Tr}(\mathbf{T}^\dagger\mathbf{T})$. Here, the matrix $\mathbf{T}$ can be parametrized with the variables t_i,

$$\mathbf{T}(t_1,t_2,t_3,t_4) \equiv \begin{pmatrix} t_1 & 0 \\ t_3+it_4 & t_2 \end{pmatrix}. \tag{5.7}$$

A likelihood function then can be defined with the parameters that form the matrix $\mathbf{T}$.

$$L = \sum_{i=0}^{3} \frac{[N\langle\psi_i|\rho_p|\psi_i\rangle - N_i]^2}{2N\langle\psi_i|\rho_p|\psi_i\rangle}. \tag{5.8}$$

Finally, maximization of this function produces the density matrix that most likely represents the experimentally measured density matrix.

5.4 Experimental details

This section will outline the experimental arrangement we used for the storage of polarization qubits in $Pr^{3+}:Y_2SiO_5$.

5.4.1 Experimental setup

The laser system based on sum frequency generation (SFG) used in this experiment was described in detail in Sec. 1.1.2. In this experiment, around 90 mW of 606 nm light is produced from 370 mW of 987 nm and 750 mW of 1570 nm pump beams. Both beams are coupled to the PPKTP crystal with efficiencies of around 30% which yields SFG efficiency of $\sim$350 $\%/W^{-1}$.

The main beam is then split into two for the memory preparation and the preparation for the weak pulses to be stored. Each beam is passed through acousto-optic modulators (AOMs) (AA-Optoelectronic, 200MHz central frequency) in double-pass configuration for amplitude and frequency modulation to create the necessary pulse sequences to prepare the AFC and also to create the short, weak pulses to be stored.

The rf signals to drive the AOMs are generated by an arbitrary waveform generator from Signadyne (500 Msample/s, 200 MHz, 1 GB internal memory). After the AOMs, the beams are carried with polarization maintaining fibers to another optical table where the cryostat and the detection setup is located (see Fig. 5.3).

In the heart of the experiment lies a 3mm-long $Pr^{3+}:Y_2SiO_5$ crystal with a doping level of 0.05% placed in an Oxford V14 cryo-free cooler at a temperature of around 3K. In order to circumvent the problem of unequal

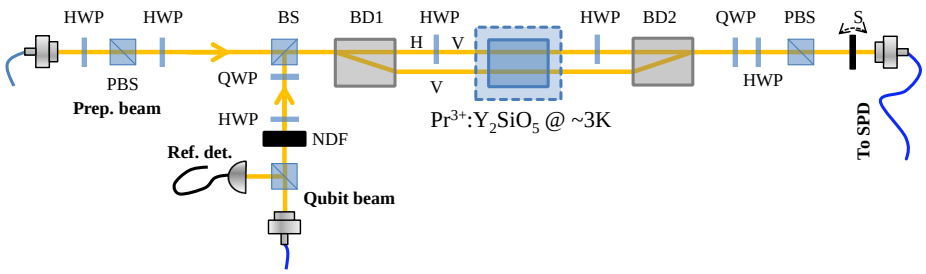

FIGURE 5.3: Experimental setup for polarization qubit storage. BD1, BD2: beam displacers, QWP: quarter-wave plate, HWP: half-wave plate, BS: beam splitter, PBS: polarizing beam splitter, NDF: neutral density filter, S: mechanical shutter and SPD: single photon detector.

absorption of different polarizations, we employed the *dual-rail* qubit approach. In this configuration, the beam is split into its two polarization components in different spatial modes. To do this, a calcite beam displacer, (Thorlabs BD27) denoted as BD1 Fig. 5.4 is placed in front of the cryostat window to separate the two polarization components (H/V) of the incoming light into two parallel spatial modes with a separation of 2.7mm. The polarization of the preparation beam is set to 45° to ensure equal powers in two spatial modes. The main technique employed in this work to compensate for the unequal absorption of different polarization components is to rotate the polarization of the horizontally polarized beam (Fig.5.3) after BD1 by 90° with a half-wave plate (HWP) so that both spatial modes would enter to the storage crystal with the same (V) polarization to match the D2 axis of the Pr^{3+} :Y_2SiO_5 crystal (Sec. 2.4). This method ensures the equal absorption of both spatial modes and enables the storage of polarization qubits.

The input beam is attenuated to the single-photon level with a stack of neutral density filters (NDFs) after its amplitude and frequency is modulated by the AOM to create the input pulses. Some portion of the input beam is picked up before the NDF and sent to a reference detector (Thorlabs PDB36A-EC) for photon number calibration. The qubits are prepared

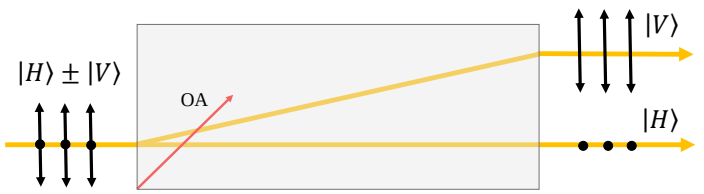

FIGURE 5.4: Simple schematic of a beam displacer. An orthogonally polarized beam is split into two parallel spatial modes with polarizations H and V. OA is the optical axis of the crystal.

with a set of successive half- and quarter-wave plates. The correct wave-plate settings are determined with the help of a polarimeter. The settings used in the experiments are shown in Fig. 5.1 for several input polarization states.

Input state	HWP	QWP
$\|H\rangle$	10.5°	219.5°
$\|D\rangle$	30°	261°
$\|R\rangle$	112.5°	279°

TABLE 5.1: HWP and QWP settings for the qubit preparation for horizontal (H), diagonal (D) and right-hand circular (R) polarizations.

After the NDF, the input beam is combined with the preparation beam on a beam splitter (BS) and passed through BD1 where its two polarization components are split as discussed in the previous paragraph. The polarization of the beam is rotated back with another HWP and the two beams are combined at a second beam displacer (BD2). The the optical paths between BD1 and BD2 forms a polarization interferometer with high passive stability [107, 167].

After the interferometer, the transmitted and retrieved light from the memory enters the polarization analysis stage, composed of a QWP, a HWP

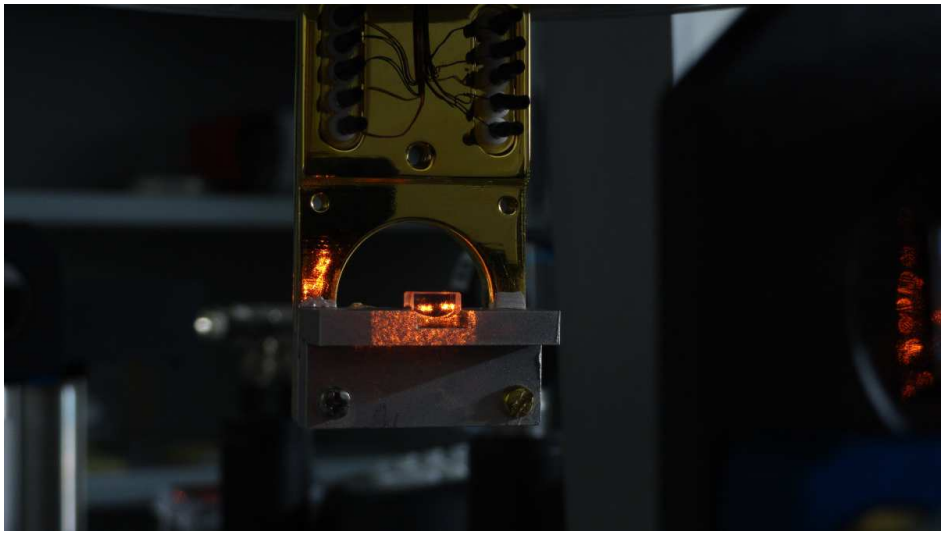

FIGURE 5.5: The storage crystal mounted on the sample holder with the two polarization components passing through. Holder of the BD1 is visible on the rightmost side of the picture.

and a polarization beam splitter (PBS), allowing us to measure the polarization state in any basis for tomographic reconstruction of the density matrix. The beam is then coupled in a multimode fiber with a coupling efficiency of ∼90% and then connected to a silicon avalanche photodiode single photon detector (SPD, model Count-100C, Laser Components) with a detection efficiency $\eta_D = 50\,\%$ and a dark count rate of $\leq 50\,\mathrm{Hz}$. Electronic signals (or 'clicks') produced by the SPD are sent to a time stamping card (PXIe card from Signadyne) in order to construct the the arrival time histogram. A TTL signal produced by the AWG is used as the start signal of the histogram. An acoustic mechanical shutter is placed in front of the fiber coupler before the SPD in order to temporally separate the leakage from the strong preparation beam and avoid any saturation and damage to the SPD.

The mean photon number μ is determined by sending input pulses with the frequency of the laser being 60 GHz off resonance, and measuring the detection probability per pulse p_{det} and backpropagating before BD1 to

take into account the losses in the optical path. Transmission from BD1 to the SPD (η_t) is measured to be 40%.

A significant degree of spatial overlap between the input and the preparation beams through the storage crystal is crucial. This is done by removing the NDFs from the input beam path and setting an equal power in both beams. Rough alignment is performed by the use of irises whereas the fine tuning of the overlap is performed by directing the overlapped beams to a classical detector and maximizing the visibility of the resulting interference by beamwalking. Beam diameters are around 600 μm and 260 μm for the preparation and the input beams, respectively.

5.4.2 Memory preparation and the pulse sequence

In this experiment, the AFC is prepared on the $5/2_g - 5/2_e$ transition as it has the strongest transition dipole moment among all the possible transitions between ground and excited state manifolds. However, this choice prohibited us to form a Λ-type system as the dipole moments of the other two transitions connecting the common excited state $5/2_g$ to the other ground levels are very small (see Table 2.1). The fact that our laser had not been stabilized at the time of this experiment encouraged us to make this choice as the transfer of the population to the ground state would require a more stable laser, mainly to create narrow peaks for longer storage time in the excited state. This also limits this particular experiment for storage only in the excited state.

The memory preparation is based on the technique introduced in Ref. [78] by Stefan Kröll's group at Lund. It starts with sweeping the frequency of the preparation beam by 12 MHz, resulting in a wide transmission window (it will be called a *spectral pit* from now on) within the inhomogeneously broadened absorption line (green trace in Fig. 5.6). The laser frequency is then shifted by -27 MHz with respect to the center of the spectral pit and a 2 ms−long single-frequency burn pulse is applied to create a single

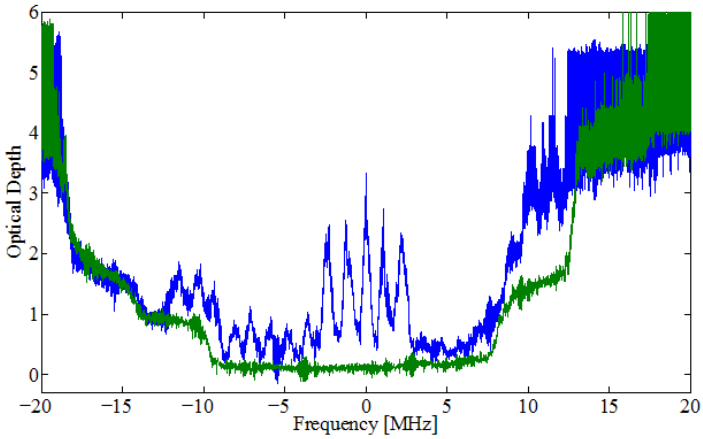

FIGURE 5.6: Empty transmission window prepared by scanning the laser frequency by 12 MHz (green) and an AFC, with $\Delta = 2$ MHz prepared on the $5/2_g - 5/2_e$ transition (blue). The memory crystal has a length of 3 mm.

spectral hole as depicted in Fig. 2.7. As a consequence, an anti-hole that corresponds to the $5/2_g - 5/2_e$ transition is then created (or "burned back") within the transparency window. Afterwards, the frequency of the laser is shifted in steps of 2 MHz and in each step the above hole-burning process is repeated. The eventual result is the AFC shown as the blue trace in Fig. 5.6 and has the following properties; background OD $d_0 = 0.64$, average peak OD, $d = 2.77 \pm 0.21$, average comb tooth width $\gamma = 640 \pm 65$kHz. With these parameters the expected 2 level AFC echo efficiency is found to be $\eta_E = 8 \pm 1\%$, using Eq. 3.20 and assuming Gaussian AFC peaks.

The total preparation sequence takes around 1 s and in the next 2 s a series of weak input pulses are sent to the memory with a repetition rate of 50 kHz.

5.5 Results

In all our experiment s the comb spacing in the AFC is set to 2, MHz which results in a predetermined storage time, $t_S = 1/\Delta$, of 500 ns.

We first verified that we can store and retrieve a complete set of qubits distributed over the Poincaré Sphere in our storage device. To this end we stored and recalled the following input states: $|H\rangle$,$|V\rangle$, $|D\rangle = \frac{1}{\sqrt{2}}(|H\rangle + |V\rangle)$, $|A\rangle = \frac{1}{\sqrt{2}}(|H\rangle - |V\rangle)$, $|R\rangle = \frac{1}{\sqrt{2}}(|H\rangle + i|V\rangle)$ and $|L\rangle = \frac{1}{\sqrt{2}}(|H\rangle - i|V\rangle)$. The red trace in Fig. 5.7 shows the storage of $|V\rangle$ encoded in weak coherent

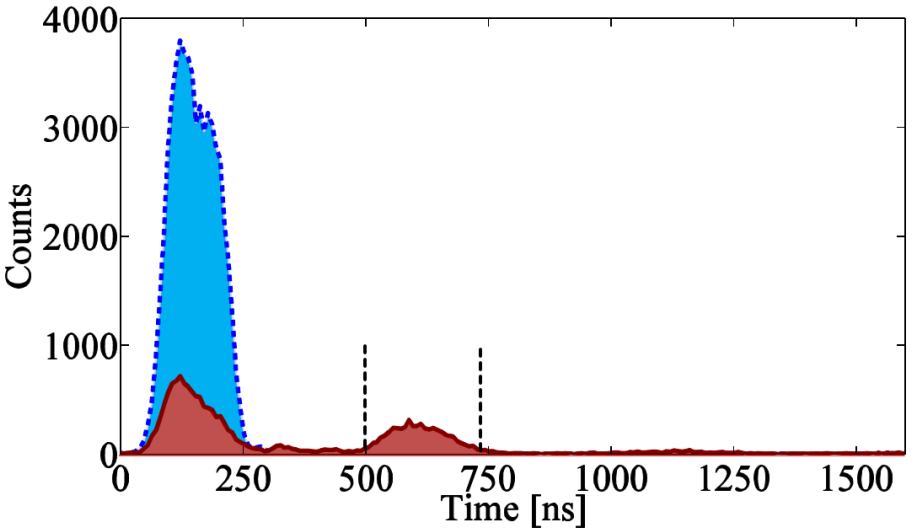

FIGURE 5.7: Storage and retrieval of $|V\rangle$ qubits with $\mu = 0.4$ (red) and the detected pulses when there is no AFC prepared (blue).

pulses with $\mu = 0.4$ and 140 ns duration (FWHM) whereas the blue shows when the same input pulses are sent through an empty spectral pit without an AFC prepared. In total 5×10^5 pulses are sent to the storage crystal. All the 6 tested polarization states are stored and retrieved with similar efficiencies, with the average being $\eta_M = (10.6 \pm 2.3)\,\%$. The measured efficiency is compatible with η_E within the errors.

Next, we need to make sure that the coherence is preserved between the $|H\rangle$ and $|V\rangle$ components of the qubits during the storage process. In order to test whether the coherence is preserved or not, we record the number of counts in the retrieved pulses when rotating the detection bases using the HWP for different input polarization states. Fig. 5.8a shows the interference fringes obtained for the input states $|V\rangle$ (blue) and $|D\rangle$ (red)

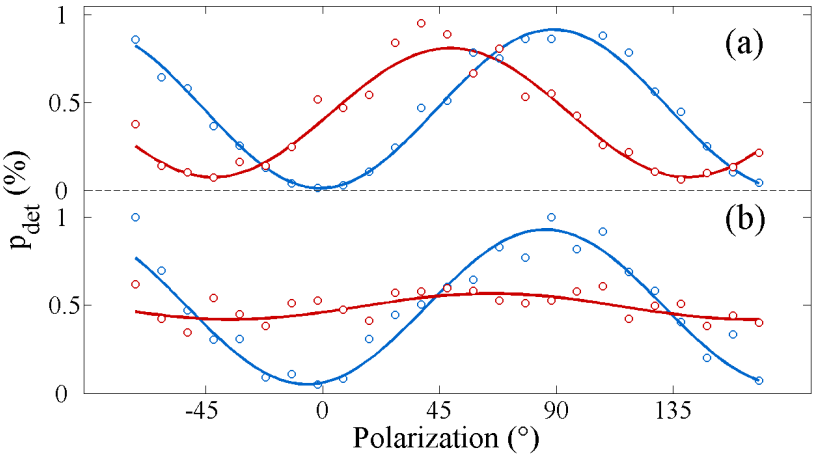

FIGURE 5.8: Measured detection probabilities as a function the HWP angle for different scenarios. (a) $|V\rangle$ (blue) and $|D\rangle$ input qubits. (b) $|R\rangle$ input qubit in the presence (blue) and absence (red) of the QWP in front of the HWP in the qubit preparation part. Dots are data points and the lines are the fitted curves.

raw visibilities of (97 ± 0.5) % and (83 ± 2) %, respectively. For the case of the circularly polarized qubits we should not observe any dependence on the HWP angle when the QWP is removed. This is because the polarization of the input beam is still in circular and thus the analyser PBS will simply divide the incoming power in two. Interference should be restored when the QWP is placed before the HWP as the circular input polarization now becomes a linear polarization. This result is shown in Fig. 5.8b. We observe a reduced visibility of (15 ± 3) % in the absence of the QWP. After inserting the QWP, the interference is restored with a visibility of (89 ± 2) %. We attribute the residual visibility in the absence of the QWP mainly to non-perfect preparation of the $|R\rangle$ state. It should be noted that the visibilities for the input states that can be decomposed into two components ($|R\rangle$ and $|D\rangle$) are slightly lower. This is mainly due to the small phase fluctuations in the polarization interferometer created by the vibrations from the cryostat. Similar visibilities (99%, 98.5% and 89% for $|H\rangle$, $|V\rangle$ and $|D\rangle$, respectively)were observed with bright pulses with the

laser frequency being off-resonant with the atomic transition. This suggests that the observed non-unit visibilities are mainly due to the phase fluctuations in the interferometer and the phase is well preserved during the storage and retrieval of different polarization components in different spatial modes.

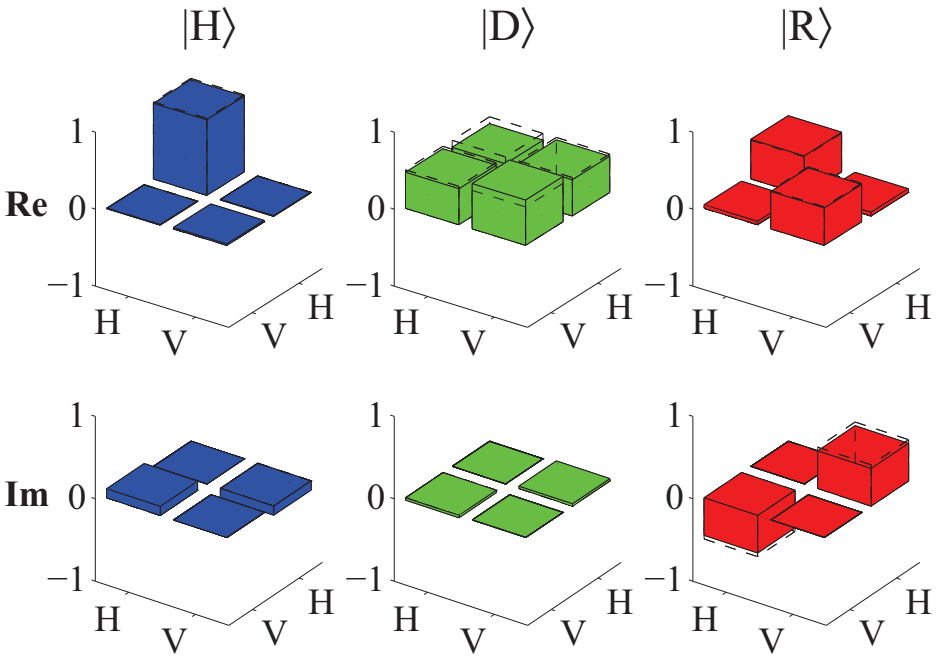

FIGURE 5.9: Reconstructed density matrices of the retrieved qubits with $\mu = 0.4$. No background is subtracted. Dashed bars show the matrix components of the ideal states.

We use quantum state tomography as explained in Sec. 5.3 to reconstruct the density matrix of the retrieved qubits to calculate the fidelity of the storage process. Fig. 5.9 shows the reconstructed density matrices ρ_{out}, of the complete set of qubits for $|H\rangle$, $|D\rangle$ and $|R\rangle$ states with $\mu = 0.4$. The conditional fidelity (Sec. 1.4.2) of the output state with respect to the target state $F^c_{|\psi\rangle} = \langle\psi|\rho_{out}|\psi\rangle$ can then be estimated from the reconstructed matrices. The values we obtain are listed in 5.2. We find a mean fidelity of $F^c_{mean} = (96 \pm 2)\,\%$. We should note that this value is a lower bound for the conditional fidelity, since it is calculated with respect to target states

and also takes into account imperfections in the preparation of the qubits.

As a last analysis, we determine the average fidelity F^c_{mean} (Eq. 1.11) as

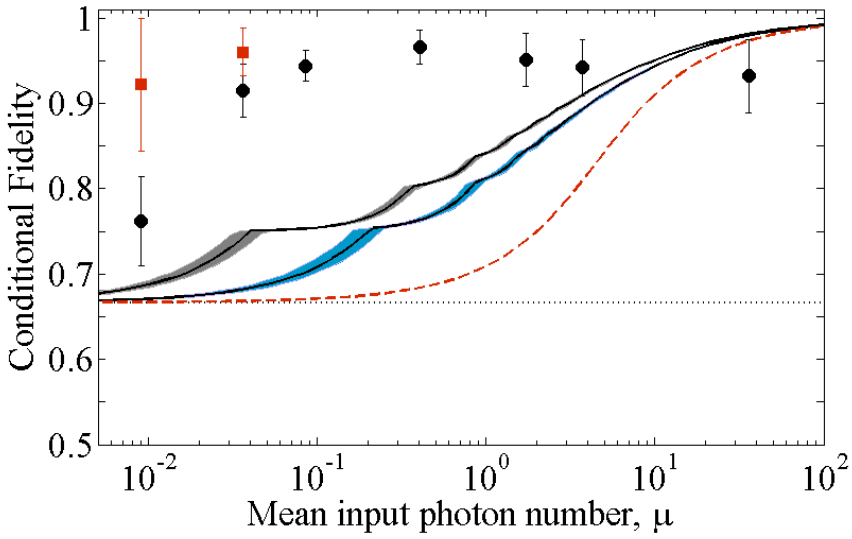

FIGURE 5.10: Conditional fidelity of the retrieved qubits with respect to the mean input photon number, μ. The fidelity is measured by quantum state tomography and averaged over the fidelities of the fidelities of the states $|V\rangle$, $|D\rangle$ and $|R\rangle$. Black dots are the experimental data, red squares are the fidelities when the dark count of the detector is subtracted. The black horizontal dashed line is the fidelity of the single-photon Fock state (2/3).Red dashed line corresponds to the Eq. 5.9, takes into account the Poissonian statistics of the input field. Blue and black shaded regions correspond to the cases where the finite storage and retrieval efficiency is considered as well.

a function of μ and compare it with the best obtainable fidelity using a measure and prepare strategy to assess the quantum nature of the storage. It is known that for a state containing N qubits, the best classical strategy can lead to a maximum fidelity of $F_c = (N+1)/(N+2)$ [59]. However, if the qubit is encoded in weak coherent states, which is also the case in the present experiment, one has to take into account the Poission distribution of the photon number that constitutes each qubit [160]. The maximum

achievable classical fidelity, in this case, becomes,

$$F_{class}(\mu) = \sum_{N\geq 1} \frac{N+1}{N+2} \times \frac{P(\mu, N)}{1 - P(\mu, 0)}, \tag{5.9}$$

where $P(\mu, N) = e^{-\mu}\mu^N/N!$. This is valid for the case of a memory with unit efficiency. However, if $\eta_M < 1$, a classical memory could use a more elaborate strategy to exploit the finite efficiency so that it could gain more information about the input state as first demonstrated in [160]. For instance, it could produce an output only if the number of photons per pulse is high and hence it can better estimate the fidelity of the input quantum state.

However, in the case of Ref. [160] the memory is a single trapped atom in an optical cavity, thus the maximum number of photons can be stored in the memory at a given time is limited to 1. We adopted the approach developed in Ref. [160] and modified for an ensemble-based memory where almost any μ can be stored. Details of the calculation of the classical fidelity for the case of a non-unit efficiency memory is given in Appendix A.

The different curves for different scenarios discussed above are shown in Fig. 5.10 as a function of the mean input photon number, μ. The black dots show the experimental data from which we see that for the most of the photon numbers tested, the measured F^c_{mean} values are significantly higher than the maximum achievable classical fidelity. This proves that our crystal operates as a quantum storage device for polarization qubits. F^c_{mean} decreases for $\mu < 0.1$. This is mainly due to the dark count of the SPD, as high fidelities can be recovered by subtraction of this background (red squares). This also demonstrate the noise-free character of the two-level AFC storage protocol. On the other hand, we also observe that when μ becomes large ($\mu \geq 3.5$ in our case), the F^c_{mean} is not sufficient to be in the quantum regime anymore. This analysis shows that very high fidelities are required to assess the quantum character of the storage when

using coherent states with $\mu >> 1$. To our knowledge, it is the first time that ensemble based storage has been characterized using this criteria.

Input State	Fidelity	Input State	Fidelity
$\|H\rangle$	0.982 ± 0.003	$\|V\rangle$	0.983 ± 0.002
$\|D\rangle$	0.968 ± 0.005	$\|A\rangle$	0.938 ± 0.009
$\|R\rangle$	0.954 ± 0.007	$\|L\rangle$	0.926 ± 0.01

TABLE 5.2: Raw conditional fidelities for 6 different polarization input states. For this measurement, η_M varied between 8 % and 10 %. The errors have been obtained using Monte Carlo simulation taking into account the statistical uncertainty of photon counts and a technical error reflecting slow drifts in our systems, and estimated from the residuals from the fit of Fig.5.8 and similar curves.

5.6 Discussion and conclusion

The storage time in our experiment is limited by the minimal achievable width of the AFC peaks (<600 kHz), which is in turn limited by the linewidth of our unstabilized laser at the time of the experiment. As we will show in the next sections, the width of the AFC peaks were later reduced to around 40 kHz with a frequency-stabilized laser system. The fundamental limit for the AFC peak widths is however given by the homogeneous linewidth of the optical transition ($2-3$ kHz). The creation of AFC peaks with widths limited by the natural homogeneous broadening would allow storage times of around tens of microseconds in the excited state. Finally, once combined with the temporal multimode storage capability of the AFC technique [81], this would enable the storage of multiple polarization qubits in the time domain. Moreover, transfer of the optical excitation to long-lived spin states could increase the storage time to the order of seconds [109] and even to minutes [110].

In conclusion, we have demonstrated the storage and retrieval of photonic polarization qubits encoded in weak coherent pulses in the single photon

level. The average conditional fidelity of the storage and the retrieval is $> 95\,\%$, significantly higher than the classical benchmark for input photon numbers $\mu < 3.5$ even when we consider the finite device efficiency and the Poissionion photon statistics. Our results show that solid state quantum light matter interfaces are compatible with photonic polarization qubits, which are widely used in quantum information science.

Our results extend the storage capabilities of REID based memories to polarization encoding. The number of modes that can be stored in the memory can be doubled by combining the time and polarization degrees of freedom. In a related direction, recently the storage of hyperentangled states of light (photons entangled both in polarization and energy-time degrees of freedom) have been stored in a REID solid [168]. Additionally, the fact that the two polarization components have been stored in different spatial modes in the same crystal shows that REID based memories can also serve as spatially multimode quantum memories.

Chapter 6

Spin state storage of temporally multimode light

6.1 Introduction

Most AFC experiments including the one presented in the previous chapter used AFC storage in the excited state. In that case, the memory actually acts as a pre-programmed delay line for light. The delay time that can be achieved with AFC is limited by the minimum obtainable comb spacing Δ, which depends on the optical homogeneous broadening (given that the laser linewidth is narrower). For $Pr^{3+}:Y_2SiO_5$, this would correspond to a maximum storage time on the order of $50-100\,\mu$s in the excited state, in the best case. Moreover for practical applications requiring synchronization, on-demand readout of the stored light is required. This can be achieved by transferring the excitation to long-lived spin states [81] (*spin-wave storage*) which offers storage times in the order of seconds [109] and even minutes [110].

To reach spin-wave storage, several technical improvements had to be implemented. The main improvement was the stabilization of the laser frequency (see Sec. 4.1.3). This greatly enhances the performance of the

memory, as much narrower AFC peaks can now be created. The end result is being able to reach much longer storage times in the excited state which is required, so that a pair of strong control pulses can be fit within this time period. Also, the elimination of the slow frequency fluctuations renders the experiment much more stable. In this case one can increase the number of storage trials for each AFC prepared. The results presented in this chapter were made possible after the stabilization of the laser.

As mentioned in Sec. 3.3.3, proof of principle experiments of the full AFC scheme have been demonstrated using $Pr^{3+}:Y_2SiO_5$ with a total efficiency of $0.5-1\,\%$ (transfer efficiency of $30-45\,\%$), with a multimode capacity of 2 temporal modes [134]. More recently, it has been implemented in a $Eu^{3+}:Y_2SiO_5$ crystal [147] with a lower efficiency due to the low oscillator strength of the Eu^{3+} transition compared to Pr^{3+}. In this work, we extend those results in multiple ways. Firstly, by performing time-bin interference experiments we show that the coherence is preserved during the transfer to and storage in the spin-states. The second main improvement is the storage of up to 5 temporal modes in the spin-states. All the experiments presented in chapter were performed with classical pulses although these results can be extended to single-photon regime after sophisticated filtering techniques are implemented. This will be presented next chapter.

6.2 Experimental description

6.2.1 Optical setup

The experimental setup is shown in Fig. 6.1. The main difference in this experiment is that the laser frequency is now stabilized by the Pound-Drevel-Hall method. The details of the laser system and frequency stabilization is given in Secs. **??** and 4.1.3. The laser source is based on the sum frequency generation of 987 nm and 1570 nm light. The two pump beams are combined in a PPKTP waveguide to generate the light at 606 nm.

With input powers of 429 mW and 1138 mW and coupling efficiencies into the waveguide of about 38 % and 27 % for the 987 nm and 1570 nm lasers, respectively, we achieve an output power of 190 mW at 606 nm, corresponding to a conversion efficiency of 385 %/W.

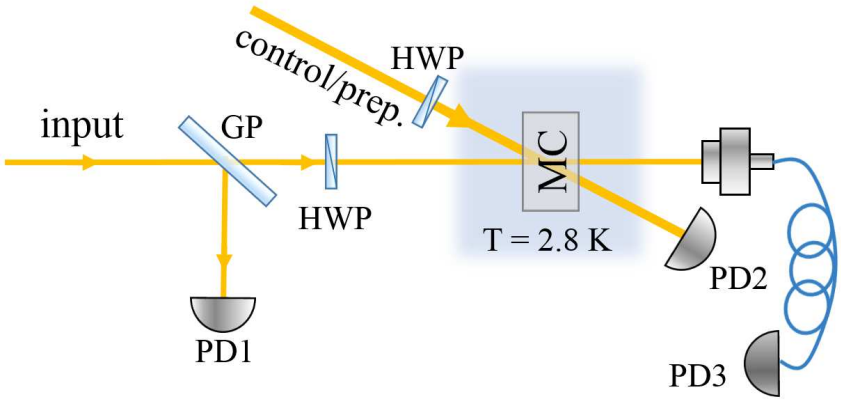

FIGURE 6.1: Schematic of the experimental setup. HWP: half-wave plate, GP: glass plate and PD: photodiode.

Acousto-optic modulators (AOM) are used in double pass configuration [159] to create the necessary pulse sequences for the experiments. The RF pulses used to drive the AOMs are generated by a Signadyne arbitrary waveform generator.

We use two different optical paths (spatial modes) to interact with the crystal, namely strong and weak modes that are separated by a narrow angle. This spatial separation of the two modes has a two-fold advantage. The first is that it prevents, or at least reduces the coupling of the preparation and control pulses to the weak mode due to scattering. The second is that it helps separating the strong free induction (FID) that is created by the strong control pulses. Filtering the FID is crucial as it is emitted coherently in the same spatial mode with the control pulses. FID might occur if the transparency window is imperfectly prepared, i.e., if some residual population remains in the ground state that is supposed to be empty for the spin-state storage (see subsection 6.2.2). Pulses in each mode are prepared in the above-mentioned double-pass AOMs after

which the beams are directed to a separate optical table where the cryostat (Oxford V14) operating at a temperature of 2.8 K is located.

The Pr^{3+} :Y_2SiO_5 crystal used in the experiment is 3 mm-long with 0.05 % doping concentration. The absorption coefficient α is measured to be $23\,cm^{-1}$ for the optical transition at 605.977 nm. The inhomogeneous linewidth is measured to be 5 GHz. Half-wave plates (HWPs) are placed in front of the cryostat to ensure the polarization is aligned parallel to the optical D_2 axis of the crystal, in order to maximize the absorption [91]. A glass plate is placed in the input mode after the fiber outcoupler to pick up some portion of the light to be used as a reference signal. A lens with a focal length $f = 100$ mm is used to focus both beams onto the crystal with beam sizes of around 95 μm. The maximum powers in the strong and weak beams measured before the cryostat are 7 mW and 1.5 mW, respectively. An additional $f = 100$ mm lens is placed after the crystal for spatial mode matching. The echo mode is steered to a detector via a single mode fiber with 50 % coupling efficiency. The linewidth of the laser at the time of this experiments is estimated by spectral hole burning experiments to be around 100 kHz over $\sim$ ms time scales. The linewidth is estimated by measuring the width of spectral hole as the one shown in Fig. 2.7.

6.2.2 Memory preparation and the experimental sequence

The full AFC scheme realized in the present work is depicted in Fig. 6.2. We chose to work with the $\Lambda-$ scheme used in Ref. [134]. The input pulse (blue arrow) is resonant with the comb on the $1/2_g - 3/2_e$ transition, while the coherent transfer of the optical excitation to and from the ground state (green arrows) is tuned to the $3/2_g - 3/2_e$ transition. The echo is emitted on the $1/2_g - 3/2_e$ transition (red arrow). The $5/2_g$ ground level is used as the auxiliary state where all the unwanted atomic population is pumped to (See Table 2.1).

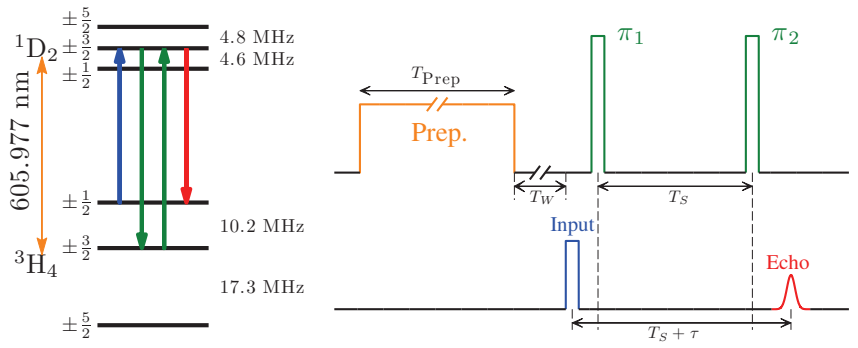

FIGURE 6.2: Level scheme and pulse sequence for the spin-wave AFC memory. The comb is prepared in a time $T_{\mathrm{Prep}} = 200\,\mathrm{ms}$. A waiting time of $T_W = 1\,\mathrm{ms}$ is used between the end of the preparation and the start of the 3LE sequence. T_s is the time between the control pulses π_1 and π_2, and τ is the AFC delay time. The total storage time is $T_S + \tau$.

The preparation of the memory follows the approach described in Ref. [78] and Section 5.4.2. A transparency window (spectral pit) is first created inside the inhomogeneous absorption profile by sweeping the laser frequency by 12 MHz, thus pumping all the ions which are resonant with this light to a non-resonant ground state. The sweep is repeated 100 times resulting in a spectral pit with a width (FWHM) of around 18 MHz [78, 169]. The burn-back method [78] is used to tailor the AFC. It consists of the pumping of ions from the $5/2_g$ auxiliary state, some of which will decay in the ground states previously emptied, thus giving rise to isolated narrow peaks (anti-holes as described in Sec. 2.5) in the spectral pit. The AFC is created by sending several burn-back pulses at frequencies differing by Δ. The finesse of the comb, and thus the efficiency of the AFC echo, can be optimized with a proper choice of duration, power and number of the burn-back pulses. Fig. 6.3 shows an example of an AFC prepared on the $1/2_g - 3/2_e$ transition.

We should note that different classes of ions will be resonant with the burn-back pulses as the hyperfine level splittings ($\sim$MHz) are smaller than the inhomogeneous width ($\sim$GHz) [169]. In the frequency window of interest

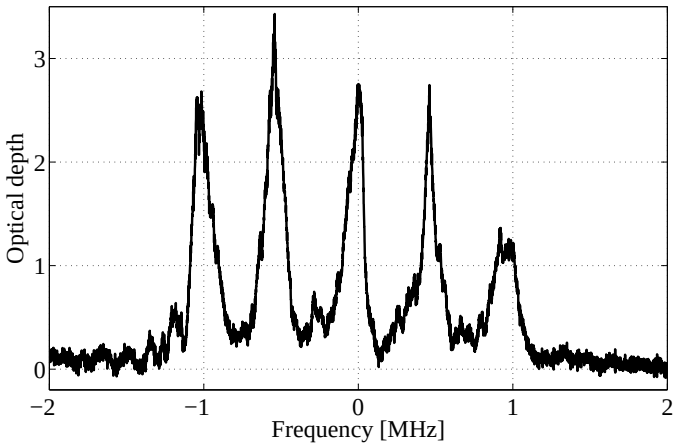

FIGURE 6.3: An example of an AFC used in this experiment. Δ is set to 500 kHz that results in the excited state storage time, $\tau = 2\,\mu$s.

for the comb, transitions associated to two classes of ions are indeed present ($1/2_g - 3/2_e$ of one class and $1/2_g - 1/2_e$ transition of the other class).

The burn-back procedure also populates the $3/2_g$ ground state, while an efficient full AFC scheme requires it to be empty. This state should be emptied before the transfer of the excitation to eliminate any noise that would be created by the strong control pulses. A "clean" sweep is performed in the spectral region of the $3/2_g - 3/2_e$ transition whose spectral bandwidth matches that of the comb. This clean sweep offers also the ulterior advantage of emptying the ground states of the unwanted classes (Appendix D).

In the experiments presented here, the total AFC preparation time, T_{Prep} from Fig. 6.2, is 200 ms, of which 50 ms are used to create the AFC. This includes $5 \times 100\,\mu$s burn-back pulses for the 5 comb peaks repeated every 500 ns for 100 times and a 2 MHz clean sweep centered at the transfer pulse frequency repeated 1000 times.

Fig. 6.3 shows an example of comb with a periodicity $\Delta = 500$kHz. It is worth noting that the read method and the limited detection response time

lead to underestimation of the comb optical density and finesse. Different detection methods are used for the results presented in the next sections. For the results presented in subsections 6.3.1-6.3.4 a photodiode (Thorlabs PDB150) is used and a memory is prepared for each pulse that is stored. For subsection 6.3.5 a single photon counter (Laser Components, model Count) is used and for each memory prepared, 500 pulse trains are used.

6.3 Results

6.3.1 AFC Storage

Figure 6.4 shows an example of a two-level AFC echo (dashed curve) for an excited state storage time of $\tau = 2\,\mu$s. Using input pulses of 840 ns duration, an AFC efficiency of $\eta_{\mathrm{AFC}} = 15.6 \pm 0.5\,\%$ is observed. The efficiency is measured by taking the area of the echo in the blue trace and comparing this to the area of the input pulse (black trace) when sent through an empty spectral pit in the absence of an AFC. When measuring the input pulse area, its polarization is rotated to be perpendicular to the optical D_2 axis, ensuring weak interaction with any residual ions in the pit. We compare the area of the transmitted part of the input pulse to that of the echo to better estimate the AFC parameters [129]. The probability of a photon to transmit through a medium with a prepared AFC is given by $\mathrm{T} = e^{-(d_0+d/F)}$, whereas the ratio of the stored photons to the transmitted ones are given as, $\mathrm{R} = 1/[(d/F)^2 e^{-7/F^2}]$ [129]. By using these two equations and assuming a tooth width of $\gamma = 125\,(167)$ kHz, then $F = 4\,(3)$ and the inferred optical depths would become $d = 4.12\,(3.66)$ and $d_0 = 0.45\,(0.26)$, which are both larger than what is detected with a direct read-out of the AFC as shown in Fig. 6.3.

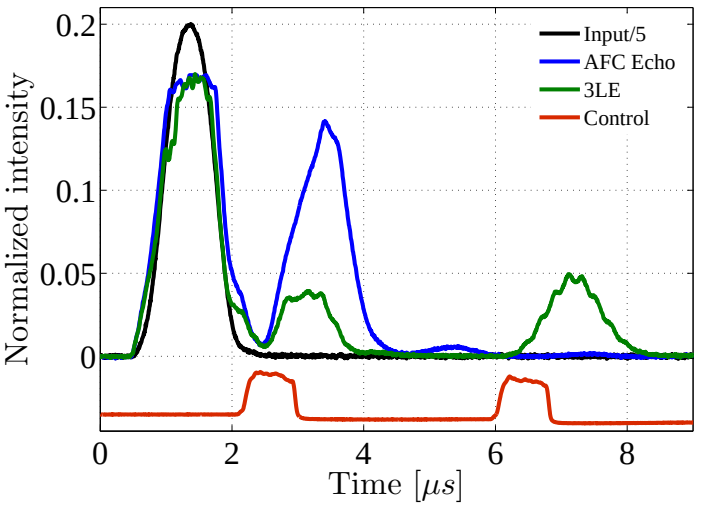

FIGURE 6.4: The full AFC memory scheme. The blue curve shows the two-level echo from an AFC programmed to give a delay of $2\,\mu$s ($\Delta = 500\,$kHz) (Fig. 6.3). The green solid curve shows the effect of the transfer pulses. The AFC echo is reduced and the 3LE is observed. The black curve shows a reference of the input pulse, with full width at half max duration of 840 ns. For clarity, this curve is divided by 5. The red trace indicates the temporal location of the 800 ns rephasing pulses separated by $T_S = 4\,\mu$s.

6.3.2 Spin-Wave Storage

Figure 6.4 shows an example of the full AFC scheme of spin-wave storage (green curve). A strong single frequency control pulse (red curve) is used to transfer the excited state coherence to and from the $3/2_g$ ground state. The effect of the first transfer pulse is clearly seen by the significant reduction of the AFC echo. A second transfer pulse is applied after a time $T_S = 4\,\mu$s and a 3LE is clearly seen above the noise level (red curve). The observed 3LE is the direct result of the application of both control pulses, as confirmed by the fact that it vanishes by removing either the first or the second control pulse or the input pulse itself. The oscillation seen on the 3LE and the reduced 2LE in the red curve has a frequency of 10.2 MHz, and it is mostly

due to the beating between the noise created by the control pulses and the corresponding echoes.

Figure 6.5 shows the 3LE efficiency, both calculated from the amplitude and the area (inset) of the echo, as a function of T_S. Due to the inhomogeneous broadening of the spin states, the efficiency of the echo decays as a function of T_S. This inhomogeneity is known to be Gaussian with the following form [147]:

$$\eta(T_S)_{3\mathrm{LE}} = \eta(0)_{3\mathrm{LE}} \times \exp\left[\frac{-(\gamma_{\mathrm{IS}} T_S)^2}{2\log(2)/\pi^2}\right], \tag{6.1}$$

where γ_{IS} is the spin inhomogeneous broadening and $\eta(0)_{3\mathrm{LE}}$ is the 3LE efficiency at zero delay. Fitting the data with this equation and extrapolating to $T_S = 0$, where the spin inhomogeneity has no effect, the 3LE efficiency, $\eta(0)_{3\mathrm{LE}}$, for the area (amplitude) is found to be $5.6 \pm 0.1\,\%$ ($5.0 \pm 0.1\,\%$). The corresponding inhomogeneity then becomes $\gamma_{\mathrm{IS}} = 25.6 \pm 0.2\,\mathrm{kHz}$ ($25.7 \pm 0.4\,\mathrm{kHz}$) in agreement with previous experiments [134, 170]. Comparing the AFC efficiency with this 3LE efficiency, the transfer efficiency is calculated to be $57\,\% - 60\,\%$ using Eq. 3.23.

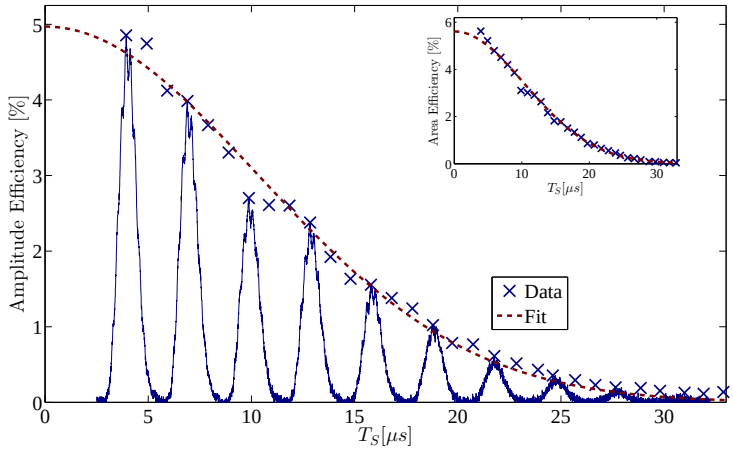

FIGURE 6.5: 3LE efficiency vs. T_S. All the conditions are the same as in Fig. 6.4. Inset shows the efficiency calculated by taking the area of the echo. All data are the average of 10 acquisitions.

6.3.3 Transfer Characterization

In this section I will present the experiments where we characterize the transfer efficiency η_T as a function of the power in the control pulse and thus the Rabi frequency, $\Omega_R = \mu_{ge}E/\hbar$. Here E is the electric field amplitude and μ_{ge} is the electric dipole moment of the transition. The experimental conditions for this measurement are identical to those outlined in Fig. 6.4. A time T_S of 4 μs is chosen as a time fast compared to the spin inhomogeneous dephasing time so as not to limit the storage efficiency.

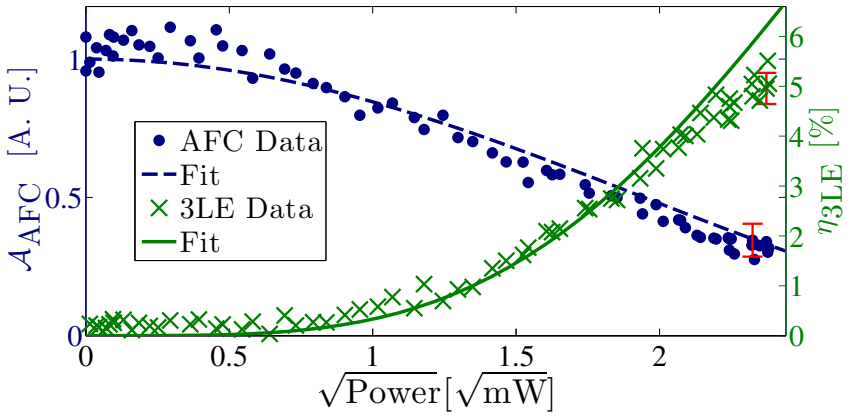

FIGURE 6.6: Two level AFC echo area $\mathcal{A}_{\mathrm{AFC}}$ (dots) and three level efficiency $\eta_{3\mathrm{LE}}$ (crosses) as a function of the square root of power of the control pulses. The dashed and solid lines represent a fit to the data as described in the text. Each data point is an average of 10 trials. Error bars indicate the maximum standard error in the mean measured for each data set.

Figure 6.6 shows the 3LE efficiency and the area of the two-level AFC echo $\mathcal{A}_{\mathrm{AFC}}$ as a function of the square root of power of the control pulses. Intuitively, as the power is increased the AFC echo decreases and the 3LE increases. This behaviour can be modelled simply with a two-level atomic system being driven resonantly [84, 171], resulting in the following

equations,

$$\mathcal{A}_{\mathrm{AFC}}(\bar{\Omega}_R t) = \mathcal{A}_{\mathrm{IN}} \frac{\eta_{\mathrm{AFC}}}{2} \left[1 + \cos(\bar{\Omega}_R t)\right], \tag{6.2}$$

$$\eta_{\mathrm{3LE}}(\bar{\Omega}_R t) = \frac{\eta_{\mathrm{AFC}}}{4} \left[1 - \cos(\bar{\Omega}_R t)\right]^2, \tag{6.3}$$

where $\mathcal{A}_{\mathrm{IN}}$ is the area of the input pulse and we introduce $\bar{\Omega}_R$ as the effective Rabi frequency. This takes into account that the input and control pulses have inhomogeneous spectral and spatial profiles and also the imperfect spatial mode overlap between the two modes. The data in Fig. 6.6 are fitted simultaneously with the above equations and show good agreement. The effective Rabi frequency is found to be $\bar{\Omega}_R = 2\pi \times 340\,\mathrm{kHz}$ for a power of 5.7 mW at the crystal.

As a comparison, we measure the Rabi frequency with coherent hole burning techniques [172] using only the control mode. The technique relies on preparing a single-class absorptive feature in an empty pit and then coherently burning spectral holes at the center of this absorptive feature with varying pulse durations. By comparing the resulting optical depths after each hole burning, one can then estimate the Rabi frequency of the particular transition (in this case $3/2_{\mathrm{g}} - 3/2_{\mathrm{e}}$). Fig. 6.7 shows different spectral holes burnt with 100 ns, 1.15 μs and 2 μs pulses with 5.7 mW power, respectively.

An oscillatory behaviour is seen when the ions are driven coherently towards the excited state with a Rabi frequency $\Omega_R = \mu_{ge} E/\hbar$. Most, if not all the ions in the pulse bandwidth can be transferred to the excited state if the pulse area reaches the value of π. This behaviour is seen in Fig. 6.8. A Rabi frequency, Ω_R of $2\pi \times 420\,\mathrm{kHz}$ is found from the oscillation period, whereas it is estimated to be around $2\pi \times 430\,\mathrm{kHz}$ from the calculations, taking into account the pulse power and the electric dipole moment of the $3/2_{\mathrm{g}} - 3/2_{\mathrm{e}}$ transition ($2.32 \times 10^{-32}\,\mathrm{Cm}$). By using experimentally measurable parameters, the Rabi frequency can be written as,

$$\Omega_R = \frac{\mu_{ge}}{h} \sqrt{\frac{2I}{\mathrm{c}\,\epsilon_0\,\mathrm{n}}}. \tag{6.4}$$

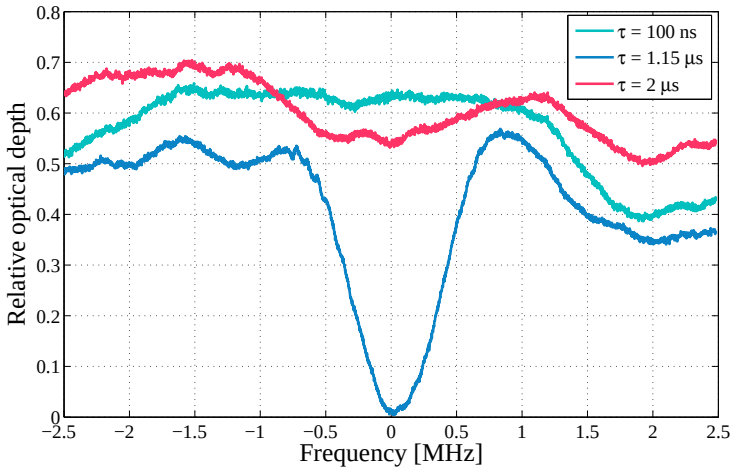

FIGURE 6.7: Coherent hole burning spectra with different pulse durations.

In Eq. 6.4, n is the refractive index of the crystal and $I = 2P/w$ is the intensity of the laser for a Gaussian beam with a waist of w. This Rabi frequency is independent of the spatial mode overlap since we use only one spatial mode and is thus higher than the effective Rabi frequency that is inferred from the spin-state storage experiments. It should be noted that there is no exact analytical form to mathematically express the oscillation shown in Fig. 6.8 due to fact that it strongly depends on the experimental conditions, mainly on the beam shape [172, 173].

6.3.4 Coherent storage

Keeping in mind that our grand goal is to implement an on-demand quantum memory for single photon level light fields, it is crucial that the phase between the two modes that are needed to encode a qubit be preserved during storage and retrieval. For quantum communication schemes, in addition to the polarization states, information can also be encoded in the amplitude and phase of time-bin qubits, as they are known to be robust

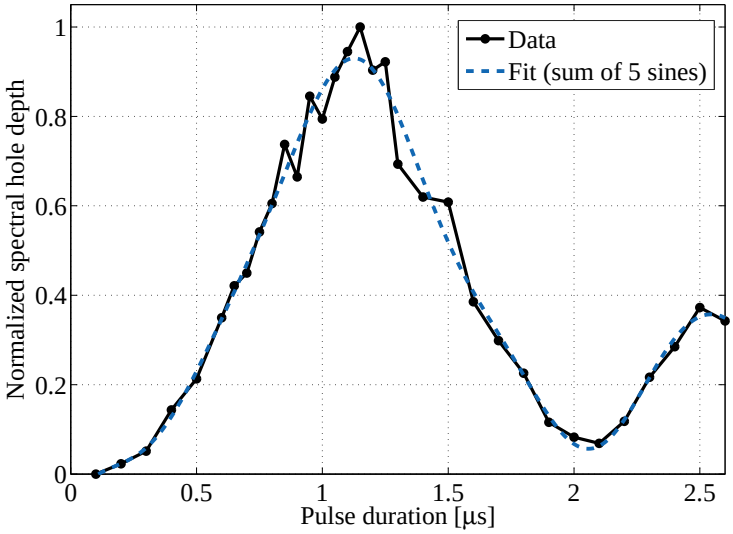

FIGURE 6.8: Coherent driving of the atomic population in arbitrary units with respect to different Rabi pulse durations. Blue dashed line is a fit aimed as a guide for an eye.

against decoherence in optical fibers [3]. In this experiment, we confirm for the first time the coherent storage of time-bin information using the spin-wave AFC memory. The schematic for the coherence measurements is shown in Fig. 6.9. We send a pair of input pulses (the early pulse I_e and the late pulse I_l) separated by t_s and with a relative phase difference ϕ. The pair of pulses are stored and analyzed directly in the memory by employing the inherent temporal multimode capability of the AFC scheme. This requires the implementation of partial readouts [174], achieved by sending two readout pulses (C_2 and C_3) separated also by t_s. The resulting output of the memory is three temporal modes, where the central mode shows coherent interference between the echo of the late pulse from the first read out (E_{l1}) and the echo of the early pulse created by the second read out (E_{e2}). The experimental traces showing the constructive and destructive interference are shown in Fig. 6.10.

The resulting interference fringe as the relative phase $\Delta\phi$ is varied is shown

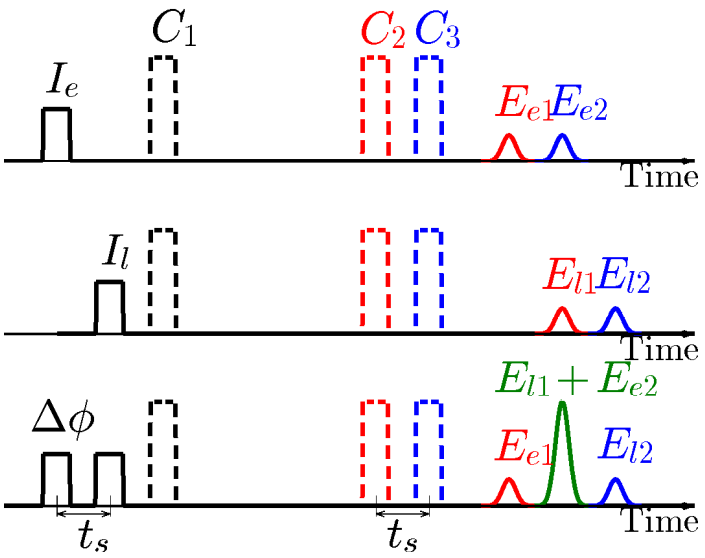

FIGURE 6.9: The experimental sequence for the coherence measurements. The first control pulse, C_1 is applied to transfer the input field to the spin-states whereas two control pulses with temporal separation t_s are employed (C_2 and C_3) to partially read-out the memory which results in two spatially separated echoes (E_{e1} and E_{e2} for the early input I_e, for instance). If another input pulse, I_l, is sent at a time t_s after the first one, the first echo of I_e and the second echo of I_l would overlap in time, resulting in three temporal modes. Finally, depending on the phase relations between the input or the control pulses, an interference is observed in this overlapping time-bin (green curve in the lowest panel).

in Fig. 6.11. Here, the relevant parameters are as follows; $\tau = 5\,\mu$s, $T_S = 12\,\mu$s, $t_s = 1\,\mu$s and pulse durations of 700 ns. For each relative phase, a total of 10 acquisitions are made for statistics and averaging. The detection window width (indicated with dashed lines in Fig. 6.10) is chosen to be 500 ns. The data show that the coherence is indeed preserved during the storage and retrieval process. The weighted sinusoidal fit yields a visibility of $84.0 \pm 5.7\,\%$.

The coherent nature of the storage is further investigated by measuring the fringe visibility as a function of T_S. The observed visibility remains at a constant value of $\bar{V} = 81.7 \pm 1.4\,\%$ as T_S is increased, i.e. it is independent of the storage efficiency as shown in Fig. 6.12. This behaviour is typical

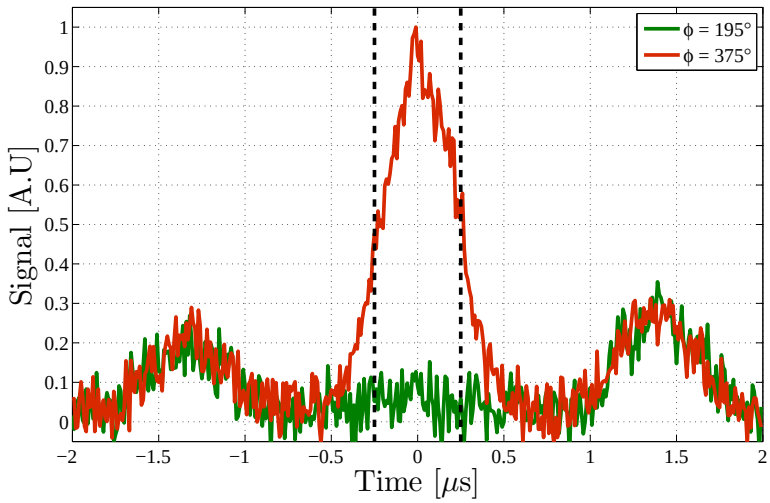

FIGURE 6.10: Experimental trace of coherent interference of the echoes by double read-out method as outlined in Fig. 6.9. Different curves represent two extreme cases of constructive (red) and destructive (green) interference.The vertical dashed lines indicate the time window where the echo area is calculated for the interference ($t_v = 500\,\text{ns}$). Normalized echo area for the two curves are indicated with the corresponding colors in Fig. 6.11.

for ensemble based optical memories [175], where the recall efficiency is decreased but the conditional fidelity (Sec.1.4.2) remains constant. However, this is true as long as the retrieved signal is much greater than the background noise, which is a challenging condition to achieve with single photon level input fields. The other way of probing the coherence is to vary the phase between the read-out pulses while keeping the relative phase between the input pulses constant. This experiment also yields an interference fringe with V = 84 %.

The observed visibilities would result in storage conditional fidelities exceeding 90 % ($F_C = (1 + V)/2$) which, if this could be demonstrated with single photon fields, would be sufficient for applications in quantum communication. The maximal possible visibility should be however 100%. Note that, besides the possible decoherence in the crystal, the visibility is directly affected by the phase noise between the two input time-bins

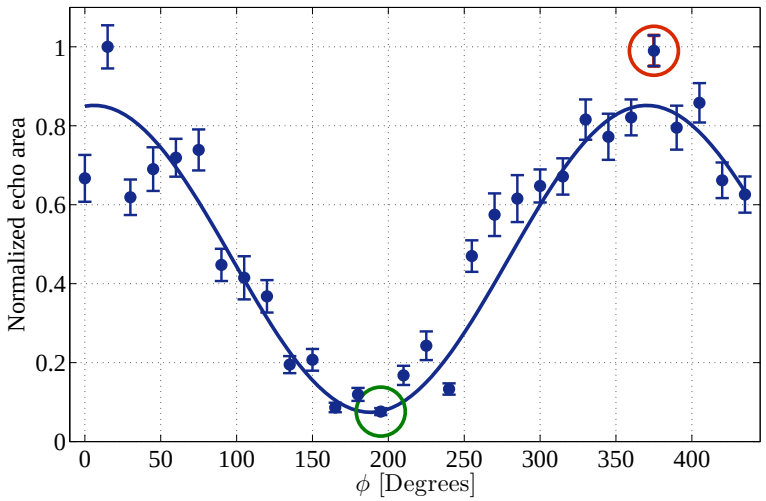

FIGURE 6.11: Echo area in the interference window vs. phase difference between the two input pulses. Each data point is an average over 10 trials with the error bar representing one standard deviation of the mean. The line is the weighted sinusoidal fit to the data. The visibility of the observed fringe is $84.0 \pm 5.7\,\%$.

and the one between the two control pulses. To check the origin of the noise, we performed an interference measurement using two pulse photon echoes (Sec. 3.1.3). In this way any possible decoherence occurring in the spin-states are eliminated as the two-pulse echo technique only involves the excited state. Fig. 6.13(a) shows the experimental schematic to check this.

Two write pulses, separated in time by t are read by two consecutive read-out pulses separated by $t/2$. Three distinct temporal modes appear as the output of which the middle one is the overlap of the two echoes originated by different write pulses. An interference, similar to that in Fig. 6.11 is observed as the phase between the two write pulses, $\Delta\alpha$ is varied. The resulting interference fringe with a visibility 81.8% is shown in Fig. 6.13(b). Each data point is an average of 10 acquisitions and the error bars are calculated from the standard deviation. The large error bars are caused by the fact that this particular experiment was not synchronized with the

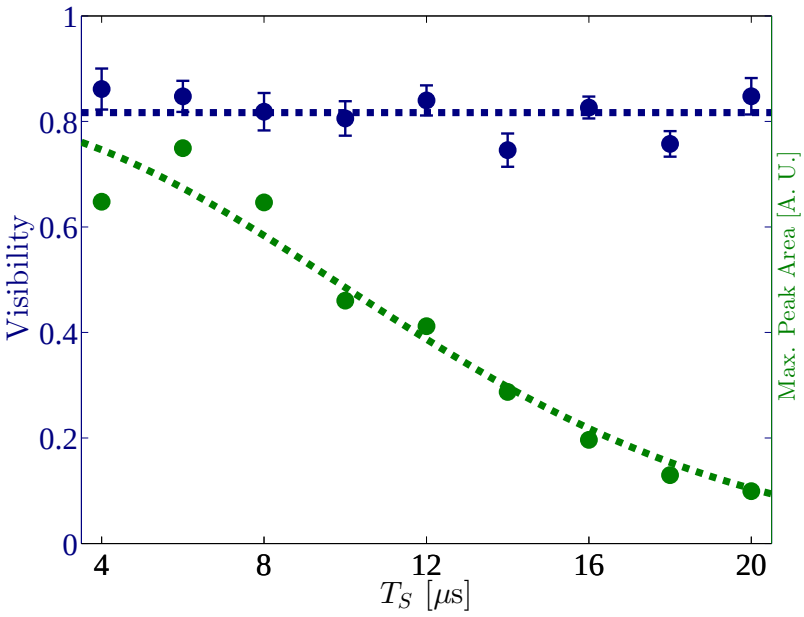

FIGURE 6.12: Visibility and maximum interference area vs. T_S. The blue dots correspond to the measured visibilty values whereas the green dots are the maximum interference area. For each T_S, an interference fringe is measured from which the visibility is extracted via a weighted fit. The error bar is a confidence interval of this fit of one standard deviation. The horizontal dotted line is the mean of the visibilites, $\bar{\mathrm{V}} = 81.7 \pm 1.4\,\%$. The dashed line is a fit using Eq. 6.1 with a corresponding spin inhomogeneity of $\gamma_{\mathrm{IS}} = 26.8 \pm 1.7\,\mathrm{kHz}$.

cryostat's operation cycle, as explained in Sec. 4.2. This shows the efficacy of the synchronization of the AFC experiments with the cryostat. The observed visibility is similar to the ones observed in the spin-state storage experiments, confirming that storing in the ground state does not affect the coherence. This also indicates that the main source of decoherence is the limited coherence of the laser itself, and not the storage and retrieval process.

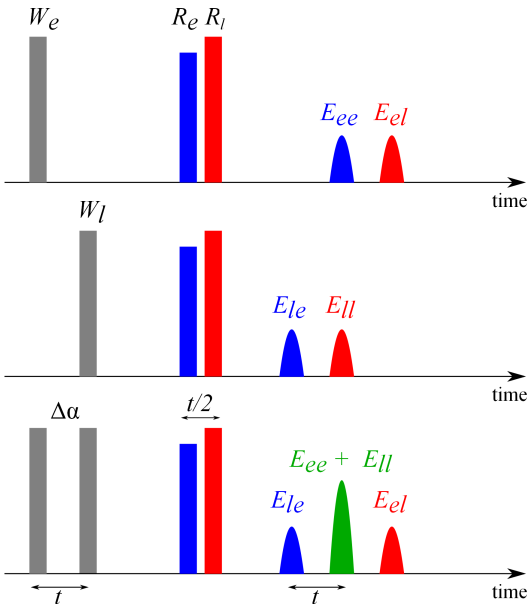

(a)

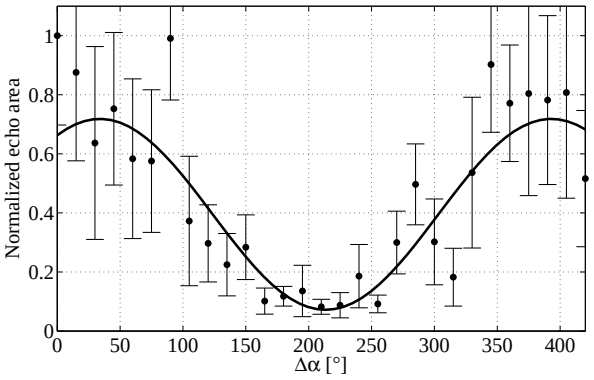

(b)

FIGURE 6.13: (a) The schematic of the time-bin interference experiment with two-pulse echo technique. W_e (R_e) and W_l (R_l) are the early and late writing (read-out) pulses, respectively. Two temporally separated echoes (E_{ee} and E_{el} for W_e pulse, for instance) are observed due to the double read-out pulses. (b) Interference observed in the $E_{ee} + E_{ll}$ region as the phase between the two write pulses, $\Delta\alpha$ is changed. Each data point is an average of 10 experimental trials and the error bars represent the standard deviation.

6.3.5 Multimode Storage

Temporal multimode storage capacity is of crucial importance in quantum memories as it speeds up the entanglement distribution rate in a quantum repeater network by considerable amount [36, 41] over more conventional techniques, such as Ref. [40], where only a single temporal mode can be stored in the memory. This capability has been demonstrated with the two-level AFC [136, 137], where the experiments were performed with REIDs that do not have appropriate ground level electronic structures ($Nd^{3+}Y_2SiO_5$ and Tm^{3+}YAG) for spin-state storage for on-demand retrieval. The maximum number of temporal modes that can be stored

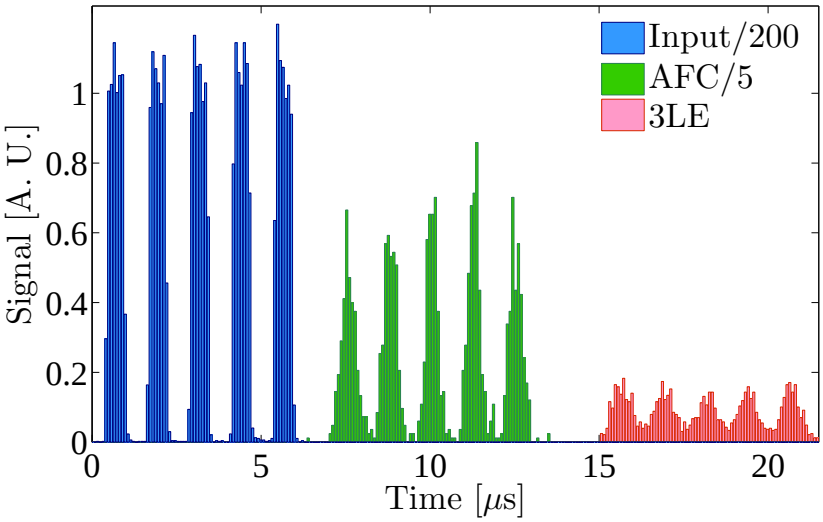

FIGURE 6.14: Spin-wave AFC storage of 5 temporal modes. The AFC delay is $\tau = 7\mu s$ with $T_S = 7\mu s$. The blue bars from $t = 0 - 6\mu$s show 5 distinct temporal modes whose height are divided by 200 for visualization. The green bars show the 2-level AFC echo divided by 5 while the red bars show the 3-level echo.

(N_{max}) in an AFC memory is limited by the number of teeth (N_{teeth}) in the AFC [81]. This can be understood in terms of the ratio between the duration of each input mode and the total duration of the pulse train. The

former is limited by the comb bandwidth whereas the the latter is limited by the AFC storage time and thus by the width and number of teeth that can fit in the comb bandwidth.

For the two-level AFC experiments, great amount of work have been made to increase the comb width [136], up to GHz bandwidth [137, 139]. This is however not possible for the systems that allow for the spin-state storage as the comb bandwidth is already limited by the narrow hyperfine splitting. This splitting ranges from a few MHz in Pr-doped solids to tens of MHz for Eu-doped solids.

In order to increase the multimode capacity of spin-wave storage, the main task then becomes the tailoring of narrow individual AFC teeth, so that longer two-level storage times would be possible. In this way, number of temporal modes stored in the memory can be increased to some extent. However, there are two limitations; firstly, the AFC bandwidth is limited by the hyperfine splittings, which is 4.8 MHz in our choice of Λ-system in Pr^{3+} :Y_2SiO_5. The second limitation is that the width of an individual AFC tooth is technically limited by the linewidth of the laser (~ 100 kHz). However, it is ultimately determined by the homogeneous linewidth of the Pr^{+3} ion (~ 3 kHz, [77]).

The efficiency of the storage and retrieval process directly depends on the available Ω_R which is limited by the available optical power in the experiment. One needs to apply long control pulses in order to compensate for the low optical power to maximize the pulse area. However, this now limits the bandwidth of the memory and also requires long input pulses. The overall effect is the reduction in the number of temporal modes can be stored in the memory. So, the extension of the results presented in the preceding sections to temporal multimode case is not straightforward. Performing the multimode storage experiment with strong ($\sim \mu$W) input pulses can result in the emission of a two pulse photon echo, accumulated echo, or in the worst case, destroy the comb itself by pumping the atoms that constitutes the AFC to some other levels. So, in order to avoid

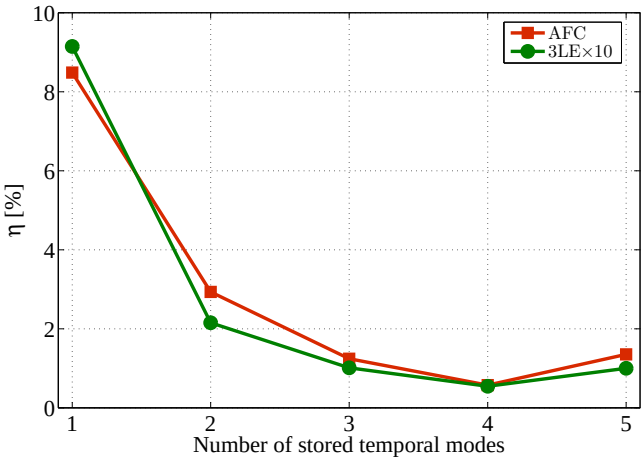

FIGURE 6.15: Three level efficiency vs. number of stored temporal modes. For one mode, $\tau = 3\,\mu$s and for each increase in temporal mode number, an additional μs is set for the AFC storage time.

these undermining events, we performed the multimode storage experiment with very low power input pulses that are attenuated to a level of around $\sim 2 \times 10^4$ photons per pulse. The recalled echoes are then detected with a single-photon detector (SPD; model Count, Laser Components). Additional neutral density filters are placed before the SPD to avoid saturation. An AOM in the double-pass configuration is used to gate any noise stemming from the strong beam. 500 trials are done for each AFC preparation. The electronic signal from the SPD is sent to a time stamping card (Signadyne) which collects the arrival times in a histogram.

Fig. 6.14 shows the time histogram of the storage and retrieval of 5 temporal modes using the full AFC scheme. A 2 MHz wide AFC with $\Delta = 133$ kHz (corresponds to AFC storage time, $\tau = 7\,\mu$s) with $N_{\text{teeth}} = 15$ is programmed. A total of 1×10^5 (2×10^6) pulse trains were used to observe the AFC (3LE) echo. The requirements of a long AFC storage time and of short input pulses contribute to the decrease of the 3LE efficiency with respect to the optimized case of a single mode storage shown in Fig. 6.4.

Indeed both the two level AFC echo and the transfer efficiency are decreased compared to Fig. 6.4. In fact, the total efficiency for the storage and retrieval of 5 modes is here limited to 0.1%. A confirmation of the fact that the overall efficiency strongly depends on the AFC storage time comes from Fig. 6.15, which shows the 3LE efficiency as a function of temporal mode number. As the number of modes is decreased, a shorter AFC storage time is used and higher efficiencies can be achieved. Despite the low efficiency observed, this is to the best of our knowledge the first reported demonstration of spin-wave storage of more than two temporal modes in a doped crystal.

6.4 Discussion

A significant increase of the spin-wave storage efficiencies reported in this chapter is necessary to be viable for use in quantum communication. However, there are some strategies to increase the overall efficiency. One of them is to use a material with high optical depth. This can be realized by either using a crystal with higher ion doping concentration (in the expense of decreased coherence time due to increased ion-ion interactions) or using a longer crystal, as shown in [121]. Another method is to place the memory crystal inside an "impedance matched" cavity as proposed in Ref. [149, 176] and recently realized by Ref. [131]. In that experiment, a spin-state storage efficiency, $\eta_{3\mathrm{LE}}$ of $12,\%$ is observed in $Eu^{3+}:Y_2SiO_5$ crystal, with 100 ppm Eu^{3+} concentration.

Reabsorption of the emitted light limits the efficiency of the AFC scheme to 54 % as in the case of controlled reversible inhomogeneous broadening [86]. However, retrieval with unit efficiency is in principle possible by retrieving the light in the backward direction [81] by using counter-propagating control pulses. Although this has not yet been demonstrated it is already feasible with the current experimental configuration we have in our lab.

Another way to increase the retrieval efficiency is to use special pulses having hyperbolic secant temporal shapes with a hyperbolic tangent frequency chirp [135]. This would overcome the limitations imposed by the temporally square, single-frequency π-pulses and provides a better transfer over the relevant spectral region. This method would require less optical power than single frequency π-pulses for a given transfer efficiency. The AFC preparation can be optimized to yield higher efficiencies, as discussed in Secs. 3.3.1 and 8.2.1 (see also Figs. 3.6 and 3.7).

The inhomogeneous spin broadening of the hyperfine levels limits the storage time of our memory to around $20\,\mu$s. However, this limitation can be overcome by means of RF spin echo techniques which counteracts the dephasing due to the inhomogeneity of the spin states. Dynamical decoupling (DD) techniques can further increase the storage time by reducing the decoherence induced by the environment of the ion (see 2.3.1.1 and 2.3.1.2). These RF based methods have been successfully implemented in Pr^{3+} :Y_2SiO_5 [109, 177], Pr^{3+}:$La_2(WO_4)_3$[178] and Tm^{3+}:YAG [179].

Lastly, the coherence time can be increased by the application of a finely adjusted external magnetic field [75, 180]. When applied with a certain angle and an amplitude the first order Zeeman shift of the electronic states become negligible thus it reduces the sensitivity of the absorbing ions to the magnetic field fluctuations which are mostly created by the neighbouring spins [75, 180]. However, this mostly comes with a drawback of a reduced bandwidth since the degeneracy of the hyperfine levels are lifted with the applied external magnetic field. This method, implemented together with a DD sequence resulted in a storage time of around 1 min, the longest ever storage time achieved in any physical system [110].

The experiment presented in this chapter suffers from the laser linewidth. I should note that the excited state storage time, τ, is limited by the comb spacing Δ, which is in turn limited by the laser linewidth. So, having a narrower linewidth laser would lead to longer storage times in the excited state by creating tighter AFCs. The multimode capacity of the memory

would also benefit from such an improvement. The laser system used in this experiment (Secs. 4.1.2 and 4.1.3) was limited to producing AFC echoes for storage times of up to at most around 10 μs ($\eta_{\mathrm{AFC}} \approx 1\,\%$)for$\tau = 7\,\mu$s.

6.5 Conclusions

In this chapter I presented experiments on coherent and temporal multimode storage of classical light using the full AFC memory protocol. We could obtain efficiencies up to $\eta_{3\mathrm{LE}} = 5.6\,\%$ the highest reported at the time. However, later on Ref. [131] reached $\eta_{3\mathrm{LE}} \cong 12\,\%$ by placing the memory inside an optical cavity following the proposal of Ref. [149]. We also demonstrated for the first time the preservation of the coherence during the storage in the spin-states by performing time-bin interference experiments. We observed an average visibility of 81.7 %, independent of the storage time. We additionally demonstrated the storage and on-demand recall of up to 5 temporal modes, highest number of modes stored as spin-waves in a REID-based optical memory[1].

In the next chapter, I will present experiments where we extended these results to the single photon regime. This is particularly challenging due to the fact that the strong control pulses create noise, in the form of scattering, fluorescence and free-induction decay. Most of this noise is emitted at the frequency of the control pulse, which 10.2 MHz away from the retrieved signal. This narrow separation of the hyperfine levels makes the spectral filtering challenging for our system.

[1] The Geneva Group also reported the storage and on-demand recall of 5 temporal modes recently [181].

Chapter 7

Solid-state quantum memory for time-bin qubits

7.1 Introduction

Storage and on-demand recall of quantum information carried by photons is a crucial task in quantum information science. As mentioned in Chapter 1, it enables the synchronization of different probabilistic processes and thus can be used in scalable photonic quantum information networks, optical quantum computing and long-distance quantum communication with quantum repeaters.

In this chapter, I will describe experiments where we extend the results of the previous chapter to the storage and on-demand retrieval of single photon level pulses with high signal-to-noise ratio (SNR). This is not straightforward, as the noise generated by the strong control pulses can dominate the weak signal retrieved from the memory. Two main mechanisms are responsible for this noise: *i)* Spatial leakage from the control pulses to the detection mode due to the scattering from the optical surfaces such and *ii)* interaction of the control pulses with the residual population remaining

in the spin-storage state due to imperfect optical pumping. This interaction includes both collective effects, such as free-induction decay (FID) and incoherent fluorescent emission. In order to filter out these noises, we employed a series of different filtering strategies namely, spatial, temporal and spectral. Especially, the spectral filtering in $Pr^{3+}:Y_2SiO_5$ is particularly challenging as the control and input pulse frequencies differ only by 10.2 MHz. Therefore, this task requires a very narrow-band filter which we realized by using a second crystal of the same kind, in which we prepare a spectral hole with variable width [182, 183].

7.2 Experimental description

7.2.1 Optical setup

We again make use of the full atomic frequency comb (AFC) scheme, as described in Section 3.3.2. This experiment, however, features the new laser system at 606 nm (Toptica TA-SHG pro) described in Section 4.1.4. of this thesis.

The experimental setup is shown in Fig. 7.1a. The relevant energy level scheme of Pr^{3+} at 606 nm is shown in Fig. 7.1b. The main laser beam at 606 nm is split into three to be used as input mode, filter preparation, and lastly for control pulses and the memory preparation. They all pass through acousto-optical modulators (AOMs) in double-pass configuration, driven by an arbitrary waveform generator (Signadyne), to create the necessary pulse sequences. The beams are then carried with polarization-maintaining single-mode optical fibers to the other optical table where the cryostat is located.

The memory and filter crystals are located inside a liquid-free cooler (Oxford V14) operating at a temperature of 2.5 K. They are both 3 mm long and doped with a Pr^{3+} concentration of 0.05 %. The control and input beams are steered towards the memory with an angle of $\sim 1.5\,°$, to reduce

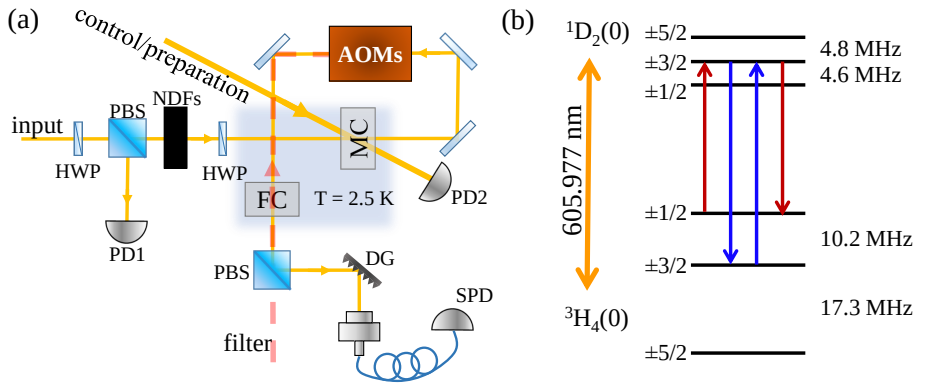

FIGURE 7.1: (a) Quantum memory setup. MC: memory crystal, FC: filtering crystal, PBS: polarizing beam splitter, AOMs: acousto-optic modulators, NDFs: neutral density filters, HWP: half-wave plate, PD: photodiode, SPD: single photon detector and DG: diffraction grating. (b) Hyperfine splitting of the first sublevels of the ground $^3H_4$ and the excited $^1D_2$ manifold of Pr^{3+} :Y_2SiO_5 Red (blue) arrows indicate the input (control) fields.

the spatial leakage from the control pulses to the input mode. This angle leads to an extinction ratio of 10^{-5}.

The beam diameters on the crystal are 280 μm and 90 μm for strong and input modes, respectively. The weak coherent states are prepared by attenuating bright pulses with variable neutral density filters (NDFs). A portion of the input beam is picked up before the NDFs with a combination of polarizing beam splitter (PBS) and a half-wave plate (HWP) and sent to a photodiode (PD1) for the calibration of the mean photon number per pulse. A mechanical shutter (not displayed) is used to protect the single photon detector (SPD) during the memory and filter preparation.

The maximum available optical powers are about 20 mW, 3.5 mW and 20 μW for control, filter preparation, and input modes, respectively, measured in front of the cryostat. The frequency of the 606 nm laser is stabilized by Pound-Drever-Hall technique to a home-made temperature controlled Fabry-Perot cavity housed in a vacuum chamber (see Sec 1.1.2.).

The input light is linearly polarized close to the optical D_2 axis to maximize the interaction with the Pr^{3+} ions. The measured optical depth of the Pr^{3+} transition at 606 nm is about 7 for both memory and filter crystal. In both cases, the inhomogeneous linewidth is about 6 GHz. After the storage, the retrieved signal passes through different diffraction order modes (-1st and 1st) of two consecutive AOMs, acting as temporal gate before passing through the filter crystal. This configuration allows us to keep the central frequency of the retrieved field unchanged after passing through the AOMs and thus providing spectral matching with the narrow-band filter. They additionally help to reduce the afterpulsing in the SPD. A diffraction grating is then used to filter the noise not resonant with ${}^1D_2(0) - {}^3H_4(0)$ transition. The retrieved signal is then coupled with 60 % efficiency into a single-mode fiber for connection to the single photon detector (PicoQuant τ SPAD-20, detection efficiency $\eta_d = 60\,\%$, dark count rate ~ 10 Hz). The total transmission of the input beam from the cryostat to the SPD is about 13 %.

7.2.2 AFC and filter preparation and the experimental sequence

We follow the method described in [148, 184] to create the AFC. It should be noted that this method differs substantially from the one used in Chapters 5 and 6 (see Sections 5.4.2 and 6.2.2). We first scan the frequency of the strong beam by 14 MHz in 100 ms to create a wide spectral transmission window (we also refer as *pit*) within the inhomogeneous absorption profile of the ensemble of Pr^{3+} ions (Fig. 7.2a). Afterwards a 2 MHz-wide sweep pulse is applied outside the pit to pump the atoms back to the $1/2_g$ state. This creates a 3.5 MHz-wide absorbing feature corresponding to the $1/2_g - 3/2_e$ transition inside the pit, but also populates the $3/2_g$ state (centred around 5 MHz relative frequency), which in principle must be empty for later transfer of the input field by the control pulses as can be seen in Fig. 7.2b.

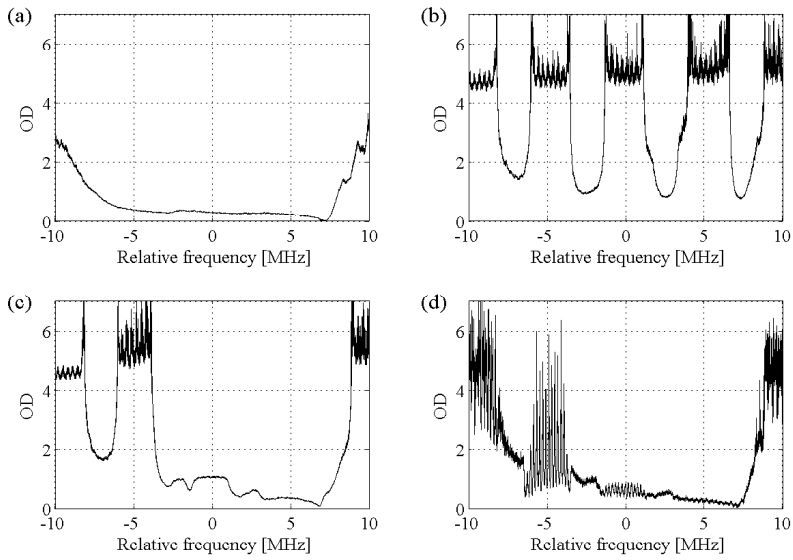

FIGURE 7.2: (a) The transparency window created inside the inhomogeneous line of the ions. (b) Absorption features corresponding to different transitions after the burn-back sweep. (c) After the clean pulse on the $3/2_g - 3/2_e$ transition is applied. (d) AFC with $\Delta = 200\,\text{kHz}$ on the $1/2_g - 3/2_e$ transition centered at $-5\,\text{MHz}$ in the figure.

Also seen in the same figure is the absorption feature corresponding to the $1/2_g - 5/2_e$ transition, centred around 0 MHz relative frequency. In order to remove the unwanted population in the $3/2_g$ state, a 2 MHz clean pulse with a duration of 50 ms is applied on the $3/2_g - 3/2_e$ transition. The clean pulse also contributes to suppress the transitions of different classes of Pr^{3+} ions which might be addressed by the preparation pulses [169]. The resulting structure is shown in Fig. 7.2c.

To create the AFC, a sequence of single-frequency hole-burning pulses is applied on the single class absorption feature resonant with the $1/2_g - 3/2_e$ transition, each time changing the frequency by a fixed amount, Δ. This sequence burns periodically spaced holes in the absorbing feature corresponding to the $1/2_g - 3/2_e$ transition and anti-holes at the frequency of the $3/2_g - 3/2_e$ transition, so after each hole-burning pulse a short burst

of clean pulse is applied to maintain the $3/2_g$ state empty. For the AFC preparation it is crucial to have a third ground state ($5/2_g$) to use as auxiliary state where to store the excess of population resulting from the optical pumping. Finally, before starting the storage experiments, we send a series of 100 pulses that are identical to the control pulses to remove the residual population in the $3/2_g$ state. The resulting comb structure for $\Delta = 200\,\text{kHz}$ is shown in Fig. 7.2d (also the green curve in Fig. 7.3).

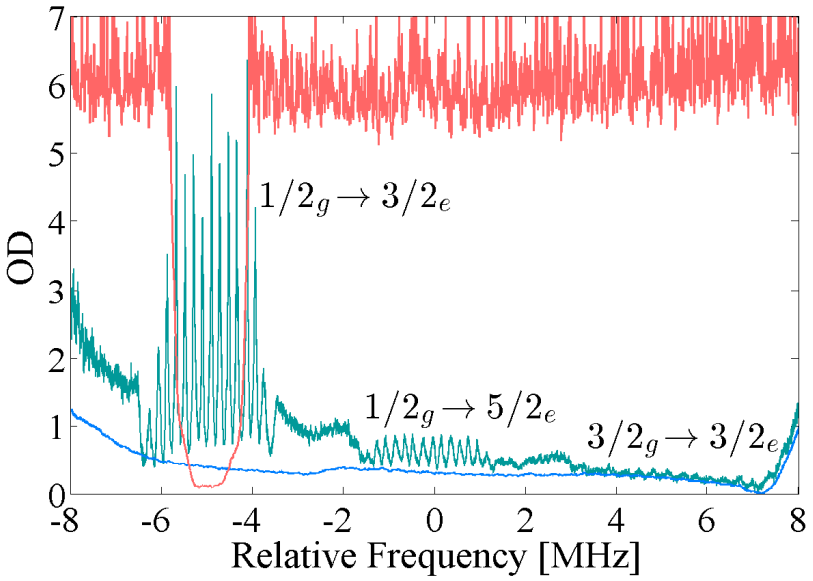

FIGURE 7.3: The narrow spectral filter prepared in a second $Pr^{3+}:Y_2SiO_5$ crystal is shown in red. The blue and green curves represent the empty pit and the AFC shown in Fig 7.2a and 7.2d, respectively.

This value, which gives rise to an excited state storage time, $\tau = 5\,\mu\text{s}$ is kept throughout all the experiments presented in this chapter. We are able to create AFC peaks as narrow as $(43 \pm 3)\,\text{kHz}$ with a peak optical density (OD), $d = 4.5 \pm 0.1$, finesse, $\text{F} = 4.7 \pm 0.4$ and a background OD, $d_0 = 0.75 \pm 0.04$ with this procedure. It should be noted that the limited dynamical range of the detector (Thorlabs PDA150B) may lead to the underestimation of the peak ODs which results in overestimation of the full width half maxima (FWHM) of the AFC peaks. As a result, the measured

AFC parameters reported here must be taken as conservative estimates. From Eq. 3.20, we expect a two-level AFC efficiency of $\eta_{\mathrm{AFC},th} = 12.2 \pm 1.6\,\%$. When the memory is tested with classical pulses, we find efficiencies of $\eta_{\mathrm{AFC}} = 10.3 \pm .4\,\%$ and $\eta_{3\mathrm{LE}} = 4.4 \pm 0.1\,\%$. The measured η_{AFC} is compatible with the expected value within error bars. It should be noted that the residual absorption, d_0 limits the memory efficiency, as shown in Fig. 3.6. The model estimates an efficiency, $\eta_{\mathrm{AFC},th} \approx 29\,\%$ for $F = 4$. Even higher efficiencies can be obtained with the method described in Ref. [130] by creating square-shaped peaks in the AFC (see Fig. 3.7).

The advantage of this method over the one described in Sec. 5.4.2 is twofold: i) For a narrow-linewidth laser, the width of the peaks that make up the AFC is limited by the optical homogeneous linewidth ($\sim 2-3\,\mathrm{kHz}$), whereas in the case of the burn-back method, it is limited by the spin-inhomogeneous broadening ($\sim 26\,\mathrm{kHz}$). ii) One can better approximate square shaped peaks, which in the end allows significantly higher two-level AFC echo efficiencies (Fig. 3.7).

The frequency filter is prepared in the second crystal inside the cryostat simultaneously with the spectral pit created in the memory crystal by using the third optical path (red dashed lines in Fig. 7.1). The frequency of the filter preparation beam is scanned around 1.2 MHz which creates a spectral hole of $\sim 2\,\mathrm{MHz}$ wide (red curve in Fig. 7.3) due to the power broadening effect. Center frequency and the width of the filter can be adjusted by the AOM which allows a great deal of spectral flexibility in terms of the filter width and position.

As in the previous chapters, we send a series of input pulses after an AFC and the filter is tailored. Gaussian input pulses with FWHM width of 430 ns are prepared with an AOM and then attenuated to the single photon level with the NDFs, creating a weak coherent state $|\alpha\rangle$ with mean photon number $|\alpha|^2 = \mu_{in}$. After the absorption of the input pulse by the AFC, two 700 ns-long Gaussian control pulses that are spectrally chirped by 5 MHz are applied on the $3/2_{\mathrm{e}} - 3/2_{\mathrm{g}}$ transition to transfer the input

photons to and from the spin state. For each prepared AFC, 1000 storage pulses together with 1000 pairs of control pulses are sent to the memory with a repetition rate of $\sim 7\,\mathrm{kHz}$. This cycle, including the memory preparation, repeats every 700 ms, synchronized with the cryostat cycle to minimize the effect of mechanical vibrations (see Sec. 4.2). The choice of the repetition rate is motivated by the minimization of the noise due to accumulated fluorescence. The sequence is then repeated 500 to 1000 times to accumulate sufficient statistics.

7.3 Results

7.3.1 Spin-wave AFC storage with weak coherent states

Fig. 7.4(a) shows the time histograms of the retrieved pulses with varying μ_{in}. The spectral width of the crystal filter is set to $\sim 2\,\mathrm{MHz}$ (red curve in Fig. 7.3) for this experiment and the spin-state storage time, T_S to $7.8\,\mu\mathrm{s}$ that yields a total storage time of $\tau_s = 1/\Delta + T_S = 12.8\mu s$. After each AFC preparation a series of 1000 storage trials are performed and the whole experiment is repeated 200 times.

We first characterize the unconditional noise floor of our device. This is performed by executing the whole memory sequence without sending any input pulses (blue bars in Fig. 7.4(a) and 7.4(b)). From this, we estimate the noise floor to be $(2.0 \pm 0.3) \times 10^{-3}$ photons per pulse at the memory crystal. Here, the error is introduced by the error in the optical losses from in front of the cryostat and until the SPD. After determining the noise floor, we send pulses with weak coherent states and obtain an SNR of 16.3 ± 2.4 for $\mu_{in} = 1.15$ (green bars).

Fig. 7.5 shows the linear scaling of the SNR with respect to increasing μ_{in} for the case of a narrow (light red, 2 MHz wide), a large (light blue, 14 MHz wide) spectral filter and finally the crystal filter totally by-passed (light green). The typical AFC and spin-wave efficiencies are observed to

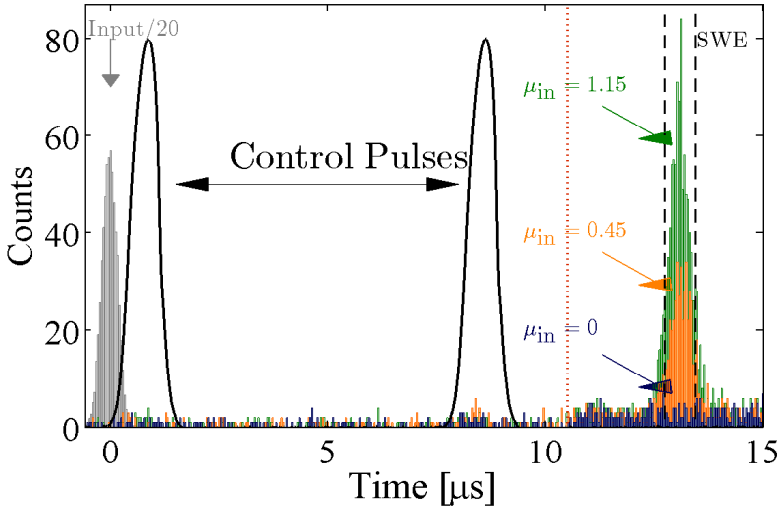

(a)

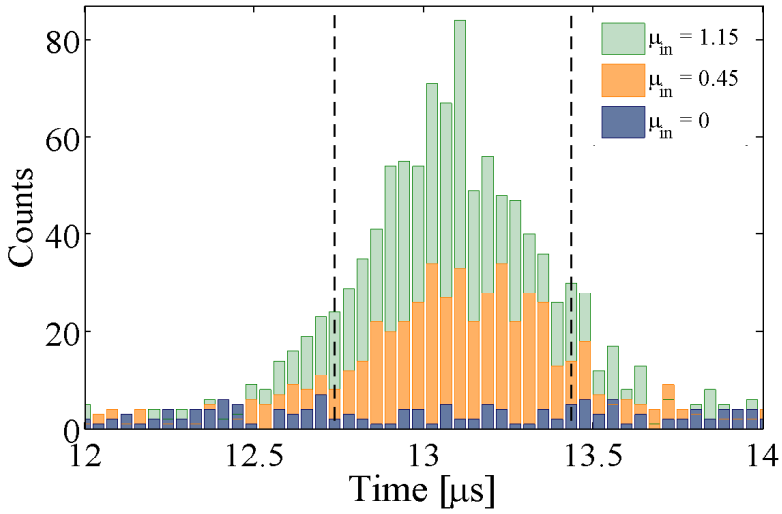

(b)

FIGURE 7.4: (a) Time histograms of the retrieved photons measured for different input photon numbers when a transparency window 2 MHz wide is prepared in the filter crystal. The input ($\mu_{in} = 0.9$) and the control pulses, as measured in photon counting and from a reference photodiode (PD2 in Fig.7.1), respectively, are also displayed. The chosen 0.7 μs wide detection window is indicated by the dashed lines about the three-level echo; it includes $\sim 80\,\%$ of the counts in the full echo mode. Red vertical dashed line after 10 μs indicates the opening of the gating AOMs. (b) Detalied view of the detection window.

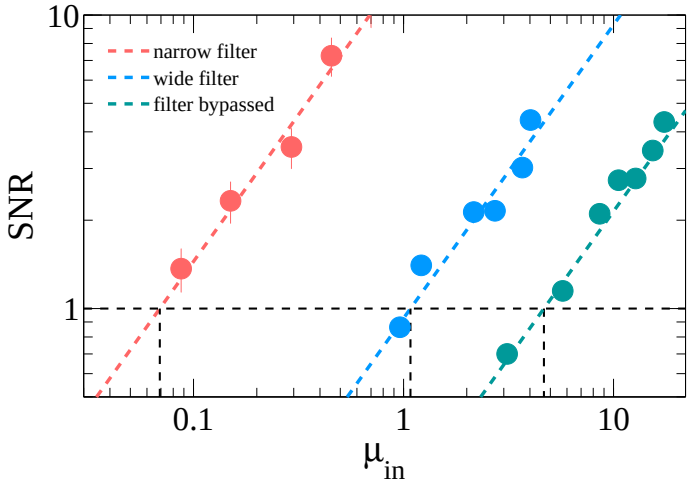

FIGURE 7.5: Signal-to-noise ratio (SNR) as a function of the number of input photons for different filter width. Light red: 2 MHz; Light blue: 14 MHz; Light green: when the filter crystal is bypassed. The error bars (mostly smaller than the data points) are evaluated with Poissonian statistics. The black dashed line indicates the limit of detection SNR = 1. The dotted lines are linear fits of the experimental data.

be around $\eta_{AFC} = (5.6 \pm 0.3)\,\%$ and $\eta_{SW} = (2.8 \pm 0.1)\,\%$, from which we deduce $\eta_T = (81.7 \pm 2.6)\,\%$ (assuming $\eta_C \sim 75\,\%$ [155]). The decrease in the efficiencies when operating in the photon counting mode with the respect to the classical operation can be attributed to various technical reasons, such as, the detection window taken ($\sim 80\,\%$ of the counts), loss in the narrow-band filter ($\sim 10\,\%$ loss) and instabilities due to longer integration times ($\sim 10\,\%$ loss). Here we introduce μ_1, the minimum number of photons at the input that is required to detect a spin-wave echo with a SNR = 1. μ_1 is a useful figure of merit to characterize the memory performance in terms of the noise and the efficiency.

The linear fit to the experimental data in Fig. 7.5 for the narrow filter case yields a $\mu_1 = 0.069 \pm 0.002$. Afterwards we measured the SNR for different τ_s by changing T_S with $\mu_{in} = 1$, as shown in Fig. 7.6. The inferred spin inhomogeneous broadening from the decay is $\gamma_{in} = (26 \pm 1)\,\text{kHz}$, which is

similar to the values measured in other experiments performed with bright pulses [134, 155]. The observed SNR for $T_S = 18.8\,\mu$s ($\tau_s = 23.8\,\mu$s) is still $= 4.5 \pm 0.4$.

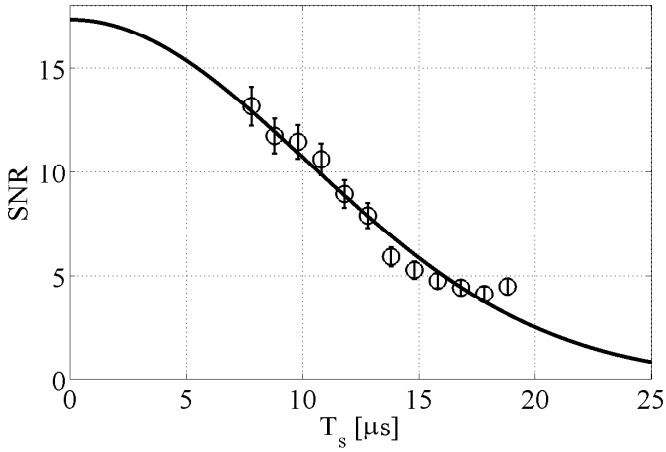

FIGURE 7.6: Decay of the SNR as a function of the spin-wave storage time T_S with $\mu_{in} = 1$. The spin inhomogeneous broadening $\gamma_{in} = (26 \pm 1)\,$kHz can be extrapolated from the Gaussian fit.

The decoherence term η_C in Eq. 3.23 can be inferred by extrapolating the SNR we measure at a storage time $T_S = 7.8\,\mu$s to $T_S = 0\,\mu$s. This yields a η_C of around 75 %.

7.3.2 Filter performance

The figure of merit for the characterization of the filter is the extinction ratio. As it is already mentioned it is quite challenging to filter the noise photons just 10.2 MHz away from the signal photons with high extinction ratio. We first prepare a 2 MHz wide spectral filter in the second crystal at the frequency of the AFC, as shown in Fig. 7.3 (red trace). For these experiments, only a wide spectral pit (blue trace in Fig. 7.3) is created in the memory crystal without preparing the AFC. The extinction ratio of the filter then can be assessed by sending the input pulse at the AFC

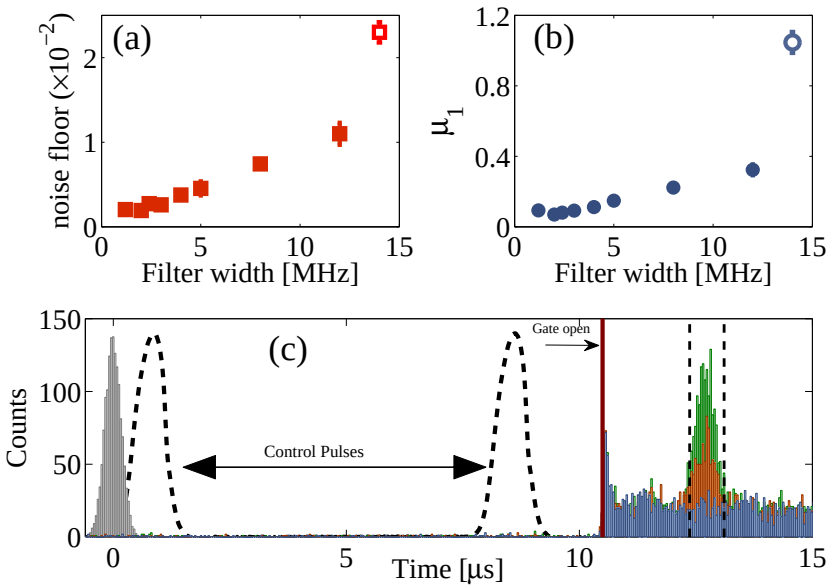

FIGURE 7.7: (a) The noise floor measured in the echo window and (b) The μ_1 value as a function of the spectral filter width. Filled symbols: hole centered at the input pulse frequency; open symbols: transparency window coincident with that prepared in the memory crystal.(c) Time histogram of the retrieved photons for different input photon numbers, μ_{in} (green 3.7, brown 1.2 and blue 0) with a filter width of 14 MHz. Red vertical line denotes the moment when the gating AOM is switched on. Grey bars show the input/10 with $\mu_{in} = 0.9$. Control pulses measured with a reference photodector are also displayed.

frequency and later at the control pulse frequencies and then comparing the detected counts in the two cases. In this way, the extinction ratio of the filter is measured to be around 750. This number compares very favorably to another kind of filter we considered, using a Fabry-Perot cavity (see Sec. B.2).

The contribution of the filter crystal in the suppression of the noise can be further analysed by measuring the noise with different filter widths. Here, the fact that the filter is prepared by spectral hole burning brings an additional flexibility, i.e. one can prepare filters width different parameters. The data shown in light blue in Fig. 7.5 plots the SNR with respect to

the μ_{in} with a 14 MHz wide spectral filter, having the same width as the spectral pit in the memory crystal. This means that there is no spectral filtering at the control pulse frequency. An increase in the noise floor to $(2.3 \pm 0.6) \times 10^{-2}$ is observed, together with a slight increase in the retrieval efficiency ($\eta_{SW} = (2.9 \pm 0.2)\,\%$). This, now results in μ_1 values up to around 1. However, if the filter crystal is bypassed, the noise floor increases to (0.23 ± 0.01), suggesting that the inhomogeneously broadened absorption line Pr^{3+} ions contributes to partially filter out the noise [145] (light green data in Fig. 7.5). The spin-wave storage efficiency for this set of measurements was slightly higher. We observe $\eta_{SW} = (5.3 \pm 0.5)\,\%$, resulting in a μ_1 value of about 4 (see Fig. 7.5).

7.3.3 On-demand quantum storage of time-bin qubits

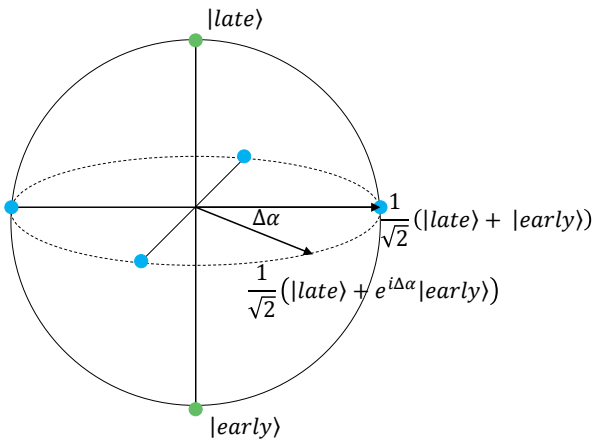

FIGURE 7.8: Representation of time-bin qubits in the Bloch sphere. Green dots located on the poles represent the $|late\rangle$ and $|early\rangle$ qubits, whereas the blue dots on the equator represent the superposition states between the two with different phase relations.

Any kind of memory must preserve the coherence of the stored qubits for applications in quantum information and communication science. As in the previous chapter, we exploit the temporal multimode capability of the AFC technique to show the preservation of the phase information

encoded in time-bin qubits during the storage in the spin-states. Time-bin encoding is also used as an alternative to polarization encoding in quantum communication as it is robust against polarization distortions in optical fibers [14].

Any arbitrary time-bin qubit can be represented in the Bloch sphere as shown in Fig. 7.8. The general expression is given as $|\psi_{in}\rangle = c_1|e\rangle + c_2 e^{i\Delta\alpha}|l\rangle$, where $|e\rangle$ ($|l\rangle$) represents a qubit in the early (late) time-bin, $\Delta\alpha$ is their relative phase, and $c_1^2 + c_2^2 = 1$, the normalization condition. Fig. 7.8 shows the early and late qubits (green dots) located in the south and north poles of the Bloch sphere, respectively. Blue dots represents the qubits located on the equator ($c_1 = c_2 = 1/\sqrt{2}$).

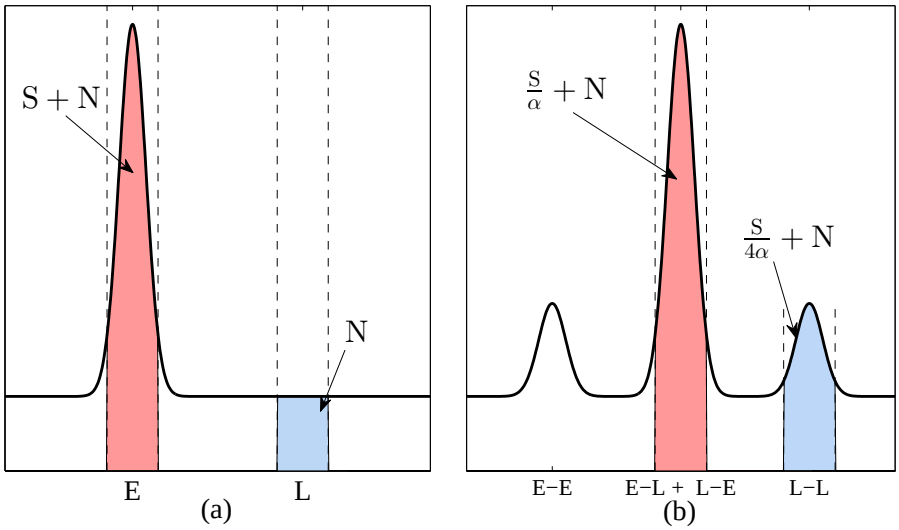

FIGURE 7.9: (a) Schematic example of the memory output for storage of an $|e\rangle$ qubit. (b) Schematic example of the memory output for storage of an $|e\rangle + |l\rangle$ qubit where the relative phases are such that the maximum interference is observed.

We first evaluate the storage and recall fidelities of states $|e\rangle$ and $|l\rangle$, located at the poles of the Bloch sphere, F_e and F_l, by storing only the early and the late qubits for pulses of duration 260 ns. Fig. 7.9a shows the schematic of the outcome of such an experiment where the $|e\rangle$ qubit has been stored

and then recalled. The total detected counts in the window around E is denoted as S + N whereas the counts in the detection window around L is given as N. Here, S represents the number of photons retrieved from the memory, i.e. the signal and N is the noise photons. Under these conditions, the fidelity is given as the ratio of the detected counts in the window E to the total counts over the windows E and L. Namely,

$$\mathrm{F}_e = \frac{\mathrm{S}+\mathrm{N}}{\mathrm{S}+\mathrm{N} \quad + \quad \mathrm{N}} = \frac{\mathrm{S/N}+1}{\mathrm{S/N}+2} = \frac{\mathrm{SNR}+1}{\mathrm{SNR}+2}. \tag{7.1}$$

where SNR is the signal to noise ratio. Assuming that the efficiency and the noise are the same for storing the $|l\rangle$ qubit, $F_l = F_e = F_{el}$. One can also express the above fidelity in Eq. 7.1 in terms of μ_1 of this particular experiment. This can be done by noting that $\mathrm{SNR} = \mu_q/\mu_{1p}$, where μ_{1p} is the μ_1 characteristic of the poles measurement and μ_q is the mean photon number per qubit. The fidelity for the poles then can be written as

$$\mathrm{F}_{el} = \frac{\mu_q + \mu_{1p}}{\mu_q + 2\mu_{1p}}. \tag{7.2}$$

Fig. 7.10a shows the experimental time histogram of the retrieval of the early (light red histogram) and late (light green histogram) input qubits with $\mu_q = 3$. The measured average fidelities,F_{el} range from 85 % to 98 % for photon number per qubit, μ_q, going from 0.6 to 5.9 (See Table 7.1).

We then measure the fidelity of the superposition states in the form of $|e\rangle + |l\rangle$. These states are located on the equator of the Bloch sphere (Fig. 7.8). We use the memory itself to analyse the retrieved qubits [148]. This is done by applying two partial write pulses with a relative phase $\Delta\beta$ to split an input pulse into two, as depicted in Fig. 7.11(a). This results in the emission of two temporally separated echoes. The amplitudes of the partial write pulses are adjusted such that the retrieved echoes have similar amplitudes as well. If we send two input pulses with a relative phase $\Delta\alpha$ that correspond to $|e\rangle$ and $|l\rangle$ qubits with a temporal separation equal to the temporal separation between the partial write pulses, then we

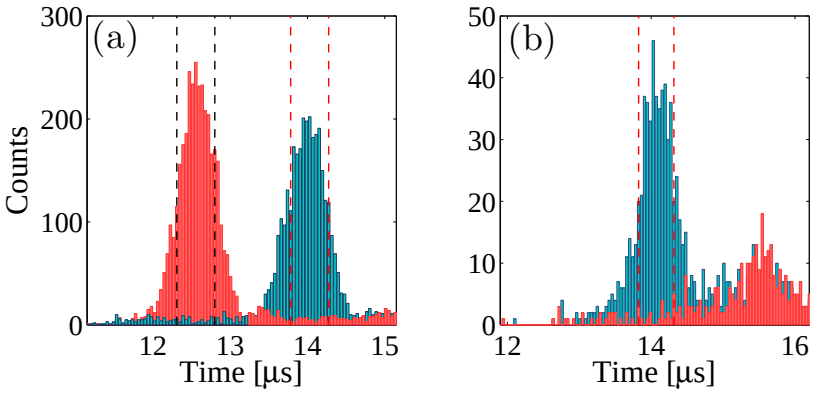

FIGURE 7.10: (a) Detected counts at the output of the memory for the early (light red histogram) and late (light green histogram) input qubits with $\mu_q = 3$. The vertical dashed lines show the 0.5 μs integration windows. (b) Detected counts at the output of the memory for an input qubit $|e\rangle + |l\rangle$ with $\mu_q = 5.9$. The light green (light red) histogram shows the case when the relative phase in the double-write process is adjusted such that the output modes are constructively (destructively) interfered. Output mode on the right corresponds to the L-L window of Fig. 7.9b. while the E-E window is not detected here as the gating AOM is kept closed to block the temporal leakage from the control pulses.

can overlap the late echo of the early bin, $|el\rangle$, with the early echo of the late bin, $|le\rangle$. There are two other temporal modes at the output of the memory, the late echo of the late bin $|ll\rangle$ and the early echo of the early bin $|ee\rangle$. An interference will occur in the central time-bin if the coherence is between the two time-bins is preserved. Here, the normalized count rate detected in the interference window is given by [14]

$$R_C = \frac{1 - V\cos(\alpha + \beta)}{2}, \tag{7.3}$$

where V is the visibility of the interference fringe.

This method conveniently provides a way to analyse time-bin qubits but at the same time suffers from the reduced storage efficiency due to the reduced duration of the input pulses. The duration of the input pulses is

reduced from 430 to 260 ns to store the time-bin qubits for the coherence measurements. This was motivated by the fact that two input pulses should be stored and retrieved in order to analyse the superposition states in the form of $|e\rangle + |l\rangle$. This modification of the pulse width results in reduced spin-wave storage efficiency ($\eta_{SW} = 2.2\,\%$) which in turn leads to an increased μ_1, which we now denote as μ_{1p}. In this configuration, we measured $\mu_{1p} = 0.11 \pm 0.01$.

Fig. 7.9(b) shows an arbitrary superposition qubit $|e\rangle + |l\rangle$ being retrieved from the memory with a relative phase $\Delta\alpha$ between the two time-bins. Here, $\Delta\alpha$ is such that the maximum interference is observed. Similar to the approach above, the detected counts in the window around the time E-E is given as $\mathrm{S}/4\alpha + \mathrm{N}$ where the signal S is the same as defined earlier. The difference here is that now the signal S is reduced by a factor of 4. There are two reasons for this 4-fold reduction; the first one is that μ_q is now distributed equally between the two input time-bins and secondly, the echo is distributed again equally between the two output time-bins. The other feature that should be noted is that the reduction in the storage efficiency due to the reduced pulse duration for the double-write process. This reduction of efficiency is denoted with factor α.

The signal detected in the central time-bin E-L + L-E is 4 times that of the signals in the L-L and E-E windows as long as the interference is fully coherent. The resulting number of counts in the central time-bin then becomes $\mathrm{S}/\alpha + \mathrm{N}$.

The fidelity of the states on the equator of the Bloch sphere is calculated from the visibility of the interference fringe by $F = (1 + V)/2$ [14], where the visibility V is defined as

$$\begin{aligned} V &= \frac{\max - \min}{\max + \min} = \frac{\mathrm{S}/\alpha + \mathrm{N} \;-\; \mathrm{N}}{\mathrm{S}/\alpha + \mathrm{N} \;+\; \mathrm{N}} \\ &= \frac{\mathrm{S}}{\mathrm{S} + 2\mathrm{N}\alpha} = \frac{\mathrm{SNR}}{\mathrm{SNR} + 2\alpha} \end{aligned} \tag{7.4}$$

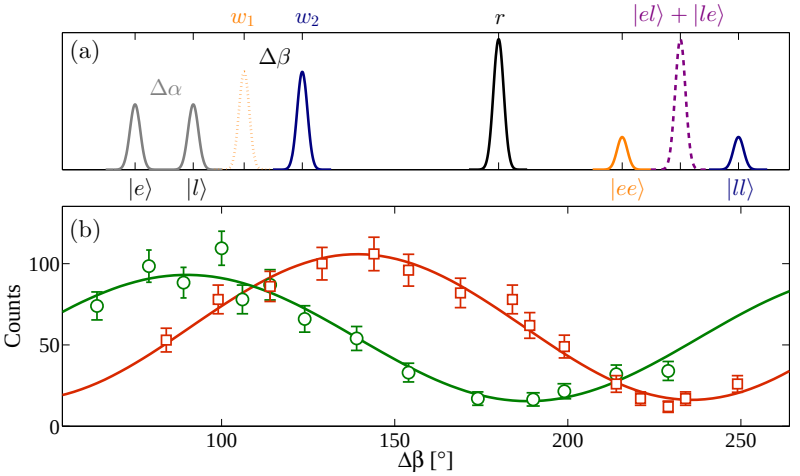

FIGURE 7.11: (a) Pulse sequence for the time-bit qubit coherence measurement. See text for details. (b) Interference fringes obtained integrating over the central output time-bin (in this case $\Delta t_d = 0.5\,\mu$s) as a function of the relative phase difference $\Delta\beta$ for $\mu_q = 1.5$. Circles: $\Delta\alpha = 90\,°$, $V = (71.6 \pm 6.8)\,\%$; Squares: $\Delta\alpha = 135\,°$, $V = (73.4 \pm 3.5)\,\%$.

where max (min) refers to the maximum (minimum) integrated counts of the fringe, the max being $\mathrm{S}/\alpha + \mathrm{N}$ and min being N. Note that we have V in terms of the SNR of the poles measurement, so the resulting fidelity can be written in terms of μ_{1p}, i.e.

$$\mathrm{F}_{+-} = \frac{1}{2} + \frac{1}{2}\frac{\mu_q}{\mu_q + 2\alpha\mu_{1p}}, \tag{7.5}$$

where the subscript $+(-)$ refers to the qubit $|e\rangle \pm |l\rangle$ ($|e\rangle \pm i|l\rangle$), and we assume $\mathrm{F}_+ = \mathrm{F}_- = \mathrm{F}_{+-}$. We measure α by comparing the μ_1 in the L-L window of figure 7.9 to μ_{1p} and we measure $\alpha = 2.5 \pm 0.6$. The overall fidelity for each μ_q is given by

$$\mathrm{F}_T = \frac{1}{3}\mathrm{F}_{el} + \frac{2}{3}\mathrm{F}_{+-}, \tag{7.6}$$

where F_{el} is the average fidelity measured in the the poles (equator) basis. F_T can be written in terms of μ_q and μ_{1p} by combining Equations 7.2 and

7.5 as follows,

$$\mathrm{F}_T = \frac{1}{3}\left[\frac{\mu_q + \mu_{1p}}{\mu_q + 2\mu_{1p}}\right] + \frac{1}{3}\left[1 + \frac{\mu_q}{\mu_q + 2\alpha\mu_{1p}}\right]. \tag{7.7}$$

In Fig. 7.11(b) we plot different interference fringes for $\mu_q = 1.5$. We obtain a raw visibility of $V_{+-} = (72.5 \pm 1.3)\,\%$ from the sinusoidal fits. We then calculate F_T according to the Eq. 7.6 and the resulting values are shown in Fig. 7.12 for different μ_q and listed in Table 7.1. We fit the data in Fig. 7.12 with equation 7.7 taking α as a free parameter. We obtain $\alpha = 2.5 \pm 0.3$ from the fit which agrees quite well with the measured value of $\alpha = 2.5 \pm 0.6$ that is stated above. The excellent agreement between the model and the experiment shows that the reduction of F_T while decreasing μ_q is due to the noise created by the control pulses and not by any loss of coherence during the storage and retrieval process.

Similar to the analysis we performed in Chapter 4, the total fidelity is compared with the highest fidelity that can be achieved with a measure-and-prepare strategy in order to assess the quantum nature of the memory (solid curve in Fig. 7.12). Again, as in Chapter 4, one should also take into account the finite memory efficiency (2.2 %) and the Poissionian statistics of the input states [152, 160, 184]. Our experimental data show that the F_T surpasses the classical threshold for most of the tested μ_q. According to the raw data, our spin-wave memory operates in the quantum regime for $\mu_q > 0.96$. Our model predicts that the memory could surpass the classical limit for $\mu_q > 0.25$ if the time-bin qubit analysis would be done with an external interferometer instead of the double-write procedure that we employed here (grey and red lines in Fig. 7.12).

The very low noise floor and the ability to obtain $\mu_1 \ll 1$ paves the way for the spin-wave storage of heralded single-photons as required in many quantum information and communication applications [185]. The probability to have an input photon at the memory (also called the *heralding efficiency*) should be higher than μ_1 in order to operate in the quantum regime for the storage of heralded single-photons. In a previous experiment in our lab,

μ_q	F_{el}	F_{+-}	F_T	F_C
5.9	$(97.9 \pm 1.5)\%$	$(97.2 \pm 1.7)\%$	$(97.4 \pm 1.2)\%$	$(93.0 \pm 0.1)\%$
3.2	$(96.9 \pm 2.2)\%$	$(93.3 \pm 1.2)\%$	$(94.5 \pm 1.1)\%$	$(90.1 \pm 0.1)\%$
1.5	$(93.5 \pm 2.9)\%$	$(86.2 \pm 1.6)\%$	$(88.6 \pm 1.4)\%$	$(86.2 \pm 0.1)\%$
1.1	$(93.3 \pm 3.1)\%$	$(85.8 \pm 1.5)\%$	$(88.3 \pm 1.4)\%$	$(84.4 \pm 0.1)\%$
0.6	$(84.9 \pm 4.2)\%$	$(72.9 \pm 1.3)\%$	$(76.9 \pm 1.6)\%$	$(81.0 \pm 0.1)\%$

TABLE 7.1: Fidelities $\mathcal{F}_{el}$, $\mathcal{F}_{+-}$ and $\mathcal{F}_T$ for each μ_q tested. F_C is the classical benchmark for testing the device with weak coherent states which depends on the efficiency of the memory and the input photon number used [152, 160]. The stated errors are one standard deviation.

where the heralded single photons from an ultra narrow-band spontaneous parametric down conversion source [62] the heralding efficiency was around 5 %. The μ_1 values reached in this experiment are still larger than that, but the current efforts in the lab are focused to increase the heralding efficiency of the single photons and also to increase the storage efficiency by using a longer crystal, for example. We should note that much higher efficiencies (for storage in the excited state) have been obtained with $Pr^3+:Y_2SiO_5$ using a longer crystal (69 %) [121] or an impedance matched cavity (58 %) [151]. As discussed in Sec. 7.2.2, there are several bottlenecks in the experiment that can be eliminated and improved. The finite background absorption, d_0, limits the achievable efficiency to around ± 10 % instead of a possible ± 26 % (see Fig. 3.7). The other improvement can come by preparing square-shaped AFC peaks [130]. Lastly, as for the storage in the spin-states, the limited transfer efficiency in the current experiment could be further improved to ensure higher storage efficiencies. This can be implemented by using more complex techniques, such as rapid adiabatic pulses [186, 187]. Also, the spatial overlap between the control and the input modes could be aligned better to yield higher efficiencies.

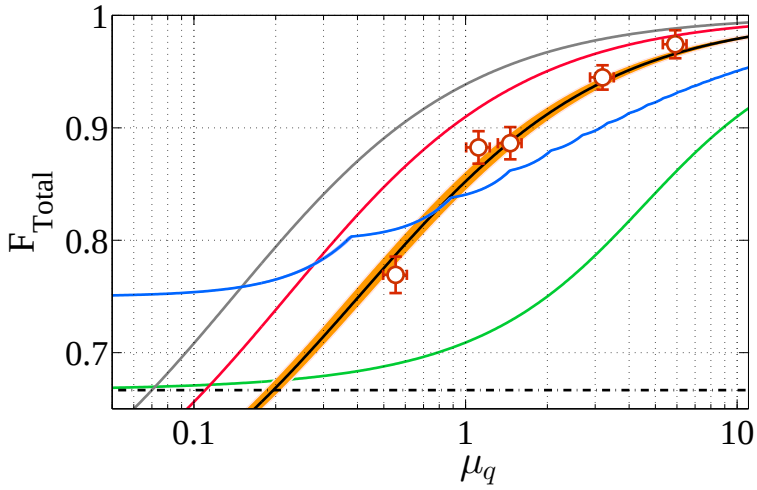

FIGURE 7.12: Total fidelity vs input photon number per qubit, μ_q. The red circles are the data points with an error bar of 1 standard deviation. The black line is a fit to the data points using Eq. 7.7, with the corresponding shaded area being the 1 standard deviation of the error in this fit. The solid blue (green) line is the limit obtained by a measure and prepare strategy for our memory efficiency of $\eta_{SW} = 2.2\,\%$ ($\eta_{SW} = 100\,\%$) when testing the memory with weak coherent states [152]. The dash-dotted line is the classical limit for testing the memory with a single-photon Fock state ($F = 2/3$). The red line shows the case for $\alpha = 1$, with $\mu_{1p} = 0.11$, i.e. the case where our detection of the coherence is replaced by an unbalanced Mach-Zehnder interferometer, for example. Grey line shows the case for $\alpha = 1$, with $\mu_{1p} = 0.07$, i.e. the μ_1 measured for the optimised pulse bandwidth case.

7.4 Conclusions

To sum up, we showed the storage and on-demand retrieval of single-photon level light pulses in a $Pr^3{+}Y_2SiO_5$ system with SNR > 10 for pulses with $\mu_{in} \approx 1$. The high SNR then allowed us to store time-bin qubits encoded again with weak coherent states with conditional fidelities higher than the one that can be achieved with a measure-and-prepare strategies. This in the end proved the quantum character of our storage device and made it the first QM for time bin qubits with on demand read-out. Our results now extend the capabilities of REID based quantum memories to

the long-sought on-demand read-out functionality. These results open the door for long-lived storage and on-demand readout of non-classical states of light in solid state devices and represent an important step in view of using solid state quantum memories in scalable quantum networking architectures. In parallel to our experiment, single photon spin-wave storage has also been reported in an Eu^{3+}-doped crystal [181].

Chapter 8

Conclusions and outlook

This chapter will summarize the results presented in this thesis and put those results in a larger context in the quantum information and communication science. I will comment on how the present results could be further improved and lastly present the future research that be built on the results of this thesis.

8.1 Summary of the work done

The main emphasis of this thesis is the storage of photonic qubits in a rare-earth ion doped (REID) crystal memory basen on Pr^{3+} :Y_2SiO_5 crystal. The thesis started with the construction of the lab from scratch. This stage included the building and the characterization of the coherent laser source, resonant with the Pr^{3+} ions at 606 nm based on sum-frequency generation. Other experimental work at the early stages contains setting up the cryostat and designing the required pulse sequences for the first spectroscopy experiments.

Our first contribution to the field is quantum storage of polarization qubits in the Pr^{3+}-doped crystal [152]. We observed storage and recall fidelities

of $> 95\,\%$, only limited by the detector dark counts. Our results extended the capabilities of REID based memories to the widely used polarization encoding and thus strengthening their position amongst other quantum memory implementations. Nevertheless, this experiment was limited to the excited state storage with pre-determined storage time of 500 ns due to the unstabilized laser at the time.

The frequency of the laser was then stabilized to a Fabry-Perot cavity which in the end made the implementation of the full AFC protocol possible. The elimination of the relatively large frequency jitter enabled us to create narrower AFC peaks, thus resulting in an increased two-level storage times. As a figure of merit, we had efficiencies of around 10 % for a storage time of 500 ns with the unstabilized laser, whereas similar efficiencies can be obtained for storage times of $\sim 5\,\mu$s after the laser is stabilized. The increased storage time in the excited state enabled us to insert the required strong control pulses for the transfer of the excitations to and from the long-lived hyperfine ground levels to implement the full AFC protocol [81, 134].

Afterwards we went on with experiments where we demonstrated that the coherence is preserved during the storage and retrieval of the stored excitations in the spin-states [155]. We observed $\eta_{3\mathrm{LE}} \sim 5\,\%$, the highest efficiency in a single-pass configuration at the time. Further, we stored and recalled up to 5 temporal modes on-demand in the spin-states, the highest reported until then. Recently, spin-state storage of up to 5 temporal modes has been demonstrated in a $Eu^{3+}Y_2SiO_5$ crystal, in the single excitation regime [181].

This experiment represented our first step towards the on-demand storage of single-photon level light pulses in the spin-states. However, the main challenge was to suppress the noise created by the control pulses as the frequency separation between the control and the input fields is only 10.2 MHz. This narrow separation required a sophisticated filtering to reach the single-photon level, combining spatial, spectral and temporal

filtering. We implemented a narrow-band spectral filter based on spectral hole burning in a second crystal [182, 183]. The filtering strategy we employed finally allowed us to reach an unconditional noise floor of $(2.0 \pm 0.3) \times 10^{-3}$ photons per pulse at the memory crystal. When combined with the efficiency $\eta_{3\mathrm{LE}} \approx 2.2\,\%$ it translates into an SNR of > 10 for inputs with mean photon number ~ 1. The high SNR we obtained finally opened the way for the storage and on-demand retrieval of time-bin qubits. Our results showed again that the fidelity of the process surpasses the one that could be achieved with a measure and prepare strategy for mean photon numbers per qubit, $\mu_q > 0.96$. This finally marks our device as the first optical quantum memory with on-demand readout for time-bin qubits realized in any physical system.

The results presented in this thesis form a coherent progress in the quantum memory field, strengthening the position of REID systems as candidates for nodes of a scalable quantum network. They also form the basis for the future experiments in the lab, which will be detailed in the next section.

8.2 Outlook

8.2.1 Potential improvements

The performances of our quantum memory can be significantly improved. An important improvement would be an increase in the storage and retrieval efficiency. This can be ameliorated by using different types of control pulses, for example hyperbolic secant type [179, 188, 189] or rapid adiabatic passage techniques [186, 187] might prove useful to increase the transfer efficiency of the control pulses. Implementation of these pulses would require further detailed study, and most probably longer storage times in the excited state. The limited transfer efficiency, $\eta_T \approx 82\,\%$,

reported in Chapter 7 could thus be increased to almost unity by appropriate design of control pulses. However, this would not be enough by itself to boost the overall efficiency. The overall efficiency is bounded by the highest obtainable η_{AFC}, which, in our case is around 12 % for a storage time of 5 μs. The maximum value that can be obtained in our crystal with OD = 5 is around 38 %, as can be seen from Fig. 3.7. The main reason of the lower efficiency is due to the imperfect preparation of the AFC and the background absorption d_0, as explained in Sec. 3.3.1. This currently limits the potential gain of using longer crystal with larger optical depths. A potential solution would be to create the AFC by pumping the crystal from the side, using an optically thin path, as demonstrated in [121]. Other techniques to create AFCs using coherent pulses might also lead to better quality combs [131, 181]. Further increase can come by the application of control pulses in a counter-propagating configuration [81]. All these strategies are technically feasible currently in our lab. As a last resort, placing the memory inside an impedance-matched cavity, as proposed in [149] and demonstrated in [151] would effectively increase the efficiency without the need of increasing the material OD.

Storage time in the excited can be extended by better stabilizing the laser which would allow us to tailor narrower AFC peaks. This way, the separation between the AFC peaks, Δ, can be made smaller to yield longer storage times in the excited state. This improvement would bring a second advantage, namely the increase in the number of modes, N, that can be stored in the memory. This would be possible by preparing AFCs with larger number of peaks as it determines the maximum N.

Lastly, the storage time in the spin-states can be increased by means of spin-echo, dynamic-decoupling and zero first order Zeeman shift techniques [75, 177] by many orders of magnitudes [109, 110, 178]. Spin-echo technique has recently been used to store weak coherent states with $\bar{n} = 1$ in an AFC memory in Eu^{3+}:Y_2SiO_5 crystal. The storage time has been extended to around 500 μs [181], almost a factor of 20 more than what it is possible without employing any decoherence control method [148]. Similar strategy

would boost the storage time of our quantum memory and when combined with the above-mentioned strategies to increase the efficiency, it would make our device an excellent candidate for a realistic quantum repeater node.

8.2.2 Future directions

Our work fills an important gap in the field of quantum memories in the sense that now the storage of non-classical states of light in the long-lived ground states of a solid becomes feasible. The immediate efforts in our lab are concentrated on the storage of heralded single photons from an ultra-narrow band photon pair source [62]. We could successfully store the heralded single photons from the source in the excited states of the Pr^{3+} ions, again with the AFC method [145]. The challenge that is faced in the lab at the moment is that the heralded single photons have a duration of $\sim 100\,\text{ns}$, making them spectrally larger than the AFC. This spectral mismatch would result in lower η_{AFC} as well as lower transfer efficiencies to and from the spin-states. The important figure of merit for this experiment is the heralding efficiency, η^H, defined as the probability of having a single photon heralded by the presence of the other photon (in our case it is at telecom wavelength, 1436 nm) of the pair. It has been shown that the condition $\eta^H > \mu_1$ should be satisfied to successfully store the heralded single photons in the spin-states of the memory with a SNR > 1 [145, 181, 185]. The current value of $\eta^H \approx 0.25$ achieved in the lab seems well above the value $\mu_1 \approx 0.07$ that has been presented in this thesis, nevertheless, the above-mentioned spectral mismatch between the heralded single photons and the AFC might require a larger margin between η^H and μ_1.

As we have seen in Section 1.3, connecting distant quantum memories is of vital importance for quantum networking. One might need to interface different kinds of memories as well. One of the most commonly used and studied systems in the field is the ensemble of laser cooled Rb atoms. To

this end, connecting a REID-based quantum memory, such as the one presented in this thesis and a cold atomic quantum memory would require quantum frequency converters that do not spoil the information encoded in the signal pulses. In this line of research, our lab first demonstrated a quantum frequency converter based on sum-frequency generation [60] to convert the photons emitted from a Rb quantum memory [61] to the telecom C-band at around 1550 nm. In a different, another frequency converter is implemented to convert the wavelength of these telecom photons to 606 nm to store them in an AFC memory in a Pr^{3+}:Y_2SiO_5 crystal [184]. The next would be to combine these two setups to interface the solid-state AFC memory with the cold atom Rb memory.

Another line of research in the quantum information science and the quantum memory community in particular, is to miniaturize the devices to make them compatible with the existing technology as well for the scalability purposes. So far, quantum dots [190, 191] and NV centers in diamond [192–194] have been investigated intensively. However, these systems suffer from spectral blinking and diffusion when confined to nano scale structures [195, 196]. To overcome this limitation, REID crystals emerged as alternative systems thanks to their already proven capability for applications in quantum information science. An important step towards the miniaturization of REID based quantum memories came out recently from Caltech [146, 197]. Nevertheless, there have already been some experiments with integrated waveguide geometries. These include the works from Calgary [139] with a Tm^{3+}:$LiNbO_3$ and Geneva [175] with Er^{3+}:$LiNbO_3$ waveguides. The first experiment concerned the storage of photonic entanglement whereas the latter showed the interference of photon echoes emitted from separate waveguides. A recent photon echo experiment from ANU has demonstrated an integrated device based on Pr^{3+}:Y_2SiO_5 [198].

Our lab has recently started a collaboration with Politecnico di Milano to realize an integrated optical memory device based on femtosecond laser written [199] waveguides in a Pr^{3+}:Y_2SiO_5 crystal. The first AFC experiments have been performed recently with classical light and the future

work will be focussed on the realization of long-lived on-chip quantum memory for non-classical light.

Appendix A

Modelling the fidelity

In this appendix, I will present the calculations of the classical benchmark of the memory, presented in Fig. 5.10 in Chapter 5.

The main principle behind our approach is to estimate the best obtainable fidelity for a given memory efficiency with a classical strategy. Specifically, we consider that an initial party performs a classical state estimation of the input qubits then stores the result in a classical memory and prepares a new qubit based on the initial measurement. The maximum achievable fidelity in this case, for a constant photon number N is given by [59]

$$F = \frac{N+1}{N+2}. \tag{A.1}$$

If the memory is tested with a Fock state, $N = 1$, then the classical bound becomes 2/3. Instead, if one uses weak coherent states then the probability of having different photon number components should also be taken into account. A pulse of light with a mean photon number μ has a Poissonian probability distribution for different photon number states and it is given by,

$$P(\mu, N) = \mathrm{e}^{-\mu}\, \frac{\mu^N}{N}. \tag{A.2}$$

The maximum achievable fidelity with a classical strategy now becomes a weighted sum over N of the fidelity for a given N where the weight is given by the Poissonian statistics of the input [160]. This is written as,

$$F = \sum_{N\geq 1}^{\infty} \frac{N+1}{N+2} \frac{P(\mu, N)}{1 - P(\mu, 0)}. \tag{A.3}$$

This formula works only if the quantum memory has a storage and retrieval efficiency $\eta_M = 1$. But so far, a quantum memory with unit efficiency is yet to be demonstrated ($\eta_M < 1$). As suggested in Ref [160], a more sophisticated classical strategy could simulate a non-unit efficiency by producing an output for only high photon numbers N, yielding a higher achievable fidelity.

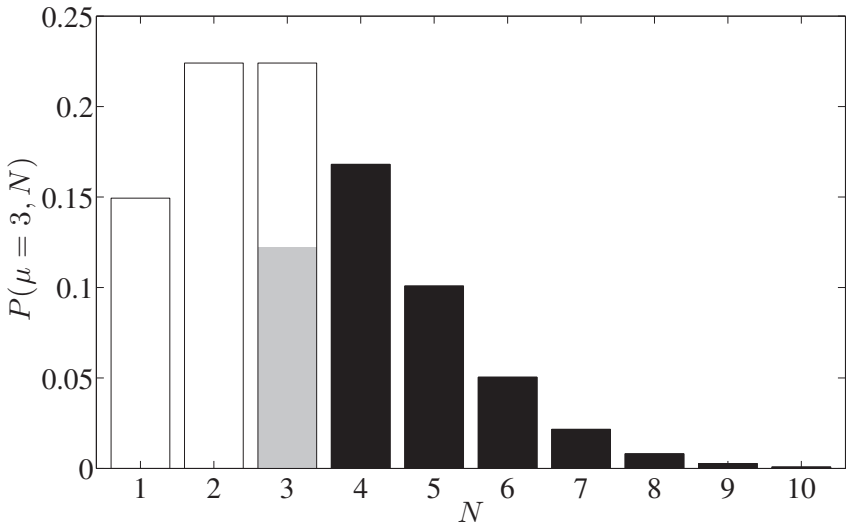

FIGURE A.1: An example of obtaining N_{min}. Plotted above is the probability distribution for a coherent state of $\mu = 3$. The target efficiency here is 50%. For this target efficiency $N_{\text{min}} = 3$, found using Equation A.8. The grey shaded part of bar $N = 3$ plus the black bars $N \geq 4$ equate to the 50% target efficiency.

The classical measure and prepare strategy is considered to be 100 % efficient, but we define the effective classical efficiency η_C as the probability

that the classical device gives an output qubit, if it has received at least one photon as input:

$$\eta_C = \frac{P_{\text{out}}}{1 - P(\mu, 0)}, \tag{A.4}$$

where

$$P_{\text{out}} = \sum_{N \geq N_{\text{min}}+1} P(\mu, N). \tag{A.5}$$

Here, it should be noted that the photon number statistics of the output qubit is not relevant as we do not use photon number resolving detectors. The classical memory can produce a result for some threshold photon number $N_{\text{min}}+1$ and above, and no result for N lower than this. It is important to note that for the above there exists only certain η_{C} for a given mean photon number μ. Hence, not all quantum efficiencies can be simulated by this approach. A more general form of P_{out} which allows for arbitrary number and hence efficiency is the following

$$P_{\text{out}} = \gamma \; + \sum_{N \geq N_{\text{min}}+1} P(\mu, N), \tag{A.6}$$

where now the memory gives a result for N_{min} with a probability of γ, with the condition $\gamma \leq P(\mu, N_{\text{min}})$. The efficiency then becomes

$$\eta_C = \frac{\gamma \; + \sum_{N \geq N_{\text{min}}+1} P(\mu, N)}{1 - P(\mu, 0)}. \tag{A.7}$$

It is now assumed that $\eta_M = \eta_C$. N_{min} is then obtained as follows

$$N_{\text{min}} = \min\, i : \sum_{N \geq i+1} P(\mu, N) \leq (1 - P(\mu, 0))\, \eta_M. \tag{A.8}$$

Figure A.1 shows a graphical representation of obtaining N_{min}.

The maximum achievable classical fidelity using the above described strategy is given as,

$$F_{class} = \frac{\left(\frac{N_{\min}+1}{N_{\min}+2}\right)\gamma + \sum_{N \geq N_{\min}+1} \frac{N+1}{N+2} P(\mu, N)}{\gamma + \sum_{N \geq N_{\min}+1} P(\mu, N)}, \tag{A.9}$$

where γ and $N_{\min}$ are obtained from Equations (A.7, A.8). Figure A.2 shows the fidelity as a function of mean photon number μ for various efficiencies η.

Note that the classical memory could also in principle take advantage of the optical loss and the finite detection efficiencies in the experiment to increase the maximal classical fidelity. In that case, we would have $\eta_C = \eta_M \eta_t \eta_D$, where η_t is the optical transmission from the quantum memory to the detector and η_D is the detection efficiency of the SPD. For our experiment, we have $\eta_M = 0.1$, $\eta_t = 0.4$ and $\eta_D = 0.5$ such that in that case $\eta_C = 0.02$.

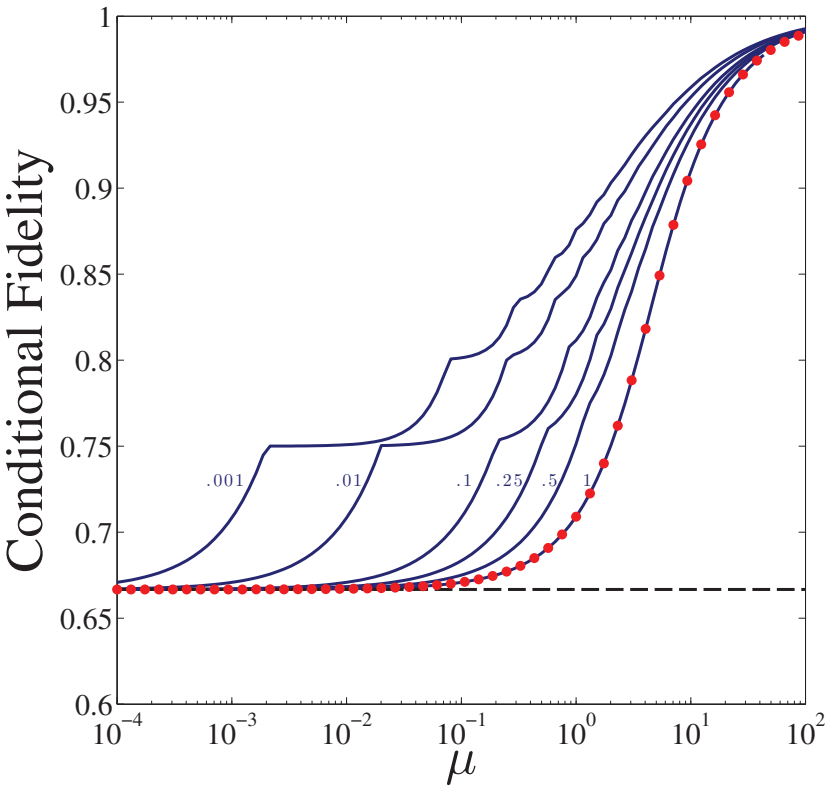

FIGURE A.2: Maximum achievable fidelity using a classical memory as a function of mean photon number μ for different memory efficiencies η (Eq. A.7). The cases shown are $\eta = \{0.001, 0.01, 0.1, 0.25, 0.5, 1\}$. The solid lines are calculated using Equation A.9, the dots are calculated using Equation A.3. It is seen that for $\eta = 1$, Equation A.9 reduces to Equation A.3. The dashed line is for the single photon case $N = 1$.

Appendix B

Additional data for Chapter 7

B.1 Spin-wave AFC results with the SFG laser

We performed the first single-photon level spin-wave storage experiments with the laser system based on sum-frequency generation, which is described in Section 4.1.2. As has been observed in Ref. [148], we observe an echo located $1/\Delta$ after the second control pulse.

The explanation given for this source of noise in Ref. [148] is that it stems from the off-resonant excitation of the AFC by the second control pulse. It is called off-resonant echo (OREO) by the authors of [148]. We later proceeded with the checks performed in [148] in order to make sure that it is of the same origin. Switching off the second control pulse while still preparing a memory makes this peak disappear. Also, if we only prepare an empty spectral pit while keeping the control pulses on makes it disappear as well.

Figure B.1 shows the arrival time histograms for different mean photon numbers at the input, μ_{in}. OREO is seen $5\,\mu$s after the second control

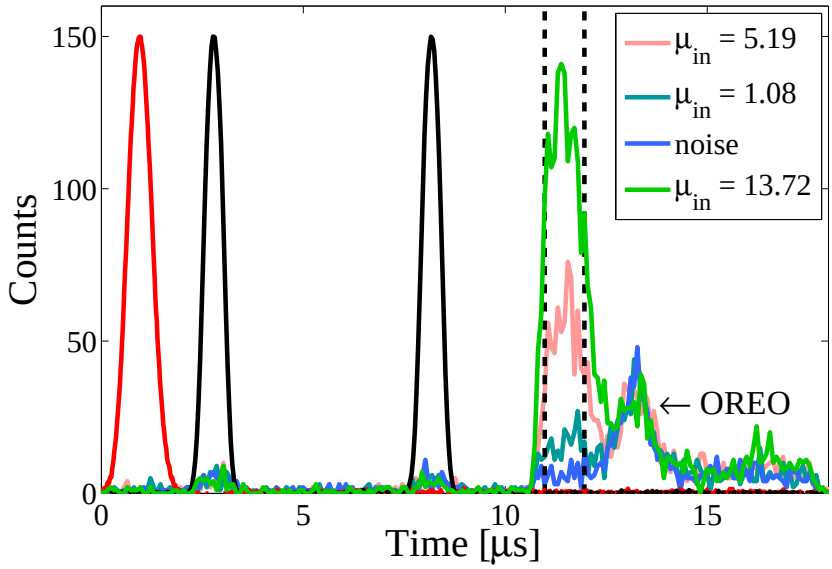

FIGURE B.1: Arrival time histograms for differen μ_{in}, including $\mu_{\text{in}} = 0$. Black traces are the strong control pulses, detected by the reference detector. Red denotes the input pulse, again detected by the reference detector. Vertical dashed lines indicate the detection window (1.05 μs). OREO is clearly seen just after the three-level echo.

pulse. Although it is emitted in a temporally separated mode, it still contributes to the noise in the three level echo detection window.

Fig. B.2 shows the scaling of the SNR with respect to varying μ_{in}. From the data, we infer the $\mu_1 = 0.72$, almost an order of magnitude higher than the value reported in Chapter 7.

This data shows the significant improvement we obtained upon the acquisition of the laser system based on the second harmonic generation of 1212 nm (See section 4.1.4). The reasons of this improvement are not fully understood, but several elements may play a role. First, the system involves only one pump wavelength instead of the two pumps present in the SFG-based system. This facilitates the laser stabilization which leads to higher storage and retrieval efficiencies. Also, due to the absence of the large bandwidth amplified spontaneous emission from the fibre amplifier

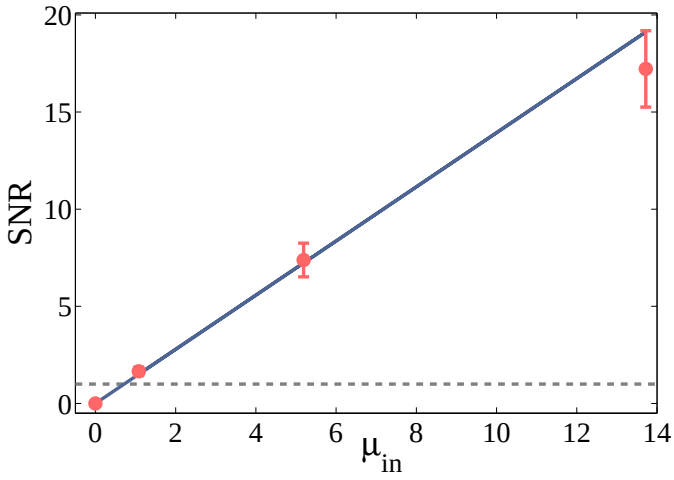

FIGURE B.2: SNR vs. μ_{in}. Data points are shown individually in Fig. B.1. Dashed horizontal line indicates SNR = 1.

at 1570 nm, it is likely that the frequency-doubled laser has a lower noise floor. This could in turn reduce the noise in the memory experiment.

To further study the noise sources, we investigated the interaction of the control pulse with the ions in the memory crystal. Figure B.3(a) shows the time profile of a Gaussian control pulse after it passed through the memory crystal. Fourier transform of the pulse (black trace in Fig B.3(b)) shows that it has an amplitude modulation with a frequency 10.2 MHz. The noise reduces significantly when the same pulse is sent through an empty spectral pit, without an AFC prepared (red trace). This suggests that the imperfect optical pumping and AFC preparation might have left some ions in the $3/2g$ state among which some of them decay to the $1/2g$ state after being excited by the control pulse. This decay results in fluorescence emission with a frequency 10.2 MHz with respect to the control pulse. The apparent oscillation thus might be due to the beating of this fluorescence and the control pulse. Similar beatings were also observed on the emitted two- and three-level echoes in the experiments presented in Chapter 6 (See Fig. 6.4).

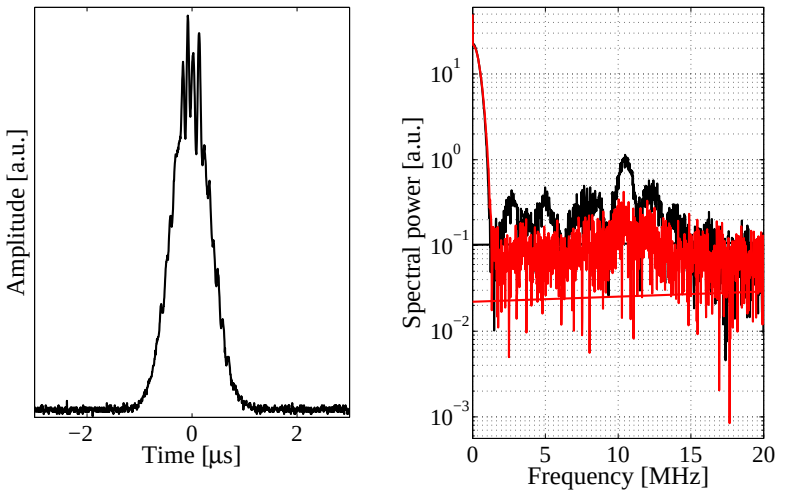

FIGURE B.3: (a) The temporal shape of the control pulse after passing through the memory crystal in the presence of an AFC. A clear amplitude modulation is seen. (b) Black: Fourier transform of the pulse shown in (a) reveals that the amplitude modulation has a frequency of 10.2 MHz. Red: Fourier transform of the control pulse when sent through an empty spectral pit (i.e. without and AFC).

B.2 Narrow-band filter based on a Fabry-Perot cavity

We have tested a Fabry-Perot cavity as a narrow-band filter before adapting the spectral hole based filtering for the single-photon level experiments presented in Chapter 7. This approach had already been demonstrated to be sufficiently effective in suppressing the noise $Eu^{3+}:Y_2SiO_5$ in the same kind of experiments [148]. However in our case, the narrower hyperfine separations puts tighter constraints on the cavity design.

We designed a cavity with a length $L = 6.2\,\text{cm}$. Reflectivity of the mirrors are specified as $R = 0.9986$ by the manufacturer. However, from the measured FWHM of the laser stabilization cavity (the same kind of mirrors are used in both cavities), we infer $R \approx 0.9954$. This value would result

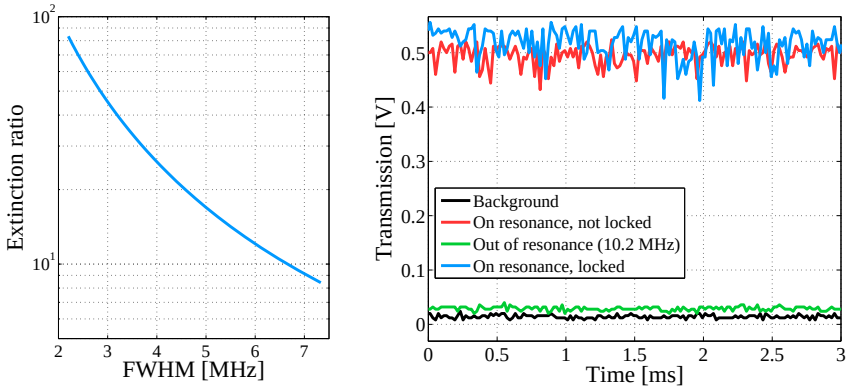

FIGURE B.4: (a) Calculated extinction ratio at 10.2 MHz with respect to the FWHM of the cavity mode. (b) Transmission signals through the cavity.

in an expected in FWHM≈ 3.5 MHz, whereas we measured 3.6 MHz. The corresponding extinction ratio at 10.2 MHz is then calculated to be ~ 30.

The length of the cavity should be stabilized such that the echo photons emitted from the memory would be on resonance with the cavity mode. This is realized by locking the cavity length with a piezoelectric element mounted on one of the mirrors. A portion of the main beam is picked up and its frequency is modulated with an AOM with a frequency of 500 kHz. It is passed through the cavity and detected with a photodiode from which an error signal is produced as described in Appendix C. The feedback signal is then sent to the piezoelectric element. One should note that unlike the case in Sec. 4.1.3, the error signal is produced with the signal that is transmitted through the cavity, not from the reflected beam. The main reason is that the frequency sidebands at ±500 kHz also pass through the cavity. We adopt this approach because unlike the laser frequency stabilization purposes we do not require a fast feed-back, but instead, keeping the cavity on resonance with the echo photons over the experimental time scale would suffice.

Nevertheless, the presence of the strong $\sim \mu$W locking beam would prevent the single-photon level echo signal be detected by the APDs due to reflections and scatterings from optical surfaces, even though the two modes are counter-propagating through the cavity. Thus, we decided to lock the cavity during the memory preparation and switch off the locking beam while the echo photons are being retrieved. Initial checks showed that the cavity remains on resonance during the time scale of the experiments (∼few hundred ms) after the locking beam is switched off. Fig. B.4(b) shows details of the cavity filtering performance. The extinction ratio AT 10.2 MHz is measured to be ~ 30 by comparing the blue and green traces. Transmission drops by 10 % when the locking beam is switched off (the red trace).

Appendix C

Pound-Drever-Hall technique

In this appendix I will outline the basics of the Pound-Drever-Hall technique for laser frequency stabilization. I will mainly follow the approach in Ref. [158].

A Fabry-Perot cavity consists of two highly reflecting mirrors facing each other. The light entering into the cavity thus bounces back and forth many times before totally leaks out. The cavity decay time is given by $\tau = 1/(2\pi\Delta\nu)$, where $\Delta\nu$ is the linewidth of the cavity resonance mode. In our case the cavity has a linewidth of around 1.3 MHz, which yields $\tau \simeq$ 122.4 ns.

The light that is reflected back is now composed of two parts: *i*) the light that is reflected directly from the mirror and *ii*) the light that leaks out after some round-trip inside the cavity. Under the resonance condition, however, these two fields are destructively interfered and most of the light is coupled to the cavity mode. Any drift in frequency of the incoming field would result in non-perfect destructive interference, hence some light will

be reflected back. Here the reflection coefficient is given by,

$$F(\omega) = \frac{r(e^{i2\omega L/c})}{1 - r^2 e^{i2\omega L/c}} \tag{C.1}$$

where r is the reflectivity of cavity mirrors, ω is the frequency of the light, L is the cavity length and c is the speed of light.

If one can sensitively detect the phase of the reflected light, a feedback signal can be extracted to keep the laser frequency locked to the cavity mode. This is done by the PDH method.

A portion of the light from the main beam is picked up and passed through an electro-optic modulator (EOM) for phase modulation with a frequency ω_m. The electric field of the modulated beam then becomes

$$E_{mod} = E_0 e^{i(\omega t + \beta \sin(\omega_m \tau)}, \tag{C.2}$$

which then can be expanded into Bessel functions as

$$E_{mod} = E_0[J_0(\beta)e^{i\omega t} + J_1(\beta)e^{i(\omega+\omega_m)t} - J_1(\beta)e^{i(\omega-\omega_m)t}] \tag{C.3}$$

where β is the modulation depth and J_n is the nth order Bessel function. Higher order terms are omitted assuming β. Here we see that in addition to the main beam at the carrier frequency ω, there are two sidebands at frequencies $\omega \pm \omega_m$. This field is then sent to the Fabry-Perot cavity whose reflection is $F(\omega)$. Now the electric field of the reflected beam can be written as,

$$E_{refl} = E_0[F(\omega)J_0(\beta)e^{i\omega t} + F(\omega+\omega_m)J_1(\beta)e^{i(\omega+\omega_m)t} - F(\omega-\omega_m)J_1(\beta)e^{i(\omega-\omega_m)t}] \tag{C.4}$$

That would result in an intensity given as $P_{refl} = |E_{refl}|^2$ which is detected via a photodiode. In its full-form P_{refl} is expressed as,

$$\begin{aligned} P_{refl} = P_C|F_\omega|^2 + P_S\{|F(\omega+\omega_m)|^2 + |F(\omega-\omega_m)|^2\}+ \\ 2\sqrt{P_C P_S}\{\mathrm{Re}[F(\omega)F^*(\omega+\omega_m) - F^*(\omega)F(\omega-\omega_m)]\cos(\omega_m t) \\ + \mathrm{Im}[F(\omega)F^*(\omega+\omega_m) - F^*(\omega)F(\omega-\omega_m)]\sin(\omega_m t)\} + \mathcal{O}(2\omega_m) \end{aligned} \quad \text{(C.5)}$$

Here P_C and P_S are the powers in the carrier and sideband frequencies, respectively. Weak modulation assumption gives $P_0 \approx P_C + 2P_S$ which means most of the power is contained in the carrier and the first sideband frequencies. We are interested with the terms oscillating at the frequency ω_m to determine the phase of the reflected beam. In order to get this information, the reflected signal is demodulated by mixing it with the signal used to drive the EOM. A phase shifter is used to select either cosine or sine terms. After passing the resulting signal through a low-pass filter we would end up with the terms oscillating with ω_m. If the modulation frequency is large enough (larger than the linewidth of the cavity mode) then we can safely assume that the sidebands are reflected, i.e. $F(\omega-\omega_m) = F(\omega+\omega_m) \approx 1$. Under these conditions the error signal can be written as,

$$\varepsilon = -2\sqrt{P_S P_C}\mathrm{Im}\{F(\omega)F^*(\omega+\omega_m) - F^*(\omega)F(\omega-\omega_m)\}, \quad \text{(C.6)}$$

which is shown in Fig 2.4 (a). If we demodulate P_refl with a $\pi/2$ phase shifted signal we would get the quadrature error signal, shown in Fig C.1 (b). Finally, the produced error signal is sent to a PID feedback circuit to keep the value of the error signal around 0. This is either done by sending the feedback to the piezo controller of the ECDL's grating for small corrections or to the laser diode's current input. Piezoelectric elements typically have response bandwidth of around tens of kHz (in our case 3 kHz), whereas much faster feedback can be sent through the current that feeds the laser diode. Hence simultaneous feedback to both piezo and current is possible to ensure stability in short and long time scales, as

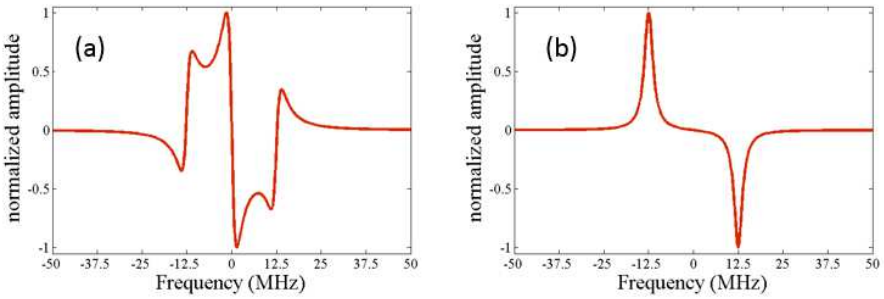

FIGURE C.1: Simulated error (a) and quadrature error (b) signals. Cavity FSR is 1 GHz and ω_m is 12.5 MHz as in our stabilization setup.

well as to enable linewidth reduction. We employed this approach in our stabilization setup.

Appendix D

Classes and class cleaning

In this appendix I will give details of the *class cleaning* procedure mentioned in Secs. 6.2.2 and 7.2.2. Although the procedure in the latter differs slightly, it follows the same logic.

Figure D.1 shows spectral positions of individual transitions of nine different classes of ions (Fig. 2.5) for the $^3H_4(0) -^1 D_2(0)$ optical transition of Pr^{3+} ion. The height of a bar represents the relative oscillator strength of the transition. Values are taken from Ref. [78] and also shown in Table 2.1. Vertical dashed lines show the approximate position of a spectral pit in which an AFC is prepared in experiments presented in Chapters 6 and 7.

A more physical representation is pictured in Figure D.2. Once a spectral pit is prepared (dashed lines in Fig. D.1), a burn-back pulse is applied $\sim 27\,\mathrm{MHz}$ with respect to the center of the pit. This pulse creates the peaks inside the pit as shown in Fig. D.2 (1). Here, different coloured peaks represent transitions that belong to different classes of ions. Later a *clean* pulse is applied around between the dashed lines to remove the unwanted population in the $3/2g$ state of the Class 1 ions for the spin-state storage experiments. This pulse removes the populations in the $1/2g$

state of Class 3 and $1/2g$ and $3/2g$ states of Class 2 ions as well. The end result after such a clean pulse is shown in the middle in Figure D.2.

The repetition of the same procedure with different back-burn pulses with seperations Δ finally creates the AFC on the $1/2g-3/2e$ transition. There is also an AFC on the $1/2g-5/2e$ transition since the population is now in the $1/2g$ state.

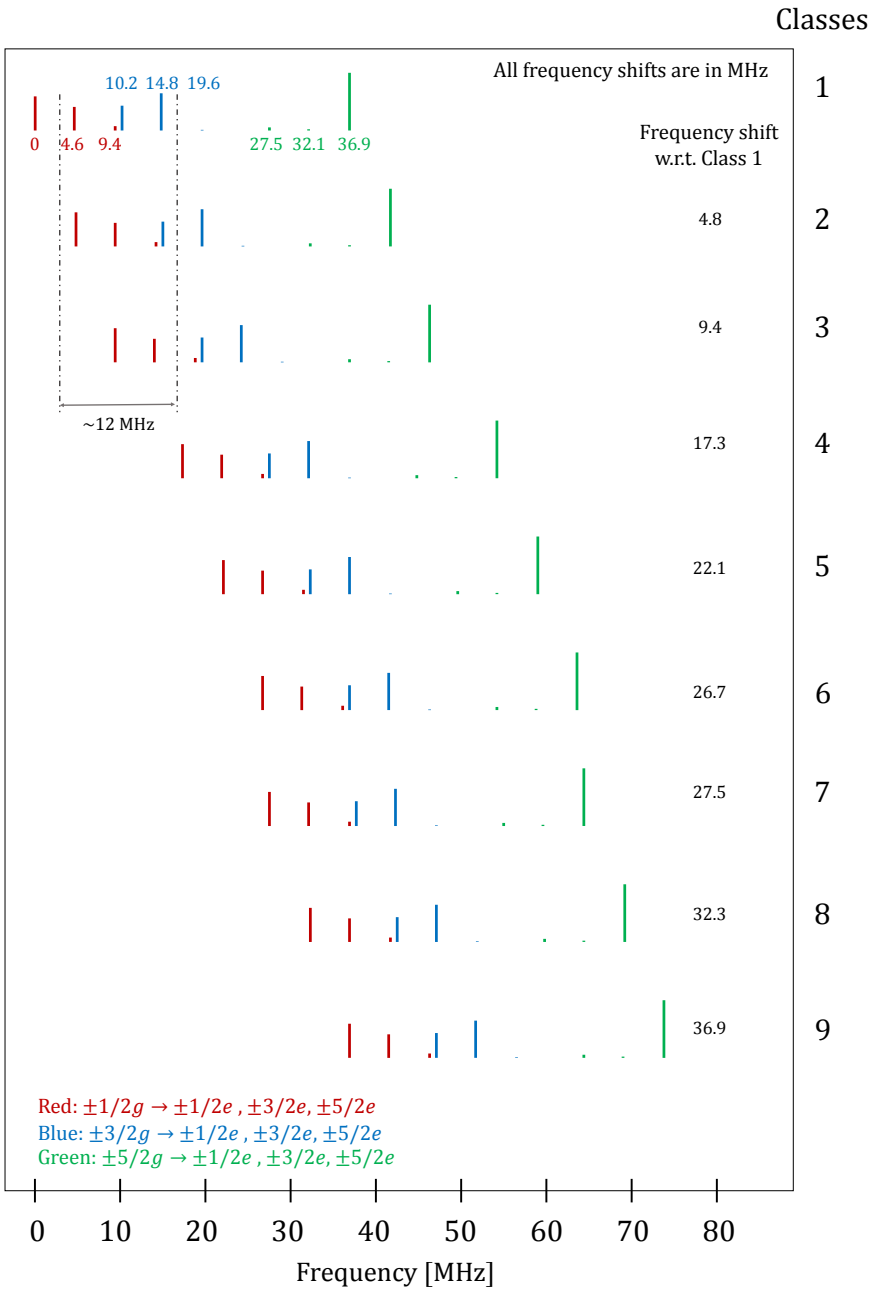

FIGURE D.1: Spectral positions of each possible transition of the 9 different classes shown in Fig. 2.5.Details are in the text.

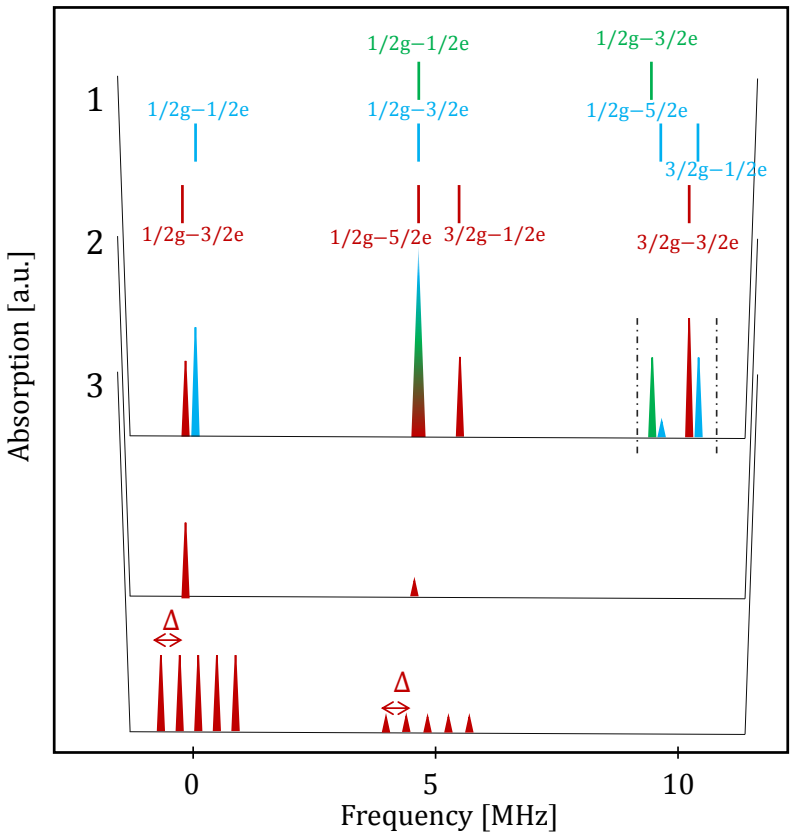

FIGURE D.2: Schematic representation of the AFC preparation with the burn back method and class cleaning. Red: class 1, blue: class 2 and green: class 3. Vertical dashed lines indicate the spectral region where the clean pulse is applied. Details are in the text.

Bibliography

[1] M. A. Nielsen and I. L. Chuang, *Quantum Computation and Quantum Information* (Cambridge University Press, Cambridge, 2000).

[2] M. Lewenstein, A. Sanpera, and V. Ahufinger, *Ultracold Atoms in Optical Lattices: Simulating quantum many-body systems* (Oxford University Press, Oxford, 2012).

[3] N. Gisin, G. Ribordy, W. Tittel, and H. Zbinden, Rev. Mod. Phys. **74**, 145 (2002).

[4] D. Dieks, Phys. Lett. A **92**, 271 (1982).

[5] W. K. Wootters and W. H. Zurek, Nature **299**, 802 (1982).

[6] B. Schumacher, Phys. Rev. A **51**, 2738 (1995).

[7] S. Barnett, *Quantum Information* (Oxford University Press, Oxford, 2009).

[8] B. Roy Bardhan, P. M. Anisimov, M. K. Gupta, K. L. Brown, N. C. Jones, H. Lee, and J. P. Dowling, Phys. Rev. A **85**, 022340 (2012).

[9] B. Roy Bardhan, K. L. Brown, and J. P. Dowling, Phys. Rev. A **88**, 052311 (2013).

[10] J. Brendel, W. Tittel, H. Zbinden, and N. Gisin, Phys. Rev. Lett. **82**, 2594 (1999).

[11] I. Marcikic, H. de Riedmatten, W. Tittel, V. Scarani, H. Zbinden, and N. Gisin, Phys. Rev. A **66**, 062308 (2002).

[12] P. C. Humphreys, B. J. Metcalf, J. B. Spring, M. Moore, X.-M. Jin, M. Barbieri, W. S. Kolthammer, and I. A. Walmsley, Phys. Rev. Lett. **111**, 150501 (2013).

[13] H. Jayakumar, A. Predojevic, T. Kauten, T. Huber, G. S. Solomon, and G. Weihs, Nat. Comm. **5**, 4251 (2014).

[14] I. Marcikic, H. de Riedmatten, W. Tittel, H. Zbinden, and N. Gisin, Nature **421**, 509 (2003).

[15] I. Marcikic, H. de Riedmatten, W. Tittel, H. Zbinden, M. Legré, and N. Gisin, Phys. Rev. Lett. **93**, 180502 (2004).

[16] H. de Riedmatten, I. Marcikic, H. Zbinden, and N. Gisin, Quant. Inf. Comp. **2**, 425 (2002).

[17] H. de Riedmatten, I. Marcikic, V. Scarani, W. Tittel, H. Zbinden, and N. Gisin, Phys. Rev. A **69**, 050304 (2004).

[18] A. Einstein, B. Podolsky, and N. Rosen, Phys. Rev. **47**, 777 (1935).

[19] J. Bell, Physics **1**, 195 (1964).

[20] S. J. Freedman and J. F. Clauser, Phys. Rev. Lett. **28**, 938 (1972).

[21] A. Aspect, P. Grangier, and G. Roger, Phys. Rev. Lett. **47**, 460 (1981).

[22] A. Aspect, P. Grangier, and G. Roger, Phys. Rev. Lett. **49**, 91 (1982).

[23] E. Schrödinger, Proc. Cambridge Philo. Soc. **31**, 555 (1935).

[24] N. Herbert, Found. Phys. **12**, 1171 (1982).

[25] D. Kaiser, *How the Hippies Saved Physics* (W. W. Norton Company, New York, 2011).

[26] C. H. Bennett, G. Brassard, C. Crpeau, R. Jozsa, A. Peres, and W. K. Wootters, Phys. Rev. Lett. **70**, 1895 (1993).

[27] D. Bouwmeester, J.-W. Pan, K. Mattle, M. Eibl, H. Weinfurter, and A. Zeilinger, Nature **390**, 575 (1997).

[28] A. Einstein and N. Rosen, Phys. Rev. **48**, 73 (1935).

[29] J. Maldacena and L. Susskind, Fortschritte der Physik **61**, 781 (2013).

[30] K. Jensen and A. Karch, Phys. Rev. Lett. **111**, 211602 (2013).

[31] J. Sonner, Phys. Rev. Lett. **111**, 211603 (2013).

[32] R. T. Nicolas Gisin, Nat. Photon. **1**, 165 (2007).

[33] X.-S. Ma *et al.*, Nature **489**, 269 (2012).

[34] C. H. Bennett and G. Brassard, *Proceedings of the IEEE International Conference on Computers, Systems, and Signal Processing, Bangalore, India* (IEEE, New York, 1984).

[35] A. K. Ekert, Phys. Rev. Lett. **67**, 661 (1991).

[36] N. Sangouard, C. Simon, H. de Riedmatten, and N. Gisin, Rev. Mod. Phys. **83**, 33 (2011).

[37] M. Aspelmeyer, T. Jennewein, M. Pfennigbauer, W. Leeb, and A. Zeilinger, Selected Topics in Quantum Electronics, IEEE Journal of **9**, 1541 (2003).

[38] G. Vallone, D. Bacco, D. Dequal, S. Gaiarin, V. Luceri, G. Bianco, and P. Villoresi, Phys. Rev. Lett. **115**, 040502 (2015).

[39] H.-J. Briegel, W. Dür, J. I. Cirac, and P. Zoller, Phys. Rev. Lett. **81**, 5932 (1998).

[40] L.-M. Duan, M. D. Lukin, J. I. Cirac, and P. Zoller, Nature **414**, 413 (2001).

[41] C. Simon, H. de Riedmatten, M. Afzelius, N. Sangouard, H. Zbinden, and N. Gisin, Phys. Rev. Lett. **98**, 190503 (2007).

[42] S. Chen, Y.-A. Chen, T. Strassel, Z.-S. Yuan, B. Zhao, J. Schmiedmayer, and J.-W. Pan, Phys. Rev. Lett. **97**, 173004 (2006).

[43] D. N. Matsukevich, T. Chaneliere, S. D. Jenkins, S.-Y. Lan, T. A. B. Kennedy, and A. Kuzmich, Phys. Rev. Lett. **97**, 013601 (2006).

[44] A. Imamoglu, Phys. Rev. Lett. **89**, 163602 (2002).

[45] D. F. V. James and P. G. Kwiat, Phys. Rev. Lett. **89**, 183601 (2002).

[46] P. Kok, W. J. Munro, K. Nemoto, T. C. Ralph, J. P. Dowling, and G. J. Milburn, Rev. Mod. Phys. **79**, 135 (2007).

[47] A. I. Lvovsky, B. C. Sanders, and W. Tittel, Nat. Photon. **3**, 706 (2009).

[48] C. Simon *et al.*, The European Physical Journal D - Atomic, Molecular, Optical and Plasma Physics **58**, 1 (2010-05-01).

[49] F. Bussieres, N. Sangouard, M. Afzelius, H. de Riedmatten, C. Simon, and W. Tittel, Journal of Modern Optics **60**, 1519 (2013).

[50] B. Julsgaard, J. Sherson, J. I. Cirac, J. Fiurášek, and E. S. Polzik, Nature **432**, 482 (2004).

[51] J. Appel, E. Figueroa, D. Korystov, M. Lobino, and A. I. Lvovsky, Phys. Rev. Lett. **100**, 093602 (2008).

[52] K. Jensen, W. Wasilewski, H. Krauter, T. Fernholz, B. M. Nielsen, M. Owari, M. B. Plenio, A. Serafini, M. M. Wolf, and E. S. Polzik, Nat. Phys. **7**, 13 (2011).

[53] S. L. Braunstein and P. van Loock, Rev. Mod. Phys. **77**, 513 (2005).

[54] J. Dias and T. Ralph, arXiv:1505.03626 (2015).

[55] C. W. Chou, H. de Riedmatten, D. Felinto, S. V. Polyakov, S. J. van Enk, and H. J. Kimble, Nature **438**, 828 (2005).

[56] E. Togan *et al.*, Nature **466**, 730 (2010).

[57] W. B. Gao, P. Fallahi, E. Togan, J. Miguel-Sanchez, and A. Imamoglu, Nature **491**, 426– (2012).

[58] K. D. Greve *et al.*, Nature **491**, 421– (2012).

[59] S. Massar and S. Popescu, Phys. Rev. Lett. **74**, 1259 (1995).

[60] X. Fernandez-Gonzalvo, G. Corrielli, B. Albrecht, M. Grimau, M. Cristiani, and H. de Riedmatten, Opt. Express **21**, 19473 (2013).

[61] B. Albrecht, P. Farrera, X. Fernandez-Gonzalvo, M. Cristiani, and H. de Riedmatten, Nat. Commun. **5**, 3376 (2014).

[62] J. Fekete, D. Rieländer, M. Cristiani, and H. de Riedmatten, Phys. Rev. Lett. **110**, 220502 (2013).

[63] *Coherent Transients And Holeburning Spectroscopy In Rare Earth Ions In Solids; Spectroscopy Of Crystals Containing Rare Earth Ions*, edited by A. Kaplyankii and R. Macfarlane (Elsevier Science Publishers, Amsterdam, Netherlands, 1987).

[64] G. Liu, in *Spectroscopic Properties of Rare Earths in Optical Materials (Chapter 1)*, edited by G. Liu and B. Jacquier (Springer-Verlag, Berlin Heidelberg, 2005).

[65] P. Goldner, A. Ferrier, and O. Guillot-Noel, *Handbook on the Physics and Chemistry of Rare Earths (Chapter 267)* (edited by J.-C.G. Bünzli and V.K. Pecharsky (Elsevier B.V.), ADDRESS, 2015).

[66] F. R. Graf, Ph.D. thesis, ETH Zürich, 1998.

[67] L. Petersen, Ph.D. thesis, ETH Zürich, 2011.

[68] C. Huang, *Rare Earth Coordination Chemistry: Fundamentals and Applications* (John Wiley and Sons (Asia) Pte Ltd., Singapore, 2010).

[69] Y. Sun, C. W. Thiel, R. L. Cone, R. W. Equall, and R. L. Hutcheson, J. Lumin. **98**, 281 (2002).

[70] R. W. Equall, Y. Sun, R. L. Cone, and R. M. Macfarlane, Phys. Rev. Lett. **72**, 2179 (1994).

[71] H. Kramers, Proc. Amsterdam Acad, vol. 33, p. 959, 1930 **33**, 959 (1930).

[72] R. M. Shelby, R. M. Macfarlane, and C. S. Yannoni, Phys. Rev. B **21**, 5004 (1980).

[73] M. Nilsson, Ph.D. thesis, Lund Institute of Technology, 2004.

[74] S. B. Altner, G. Zumofen, U. P. Wild, and M. Mitsunaga, Phys. Rev. B **54**, 17493 (1996).

[75] E. Fraval, M. J. Sellars, and J. J. Longdell, Phys. Rev. Lett. **92**, 077601 (2004).

[76] D. L. McAuslan, J. G. Bartholomew, M. J. Sellars, and J. J. Longdell, Phys. Rev. A **85**, 032339 (2012).

[77] R. W. Equall, R. L. Cone, and R. M. Macfarlane, Phys. Rev. B **52**, 3963 (1995).

[78] M. Nilsson, L. Rippe, S. Kröll, R. Klieber, and D. Suter, Phys. Rev. B **70**, 214116 (2004).

[79] K. Holliday, M. Croci, E. Vauthey, and U. P. Wild, Phys. Rev. B **47**, 14741 (1993).

[80] B. S. Ham, M. S. Shahriar, M. K. Kim, and P. R. Hemmer, Phys. Rev. B **58**, R11825 (1998).

[81] M. Afzelius, C. Simon, H. de Riedmatten, and N. Gisin, Phys. Rev. A **79**, 052329 (2009).

[82] M. Fox, *Quantum Optics* (Oxford University Press, ADDRESS, 2011).

[83] L. Mandel and E. Wolf, *Optical Coherence And Quantum Optics* (Cambridge University Press, Cambridge, 1995).

[84] L. Allen and J. Eberly, *Optical resonance and two-level atoms* (Dover, New York, 1975).

[85] L. Rippe, Ph.D. thesis, Lund University, 2006.

[86] N. Sangouard, C. Simon, M. Afzelius, and N. Gisin, Phys. Rev. A **75**, 032327 (2007).

[87] N. Kurnit, I. Abella, and S. Hartmann, Phys. Rev. Lett. **13**, 567 (1964).

[88] I. D. Abella, N. A. Kurnit, and S. R. Hartmann, Phys. Rev. **141**, 391 (1966).

[89] N. Sinclair, Master's thesis, University of Calgary, 2010.

[90] T. W. Mossberg, Opt. Lett. **7**, 77 (1982).

[91] Y. Sun, in *'Rare Earth Materials in Optical Storage and Data Processing Applications' in G Liu and B Jacquir (Eds) 'Spectroscopic Properties of Rare Earths in Optical Materials'*, edited by G. Liu and B. Jacquier (Springer-Verlag, Berlin Heidelberg, 2005).

[92] M. K. Kim and R. Kachru, Phys. Rev. B **40**, 2082 (1989).

[93] M. Mitsunaga and N. Uesugi, Opt. Lett. **15**, 195 (1990).

[94] X. A. Shen and R. Kachru, Proc. SPIE **3531**, 11 (1998).

[95] J. Ruggiero, J.-L. L. Gouet, C. Simon, and T. Chaneliere, Phys. Rev. A **79**, 053851 (2009).

[96] N. Sangouard, C. Simon, J. c. v. Minář, M. Afzelius, T. Chanelière, N. Gisin, J.-L. Le Gouët, H. de Riedmatten, and W. Tittel, Phys. Rev. A **81**, 062333 (2010).

[97] P. M. Ledingham, W. R. Naylor, J. J. Longdell, S. E. Beavan, and M. J. Sellars, Phys. Rev. A **81**, 012301 (2010).

[98] V. Damon, M. Bonarota, A. Louchet-Chauvet, T. Chaneliere, and J.-L. L. Gouet, New Journal of Physics **13**, 093031 (2011).

[99] P. M. Ledingham, W. R. Naylor, and J. J. Longdell, Phys. Rev. Lett. **109**, 093602 (2012).

[100] K.-J. Boller, A. Imamoglu, and S. E. Harris, Phys. Rev. Lett. **66**, 2593 (1991).

[101] L. V. Hau, S. E. Harris, Z. Dutton, and C. H. Behroozi, Nature **397**, 594 (1999).

[102] M. Fleischhauer and M. D. Lukin, Phys. Rev. Lett. **84**, 5094 (2000).

[103] C. Liu, Z. Dutton, C. H. Behroozi, and L. V. Hau, Nature **409**, 490 (2001).

[104] D. F. Phillips, A. Fleischhauer, A. Mair, R. L. Walsworth, and M. D. Lukin, Phys. Rev. Lett. **86**, 783 (2001).

[105] A. V. Turukhin, V. S. Sudarshanam, M. S. Shahriar, J. A. Musser, B. S. Ham, and P. R. Hemmer, Phys. Rev. Lett. **88**, 023602 (2001).

[106] T. Chanelière, D. N. Matsukevich, S. D. Jenkins, S.-Y. Lan, T. A. B. Kennedy, and A. Kuzmich, Nature **438**, 833 (2005).

[107] K. S. Choi, H. Deng, J. Laurat, and H. J. Kimble, Nature **452**, 67 (2008).

[108] M. D. Eisaman, A. André, F. Massou, M. Fleischhauer, A. S. Zibrov, and M. D. Lukin, Nature **438**, 837 (2005).

[109] J. J. Longdell, E. Fraval, M. J. Sellars, and N. B. Manson, Phys. Rev. Lett. **95**, 063601 (2005).

[110] G. Heinze, C. Hubrich, and T. Halfmann, Phys. Rev. Lett. **111**, 033601 (2013).

[111] M. Mucke, E. Figueroa, J. Bochmann, C. Hahn, K. Murr, S. Ritter, C. J. Villas-Boas, and G. Rempe, Nature **465**, 755 (2010).

[112] J. Simon, H. Tanji, J. K. Thompson, and V. Vuletic, Phys. Rev. Lett. **98**, 183601 (2007).

[113] Y.-H. Chen, M.-J. Lee, I.-C. Wang, S. Du, Y.-F. Chen, Y.-C. Chen, and I. A. Yu, Phys. Rev. Lett. **110**, 083601 (2013).

[114] S. Zhou, S. Zhang, C. Liu, J. F. Chen, J. Wen, M. M. T. Loy, G. K. L. Wong, and S. Du, Opt. Express **20**, 24124 (2012).

[115] M. T. L. Hsu, G. Hétet, O. Glöckl, J. J. Longdell, B. C. Buchler, H.-A. Bachor, and P. K. Lam, Phys. Rev. Lett. **97**, 183601 (2006).

[116] M. D. Lukin, Rev. Mod. Phys. **75**, 457 (2003).

[117] S. A. Moiseev and S. Kröll, Phys. Rev. Lett. **87**, 173601 (2001).

[118] M. Nilsson and S. Kröll, Optics Communications **247**, 393 (2005).

[119] A. L. Alexander, J. J. Longdell, M. J. Sellars, and N. B. Manson, Phys. Rev. Lett. **96**, 043602 (2006).

[120] B. Lauritzen, J. Minar, H. de Riedmatten, M. Afzelius, N. Sangouard, C. Simon, and N. Gisin, Phys. Rev. Lett. **104**, 080502 (2010).

[121] M. P. Hedges, J. J. Longdell, Y. Li, and M. J. Sellars, Nature **465**, 1052 (2010).

[122] G. Hétet, J. J. Longdell, A. L. Alexander, P. K. Lam, and M. J. Sellars, Phys. Rev. Lett. **100**, 023601 (2008).

[123] G. Hétet, M. Hosseini, B. M. Sparkes, D. Oblak, P. K. Lam, and B. C. Buchler, Opt. Lett. **33**, 2323 (2008).

[124] M. Hosseini, B. M. Sparkes, G. T. Campbell, P. K. Lam, and B. C. Buchler, Journal of Physics B: Atomic, Molecular and Optical Physics **45**, 124004 (2012).

[125] M. Hosseini, B. Sparkes, G. Campbell, P. Lam, and B. Buchler, Nat. Comm. **2**, 174 (2011).

[126] M. Hosseini, G. Campbell, B. M. Sparkes, P. K. Lam, and B. C. Buchler, Nat. Phys. **7**, 794 (2011).

[127] J. Nunn, K. Reim, K. C. Lee, V. O. Lorenz, B. J. Sussman, I. A. Walmsley, and D. Jaksch, Phys. Rev. Lett. **101**, 260502 (2008).

[128] A. L. Alexander, Ph.D. thesis, the Australian National University, 2007.

[129] H. de Riedmatten, M. Afzelius, M. U. Staudt, C. Simon, and N. Gisin, Nature **456**, 773 (2008).

[130] M. Bonarota, J. Ruggiero, J. L. L. Gouët, and T. Chanelière, Phys. Rev. A **81**, 033803 (2010).

[131] P. Jobez, N. Timoney, C. Laplane, , N. Gisin, and M. Afzelius, New Journal of Physics **16**, 083005 (2014).

[132] N. Sinclair *et al.*, Phys. Rev. Lett. **113**, 053603 (2014).

[133] C. Simon, Y.-M. Niquet, X. Caillet, J. Eymery, J.-P. Poizat, and J.-M. Gerard, Phys. Rev. B **75**, 081302 (2007).

[134] M. Afzelius *et al.*, Phys. Rev. Lett. **104**, 040503 (2010).

[135] J. c. v. Minář, N. Sangouard, M. Afzelius, H. de Riedmatten, and N. Gisin, Phys. Rev. A **82**, 042309 (2010).

[136] I. Usmani, M. Afzelius, H. de Riedmatten, and N. Gisin, Nat Commun **1**, 12 (2010).

[137] M. Bonarota, J.-L. L. Gouët, and T. Chanelière, New Journal of Physics **13**, 013013 (2011).

[138] C. Clausen, I. Usmani, F. Bussieres, N. Sangouard, M. Afzelius, H. de Riedmatten, and N. Gisin, Nature **469**, 508 (2011).

[139] E. Saglamyurek, N. Sinclair, J. Jin, J. A. Slater, D. Oblak, F. Bussieres, M. George, R. Ricken, W. Sohler, and W. Tittel, Nature **469**, 512 (2011).

[140] I. Usmani, C. Clausen, F. Bussieres, N. Sangouard, M. Afzelius, and N. Gisin, Nat. Photon. **6**, 234 (2012).

[141] E. Saglamyurek, N. Sinclair, J. Jin, J. A. Slater, D. Oblak, F. Bussières, M. George, R. Ricken, W. Sohler, and W. Tittel, Phys. Rev. Lett. **108**, 083602 (2012).

[142] E. Saglamyurek, N. Sinclair, J. A. Slater, K. Heshami, D. Oblak, and W. Tittel, New Journal of Physics **16**, 065019 (2014).

[143] J. Jin, J. A. Slater, E. Saglamyurek, N. Sinclair, M. George, R. Ricken, D. Oblak, W. Sohler, and W. Tittel, Nat. Comm. **4**, 2386 (2013).

[144] E. Saglamyurek, J. Jin, V. B. Verma, M. D. Shaw, F. Marsili, S. W. Nam, D. Oblak, and W. Tittel, Nat. Photon. **9**, 83 (2015).

[145] D. Rielander, K. Kutluer, P. M. Ledingham, M. Gundogan, J. Fekete, M. Mazzera, and H. de Riedmatten, Phys. Rev. Lett. **112**, 040504 (2014).

[146] M. Zhong, M. P. Hedges, R. L. Ahlefeldt, J. G. Bartholomew, S. E. Beavan, S. M. Wittig, J. J. Longdell, and M. J. Sellars, .

[147] N. Timoney, B. Lauritzen, I. Usmani, M. Afzelius, and N. Gisin, Journal of Physics B: Atomic, Molecular and Optical Physics **45**, 124001 (2012).

[148] N. Timoney, I. Usmani, P. Jobez, M. Afzelius, and N. Gisin, Phys. Rev. A **88**, 022324 (2013).

[149] M. Afzelius and C. Simon, Phys. Rev. A **82**, 022310 (2010).

[150] M. Sabooni, S. T. Kometa, A. Thuresson, S. Kroll, and L. Rippe, New Journal of Physics **15**, 035025 (2013).

[151] M. Sabooni, Q. Li, S. Kröll, and L. Rippe, Phys. Rev. Lett. **110**, 133604 (2013).

[152] M. Gündoğan, P. M. Ledingham, A. Almasi, M. Cristiani, and H. de Riedmatten, Phys. Rev. Lett. **108**, 190504 (2012).

[153] C. Clausen, F. Bussières, M. Afzelius, and N. Gisin, Phys. Rev. Lett. **108**, 190503 (2012).

[154] Z.-Q. Zhou, W.-B. Lin, M. Yang, C.-F. Li, and G.-C. Guo, Phys. Rev. Lett. **108**, 190505 (2012).

[155] M. Gündoğan, M. Mazzera, P. M. Ledingham, M. Cristiani, and H. de Riedmatten, New Journal of Physics **15**, 045012 (2013).

[156] M. Gündoğan, P. M. Ledingham, K. Kutluer, M. Mazzera, and H. de Riedmatten, Phys. Rev. Lett. **000**, 0000 (2015).

[157] R. W. Boyd, *Nonliear Optics* (Academic Press, San Diego, CA, 1992).

[158] E. D. Black, American Journal of Physics **69**, 79 (2001).

[159] E. A. Donley, T. P. Heavner, F. Levi, M. O. Tataw, and S. R. Jefferts, Review of Scientific Instruments **76**, (2005).

[160] H. P. Specht, C. Nolleke, A. Reiserer, M. Uphoff, E. Figueroa, S. Ritter, and G. Rempe, Nature **473**, 190 (2011).

[161] H. Tanji, S. Ghosh, J. Simon, B. Bloom, and V. Vuletić, Phys. Rev. Lett. **103**, 043601 (2009).

[162] Y.-W. Cho and Y.-H. Kim, Optics Express **18**, 25786 (2010).

[163] D. G. England *et al.*, Journal of Physics B: Atomic, Molecular and Optical Physics **45**, 124008 (2012).

[164] C. Kupchak, T. Mittiga, B. Jordaan, M. Namazi, C. Nolleke, and E. Figueroa, Scientific Reports **5**, (2015).

[165] N. Peters, J. Alteper, E. Jeffrey, D. Branning, and P. Kwiat, Quantum Information Computation **3**, 503 (2003).

[166] D. F. V. James, P. G. Kwiat, W. J. Munro, and A. G. White, Phys. Rev. A **64**, 052312 (2001).

[167] C. W. Chou, J. Laurat, H. Deng, K. S. Choi, H. de Riedmatten, D. Felinto, and H. J. Kimble, Science **316**, 1316 (2007).

[168] A. Tiranov *et al.*, Optica **2**, 279 (2015).

[169] O. Guillot-Noel, P. Goldner, Y. L. Du, P. Loiseau, B. Julsgaard, L. Rippe, and S. Kroll, Phys. Rev. B **75**, 205110 (2007).

[170] B. S. Ham and P. R. Hemmer, Phys. Rev. B **68**, 073102 (2003).

[171] M. O. Scully and M. S. Zubairy, *Quantum Optics* (Cambridge University Press, Cambridge, 1997).

[172] B. Lauritzen, N. Timoney, N. Gisin, M. Afzelius, H. de Riedmatten, Y. Sun, R. M. Macfarlane, and R. L. Cone, Phys. Rev. B **85**, 115111 (2012).

[173] Y. Sun, G. M. Wang, R. L. Cone, R. W. Equall, and M. J. M. Leask, Phys. Rev. B **62**, 15443 (2000).

[174] M. U. Staudt, S. R. Hastings-Simon, M. Nilsson, M. Afzelius, V. Scarani, R. Ricken, H. Suche, W. Sohler, W. Tittel, and N. Gisin, Phys. Rev. Lett. **98**, 113601 (2007).

[175] M. U. Staudt, M. Afzelius, H. de Riedmatten, S. R. Hastings-Simon, C. Simon, R. Ricken, H. Suche, W. Sohler, and N. Gisin, Phys. Rev. Lett. **99**, 173602 (2007).

[176] S. A. Moiseev, S. N. Andrianov, and F. F. Gubaidullin, Phys. Rev. A **82**, 022311 (2010).

[177] E. Fraval, M. J. Sellars, and J. J. Longdell, Phys. Rev. Lett. **95**, 030506 (2005).

[178] M. Lovrić, D. Suter, A. Ferrier, and P. Goldner, Phys. Rev. Lett. **111**, 020503 (2013).

[179] M. F. Pascual-Winter, R.-C. Tongning, T. Chanelière, and J.-L. Le Gouët, Phys. Rev. B **86**, 184301 (2012).

[180] G. Heinze, S. Mieth, and T. Halfmann, Phys. Rev. A **84**, 013827 (2011).

[181] P. Jobez, C. Laplane, N. Timoney, N. Gisin, A. Ferrier, P. Goldner, and M. Afzelius, Phys. Rev. Lett. **114**, 230502 (2015).

[182] H. Zhang, M. Sabooni, L. Rippe, C. Kim, S. Kröll, L. V. Wang, and P. R. Hemmer, Applied Physics Letters **100**, 131102 (2012).

[183] S. E. Beavan, E. A. Goldschmidt, and M. J. Sellars, J. Opt. Soc. Am. B **30**, 1173 (2013).

[184] N. Maring, K. Kutluer, J. Cohen, M. Cristiani, M. Mazzera, and H. de Riedmatten, New Journal of Physics **16**, 113021 (2014).

[185] H. de Riedmatten and M. Afzelius, arXiv:1502.00307 .

[186] S. Mieth, D. Schraft, T. Halfmann, and L. P. Yatsenko, Phys. Rev. A **86**, 063404 (2012).

[187] G. Demeter, Phys. Rev. A **88**, 052316 (2013).

[188] J. Dajczgewand, J.-L. L. Gouët, A. Louchet-Chauvet, and T. Chaneliere, Opt. Lett. **39**, 2711 (2014).

[189] J. Dajczgewand, R. Ahlefeldt, T. Bottger, A. Louchet-Chauvet, J.-L. L. Gouet, and T. .Chaneliere, New Journal of Physics **17**, 023031 (2015).

[190] K. Hennessy, A. Badolato, M. Winger, D. Gerace, M. Atature, S. Gulde, S. Falt, E. L. Hu, , and A. Imamoglu, Nature **445**, 896 (2007).

[191] A. Faraon, Ph.D. thesis, Stanford University, 2009.

[192] A. Faraon, P. E. Barclay, C. Santori, K.-M. C. Fu, and R. G. Beausoleil, Nat. Photon. **5**, 301 (2011).

[193] R. Albrecht, A. Bommer, C. Deutsch, J. Reichel, and C. Becher, Phys. Rev. Lett. **110**, 243602 (2013).

[194] J. Riedrich-Möller, S. Pezzagna, J. Meijer, C. Pauly, F. Mücklich, M. Markham, A. M. Edmonds, and C. Becher, arXiv:1503.05666 (2015).

[195] R. G. Neuhauser, K. T. Shimizu, W. K. Woo, S. A. Empedocles, and M. G. Bawendi, Phys. Rev. Lett. **85**, 3301 (2000).

[196] C. Bradac, T. Gaebel, N. Naidoo, M. J. Sellars, J. Twamley, L. J. Brown, B. A. S., T. Plakhotnik, A. V. Zvyagin, and J. R. Rabeau, Nat. Nanotech. **5**, 345 (2010).

[197] T. Zhong, J. Kindem, E. Miyazono, and A. Faraon, arXiv:1507.00977 (2015).

[198] S. Marzban, J. G. Bartholomew, S. Madden, K. Vu, and M. J. Sellars, Phys. Rev. Lett. **115**, 013601 (2015).

[199] G. D. Valle, R. Osellame, and P. Laporta, J. Opt. A Pure Appl. Opt. **11**, 013001 (2009).

" As it often happens in science, these things were well known to those who know things well."

Asher Peres[1]

[1] Asher Peres. How the no-cloning theorem got its name, *Fortschritte der Physik*, vol. 4-5, 458, 2003.